INLET MANIFOLD TESTS AND PERFORMANCE EVALUATION OF DEPHLEGMATORS IN AIR-COOLED STEAM CONDENSERS

Leslie van Zyl Smit

Thesis presented in partial fulfilment of the requirements for the degree of Master of Science in Mechanical Engineering at the University of Stellenbosch.

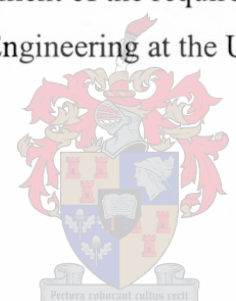

Thesis supervisor: Prof. D.G. Kröger

Department of Mechanical Engineering
University of Stellenbosch
Stellenbosch, South Africa

November 2000

DECLARATION

I, Leslie van Zyl Smit, the undersigned, hereby declare that the work contained in this thesis is my own original work and has not previously, in its entirety or in part, been submitted at any university for a degree.

Signature of candidate

ABSTRACT

Measurements on air-cooled reflux steam condensers or dephlegmators at different power plants have shown that sections of these units do not transfer heat effectively over a range of operating conditions. The ineffective sections may be due to flooding in the finned tubes although entrainment of condensate in certain steam inlet manifolds is usually the main reason for the poor performance.

In this dissertation factors that limit effective dephlegmator operation are discussed and the influence of two inlet manifold designs on dephlegmator operation is investigated. Laboratory experiments are conducted to show under which conditions liquid entrainment occurs and to visualize the flow distribution within the respective manifolds.

An alternative, essentially horizontal arrangement of the dephlegmator is proposed. In order to evaluate the performance of such a system, the heat transfer and pressure drop on the steam-side is determined experimentally in an air-cooled finned tube. No flooding was observed during tests conducted at zero and negative tube angles to the horizontal.

OPSOMMING

Toetse op lugverkoelde stoom terugvloeikondensors, of deflegmators, by verskeie kragstasies het getoon dat sekere dele van hierdie eenhede onder verskeie werkstoestande nie warmte effektief oordra nie. Hierdie oneffektiewe dele kan deur vloeding van die vinbuise veroorsaak word alhoewel die meesleur van kondensaat in sekere stoom inlaatspruitstukke gewoonlik die hoof oorsaak is.

In hierdie dissertasie word faktore wat effektiewe deflegmator werksverrigting beïnvloed bespreek en die invloed van twee inlaatspruitstukontwerpe op deflegmator werksverrigting ondersoek. Eksperimente is in 'n laboratorium uitgevoer om aan te toon onder watter werkstoestande vloeistof samesleping voorkom en om vloeiverdeling binne die onderskeie inlaatspruitstukke te visualiseer.

'n Alternatiewe, wesenlike horisontale deflegmator opstelling word voorgestel. Die werksverrigting van hierdie voorstelling is ondersoek deur die warmteoordrag en stoom-kant drukval eksperimenteel te bepaal in 'n lugverkoelde vinbuis. Geen vloeding is opgemerk vir toetsgevalle waar klein negatiewe of zero hoeke tot die horisontaal ondersoek is nie.

ACKNOWLEDGEMENTS

Firstly, I would like to express my gratitude to my promoter, Prof. D.G. Kröger for his guidance and assistance throughout this study.

A special word of thanks, to Kobus Zietsman for his words of encouragement and technical advice.

I further would like to thank my family and friends for their much appreciated support.

This dissertation is dedicated to Jacolene for her love, patience and continual support.

Say not, "I have found the truth," but rather, "I have found a truth."

The Prophet: Kahlil Gibran

TABLE OF CONTENTS

NOMENCLATURE

Symbols

A	-	Area, m^2
a	-	Coefficient, dimensionless
b	-	Coefficient, dimensionless
C	-	Discharge coefficient, dimensionless
c_p	-	Specific heat at constant pressure, J/kg K
c_v	-	Specific heat at constant volume, J/kg K
d	-	Diameter, m
e	-	Heat exchanger effectiveness, dimensionless
F	-	Force, kg m/s^2, or correction factor, dimensionless
f	-	Friction factor, dimensionless
g	-	Gravitational acceleration, m/s^2
H	-	Tube height, or elevation, m
h	-	Heat transfer coefficient, W/m^2K
i	-	Enthalpy, J/kg
i_{fg}	-	Latent heat, J/kg
K	-	Coefficient, dimensionless
k	-	Conductivity, W/mK
L	-	Length, m
M	-	Mass, kg
m	-	Mass flow rate, kg/s
Ny	-	Characteristic heat transfer parameter, m^{-1}
n	-	Number of, or exponent, dimensionless
P	-	Perimeter, or pitch, m
p	-	Pressure, N/m^2
Q	-	Heat transfer rate, W
R	-	Universal gas constant, J/kg K, Radius, m
Ry	-	Characteristic flow parameter, m^{-1}
T	-	Temperature, ^oC
t	-	Time, s
U	-	Overall heat transfer coefficient, W/m^2 K

V	-	Volume flow rate, m^3/s
v	-	Velocity, m/s
W	-	Width, m
x	-	Distance, m
Y	-	Approach velocity factor, dimensionless
z	-	Distance, m

Greek Symbols

Δ	-	Differential
ϕ	-	Expansion factor
η	-	Efficiency, dimensionless
μ	-	Viscosity, kg/ms
θ	-	Angle, ^{o}
ρ	-	Density, kg/m^3
σ	-	Surface tension, N/m, or area ratio, dimensionless

Subscripts

a	-	Air, or based on air side area
abs	-	Absolute
atm	-	Atmospheric
av	-	Average, or Mixture of dry air and water vapour
c	-	Condensate, or casing, or contraction, or cold
cf	-	Counter-flow
D	-	Drag
d	-	Diameter, or downstream, or duct
do	-	Downstream
e	-	Equivalent, or expansion, or effective, or experimental
F	-	Fan
f	-	Fin, or frictional
fr	-	Frontal
g	-	Gas phase, or gravitational
H	-	Height
h	-	Half, or hot
hc	-	Header cross-sectional

he	-	Heat exchanger
i	-	Inlet
iso	-	Isothermal
j	-	Jetting
l	-	Liquid phase
lm	-	Logarithmic mean
m	-	Mean, or momentum, or manifold
n	-	Nozzle
o	-	Outlet
p	-	Pitch, or projected
s	-	Superficial, or steam, or support
sp	-	Single phase
T	-	Temperature
t	-	Tube, or turbine, or total
tb	-	Tube bundle
tc	-	Tube cross-section
tp	-	Two-phase
tr	-	Tube row
ts	-	Tower support
tus	-	Windtunnel cross-section
u	-	Upstream
up	-	Upstream
v	-	Vapour
w	-	Water, or walkway, or wetted
wb	-	Wetbulb

Dimensionless groups

Eu	-	Euler number	$\frac{\Delta p}{\rho v^2}$
Fr_{dsl}	-	Densimetric liquid Froude number based on the hydraulic diameter	$\frac{\rho_l v_{sl}^2}{g d_e (\rho_l - \rho_g)}$
Fr_{Hsg}	-	Densimetric gas Froude number based	$\frac{\rho_g v_{sg}^2}{g H_t (\rho_l - \rho_g)}$

		on the tube eight	
f_D	-	Darcy friction factor	$\frac{d_e \Delta p}{\frac{1}{2}\rho v^2 L}$
Nu	-	Nusselt number	$\frac{h d_e}{k}$
Pr	-	Prandtl number	$\frac{\mu c_p}{k}$
Re	-	Reynolds number	$\frac{\rho v d_e}{\mu}$
Zk_d	-	Zk number	$\frac{(\rho_l d_e \sigma)^{0.5}}{\mu_l}$

Abbreviations

ACC	-	Air-cooled condenser
ACHE	-	Air-cooled heat exchanger
i.d.	-	Inside diameter
i.e.	-	That is
No.	-	Number

CHAPTER 1

INTRODUCTION

1.1 Air-cooled heat exchanger systems

In view of existing water shortages in many countries, and due to an increased global consciousness of environmental problems, power stations and other industries frequently install water-independent cooling systems. Waste heat rejection systems have to operate under thermodynamically and economically more stringent tolerances and more ingenuity in designing these systems is called for.

Air-cooled heat exchangers (hereafter ACHE's) are commonly used and range in size from less than a square metre in surface area to hundreds of thousands of square metres. The most common applications of ACHE's are in household refrigerators, air conditioners, and automobile radiators, but they are also extensively used in power plants and process industries. The general characteristic of ACHE's is the use of finned tubes to transfer heat from the process fluid flowing inside the tubes, to the cooling air forced across them. Fins on the outside of the heat exchanger tubes increase the exposed airside area, and thereby compensate for the poor heat transfer coefficient of the cooling air. In addition, the low specific heat and density of air requires a large volume of airflow, hence the frontal area of the tube bundles is large and the bundle depth is small.

1.2 The use of air-cooled condenser systems in steam power plants

In arid areas where insufficient or no cooling water is available, ACHE systems are the only effective method of power plant heat rejection. Figure 1.1 shows a photo of the largest air-cooled steam condenser in the world as used by the Matimba power station situated at Ellisras in South Africa.

Figure 1.1: Photo of an air-cooled steam condenser system.

The tube bundles of air-cooled condensers (hereafter ACC's) used in steam power plants, are arranged in two basic configurations, namely an A- or V- configuration as shown in figures 1.2 and 1.3 respectively. Turbine exhaust steam is fed to the condenser bundles by means of steam supply ducts situated at the top of the ACC units. The steam flows from the steam ducts into the finned tube bundles, where it is condensed as a result of the heat transfer between the steam and cooling airflow across the tube bundles. By means of gravity, the condensate drains to the bottom of the tube bundles from where it is fed back to the water reservoirs of the power plant. These arrangements (A- and V-configurations) reduce the required ground area and ensure adequate condensate drainage. The required cooling airflow is created by either natural convection or forced flow.

Airflow through natural convection is obtained by placing the condenser tube bundles inside a cooling tower. The density difference between the ambient air, and the heated air above the bundles inside the cooling tower, causes a natural draught that supplies the

required airflow across the bundles. Modern cooling towers have a hyperbolic shaped concrete shell, which may be up to 180 m in height [89GO1].

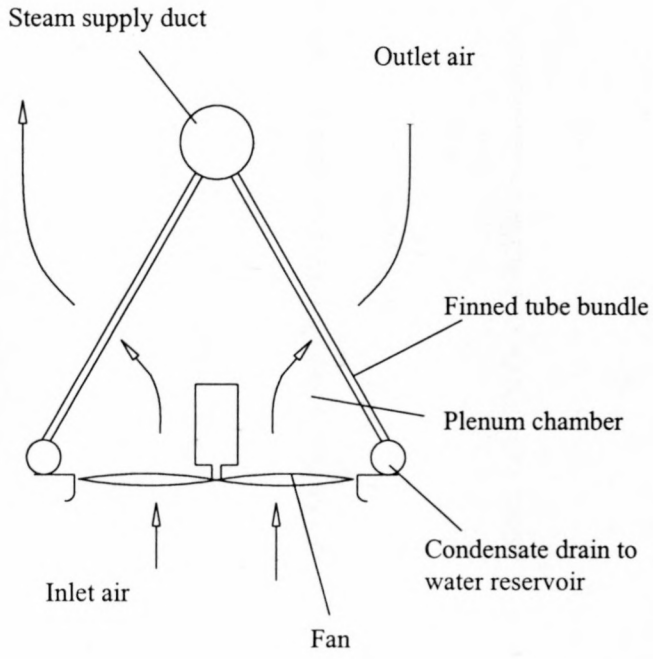

Figure 1.2: Schematics of a forced draught ACC.

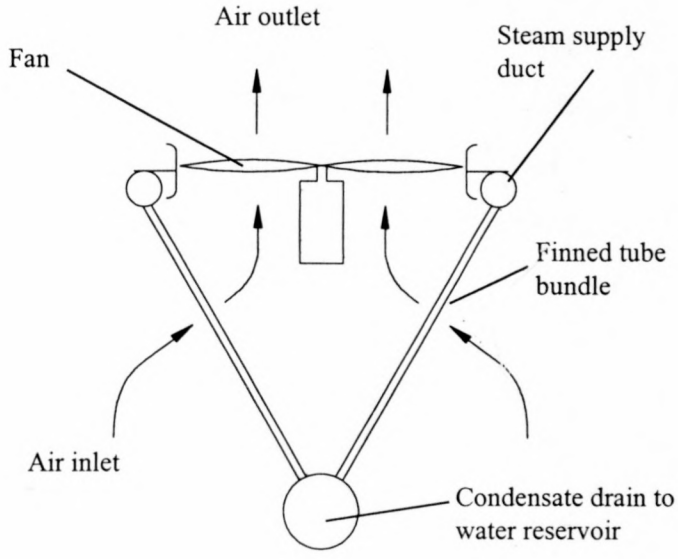

Figure 1.3: Schematics of an induced draught ACC.

Forced airflow, on the other hand, is created by means of mechanical draught systems where air is forced to flow across the airside of the condenser bundles by means of a propeller fan. Mechanical draught systems using the A-configuration are called forced draught heat exchangers, since the air first flows through the fan and is then forced through the finned tube bundles. Systems using the V-configuration are called induced draught heat exchangers, and in these systems the air first flows through the bundles and then through the fan.

Most ACC systems of steam power plants are of the forced draught type, as these systems have the following advantages over induced draught systems: The fans of forced draught systems are installed in the cooler inlet air stream below the heat exchanger tube bundles, which results in lower power consumption for a given air mass flow rate as opposed to induced draught systems. The fans are not exposed to high operating temperatures and the fan drives located in the cooler airflow below the units, are also easier to maintain. Furthermore, high turbulence levels in the plenum chamber produced by the fans, enhance the heat transfer of the tube bundles.

Induced draught systems, on the other hand, also have advantages. These systems are less susceptible to crosswinds and plume recirculation due to the relatively high escape velocity of the air from the fans. Furthermore, induced draught systems have a more uniform velocity distribution across the face of the tube bundles, compared to the appreciable velocity maldistribution encountered in the case of forced draught systems.

1.3 The dephlegmator as integral part of air-cooled condenser systems

Figure 1.4 shows the schematics of a simple air-cooled closed cycle steam power plant. The ideal cycle for such a power plant is the Rankine cycle, which is illustrated by means of the temperature-entropy curve shown in figure 1.5.

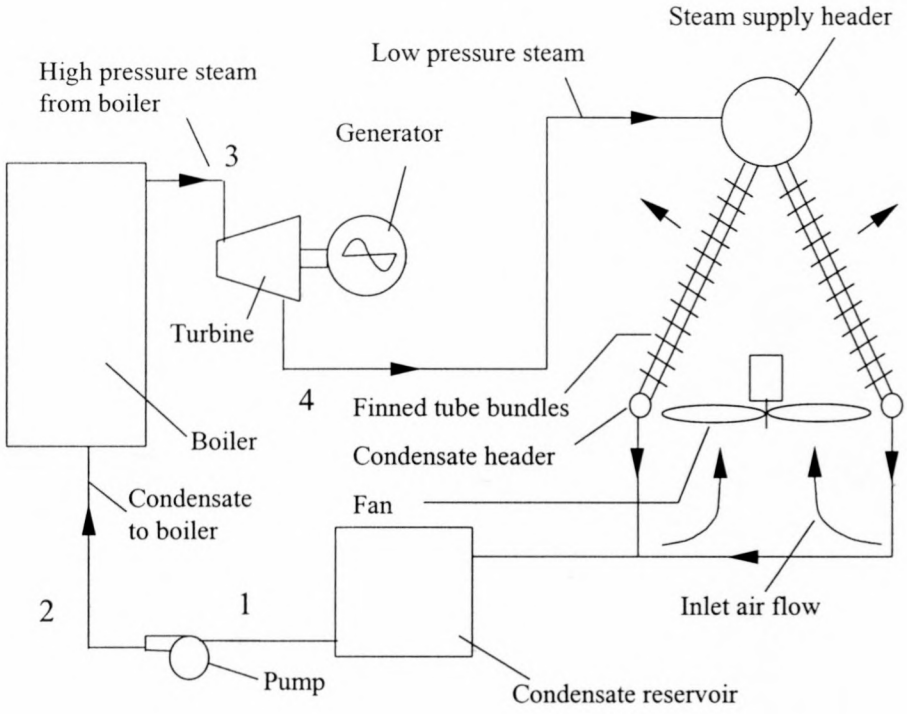

Figure 1.4: Schematics of a closed cycle air-cooled steam power plant.

The Rankine cycle processes of a simple steam power plant shown in figure 1.5 are as follows:

1-2: Reversible adiabatic pumping process.

2-3: Constant pressure transfer of heat in the boiler.

3-4: Reversible adiabatic expansion in the turbine.

4-1: Constant pressure transfer of heat in the condenser.

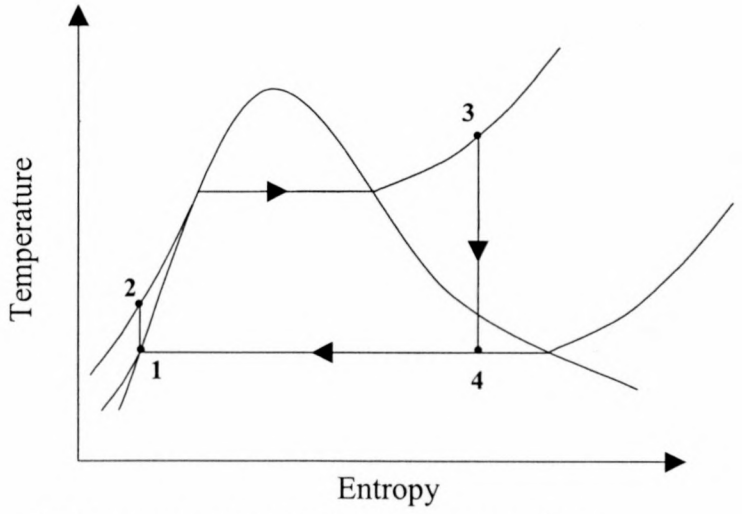

Figure 1.5: The Rankine cycle of a simple steam power plant.

Classical thermodynamics holds that the lower the temperature of the heat sink (condenser), the higher the efficiency of the Rankine cycle. Attaining the lowest possible condensing temperature in the heat sink of the Rankine cycle is therefore a primary goal in surface condenser design [85VA1]. Since the saturation temperature and pressure of steam are directly related, the objective of a low condensing temperature translates to that of a low condenser operating pressure. Accordingly, ACC's used to condense low-pressure turbine exhaust steam, operate at a high level of vacuum.

Due to the encountered vacuum conditions within ACC units, non-condensable gases in the form of atmospheric air tend to leak into these systems. Furthermore, non-condensables in the form of inert gases may also be present in the turbine exhaust steam as a result of boiler feed water treatment. These so-called non-condensable gases tend to collect in the lowest pressure region in the cycle, which is the steam space in the condenser tube bundles. Unless removed continuously and efficiently, these non-condensable gases will adversely interfere with the heat transfer and condensation process in the condenser tube bundles.

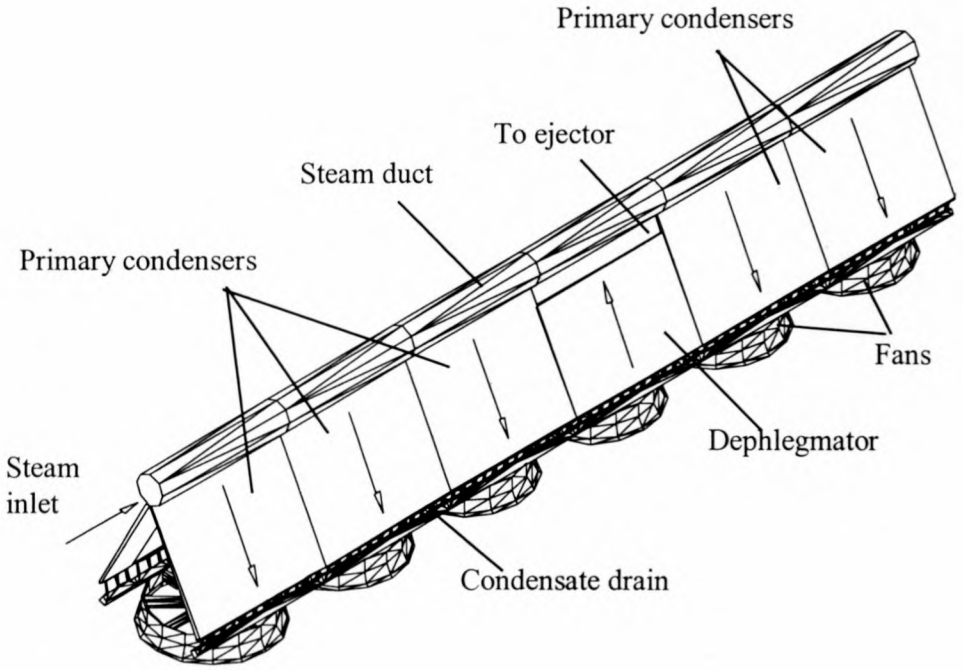

Figure 1.6: Schematics of a typical ACC illustrating the primary condensers and the dephlegmator.

To remove the non-condensables from the ACC system, a secondary condenser, acting as a de-aerator, is connected in series to the primary condenser. This secondary condenser is referred to as a *dephlegmator*, *de-aerator* or *reflux condenser*. Figure 1.6 shows the schematics of a typical A-configuration ACC system that consists of five primary condenser units and a dephlegmator unit.

The objective of the dephlegmator unit is to facilitate a net outflow of steam at the bottom of the primary condenser. Non-condensable gases that are present within the bundle tubes exit along with the steam, and the accumulation of these gases inside the primary condenser units is thus prevented. The steam along with the non-condensables is fed to the dephlegmator bundle tubes, where the steam is condensed and the non-condensables accumulated at a predetermined location inside the dephlegmator. The accumulated non-condensable gases are then removed by means of a suction pump such as a steam driven ejector. The ejector, also referred to as the holding ejector, is not only responsible for the constant removal of non-condensable gases, but also ensures that the vacuum conditions in the low-pressure part of the cycle are maintained.

It is clear that the dephlegmator forms an integral part of ACC systems, and effective operation is essential to ensure efficient and economical power generation in air-cooled, steam power plants. Many dephlegmator systems, however, operate ineffectively as a result of factors discussed in the next chapter.

1.4 The aim of this dissertation

The performance evaluation of forced draught direct ACC systems forms part of an ongoing research and development programme at the University of Stellenbosch [85BE1, 86KO1, 91VE1, 91CO1, 94KR1, 95CO1, 95DU1, 97AZ1]. This dissertation investigates the influence of the D- and box-type inlet manifold designs on dephlegmator operation. A new, essentially horizontal dephlegmator design, which will ensure more effective and economical dephlegmator operation is proposed and tested. The heat transfer and tube pressure differentials of the proposed dephlegmator design

are determined experimentally and it is shown that flooding will not occur in this particular design.

CHAPTER 2

REVIEW OF FACTORS THAT LIMIT EFFECTIVE DEPHLEGMATOR OPERATION

2.1 Introduction

Normal ACHE design procedures assume ideal or 100% performance, during which separated, stratified steam-condensate flow conditions are encountered within the bundle tubes. It is furthermore assumed that there are no non-condensables present, and that the entire surface area (steam- and airside) is available for heat transfer. The steam side heat transfer coefficient of the bundle tubes is calculated accordingly and any performance reduction below the ideal can be defined as ineffective performance. Many existing dephlegmator designs, however, have certain limitations that cause ineffective dephlegmator operation as a result of the accumulation of condensate and/or non-condensables in its bundle tubes.

Accumulated condensate within dephlegmator bundle tubes results in an increase in the pressure drop across the dephlegmator. This increased pressure drop causes a lower suction pressure at the ejectors and the rate at which steam and non-condensables are removed from the system is therefore reduced. Due to inefficient removal, non-condensables accumulate at the top of the bundle tubes to form so-called dead-zones. These dead-zones render part of the dephlegmator bundle tubes unavailable for heat transfer and reduce the overall steam side heat transfer coefficient, leading to ineffective dephlegmator operation.

Figure 2.1 [97ZA1] shows an infrared photograph of the outside tube row of a dephlegmator operating at its design air flow rate. The photograph clearly shows a presence of dead zones at the top of the dephlegmator tube bundles. Zapke [97ZA1] investigated an ACC system and found that the encountered dead zones in its

dephlegmator may amount to a reduction of up to 7 % in its total heat rejection capability. This notable reduction proves that proper dephlegmator design is of utmost importance to ensure effective operation of a steam power plant's ACC system.

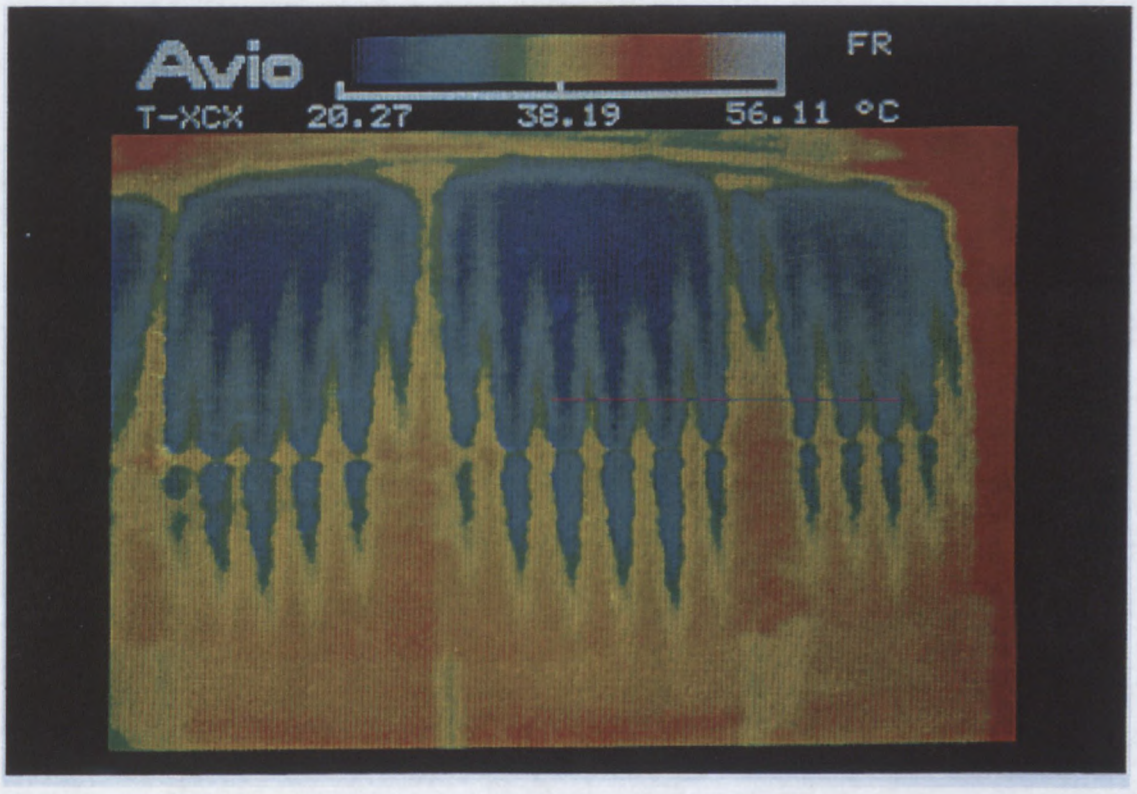

Figure 2.1: Infrared image of dephlegmator tube bundles, illustrating the presence of so- called dead- or cold zones.

Apart from the formation of dead-zones, the ineffective removal of non-condensable gases from dephlegmator bundle tubes also significantly reduces the condensation rate within the tubes. Many researchers [68KR1, 71DE1, 73AL1, 74RA1, 85RO1] have published results on the condensation of vapour in the presence of non-condensable gases. Jensen [88JE1] found that mass transfer resistance to the condensing component results from a built-up layer of non-condensables at the liquid vapour interface. A dramatic reduction in the condensation- and subsequent heat transfer rate was noted. It was found that, depending on conditions, the reduction in heat transfer can range from about 10 % at a non-condensable mass concentration of 0.1% to over 90% at a mass concentration in the range of 5 – 10%.

The presence of oxygen in the non-condensables is another source of concern, since oxygen is known to actuate corrosion of condenser internals. Singh [88SI1] states that a small concentration of oxygen can cause austenitic stainless steel tubing to become highly susceptible to stress corrosion.

Ineffective dephlegmator operation influences the efficiency of the Rankine power generation cycle. According to the Rankine cycle, the efficiency of the power station is a function of the saturation temperature at which the steam is condensed in its condenser units (heat sink).

The governing factors that determine the saturation temperature of ACC units, are the heat rejection capability of the entire system (condenser- and dephlegmator units) and the performance of the ejectors. For a given steam flow rate into the ACC, the saturation temperature will therefore rise and stabilise at higher values if the heat rejection capability is reduced, when, for example, the accumulation of condensate or non-condensables reduces heat transfer coefficients. In other words, the ACC requires a higher mean temperature difference between steam and the ambient air if the heat rejection capability is reduced while the load remains constant.

Due to the saturated steam conditions within the bundle tubes, an increase in the mean temperature difference between the steam and ambient air will result in a corresponding increase in the turbine exhaust pressure, also referred to as back pressure. As the turbine output is a function of the pressure difference across it, an increase in back pressure can be related to a reduction in output.

Factors that contribute to the accumulation of non-condensable gases are poor inlet manifold designs, inadequate ejector operation and tube row effects. These factors are discussed in the following sections.

2.2 *Tube row effects*

A common occurrence in single pass, double row dephlegmator systems is that the heat transfer characteristics of the different tube rows vary as a result of a decrease in the temperature difference between the condensing steam and the cooling air of the consecutive rows. Because the quantity of vapour that each tube row condenses is proportional to the temperature difference between the cooling air and the saturated vapour inside the tube, it follows that row 1 will condense more than row 2 if both tube rows have the same tube effectiveness. Due to the higher condensation rate in tube row 1 the pressure at the top (outlet) of row 1 will be less than that of row 2. This cannot be the case if the tube rows share a common outlet manifold and vapour is therefore forced to enter tube row 1 from row 2, as indicated in figure 2.2. This phenomenon is called steam backflow and the length of the backflow region is denoted by L_b.

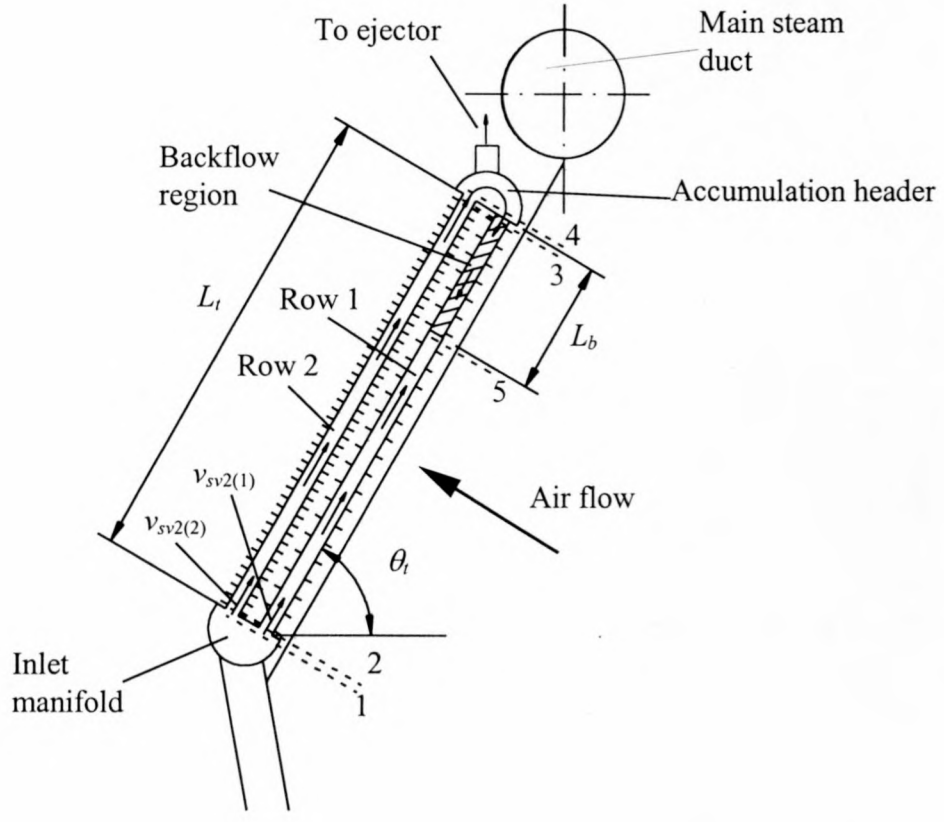

Figure 2.2: Backflow due to row effects in a single-pass double-row dephlegmator unit.

Non-condensable gases that may be present in the vapour will accumulate at the lowest pressure area inside the bundle tubes, which is the backflow region as stated by Berg [80BE1]. Numerous researchers [74RO1, 80BE1, 97FA2, 97ZA1] have published results on tube row effects in single-pass multi-row condensers. Appendix A gives a detailed analysis of the performance characteristics of a typical A-configuration double row dephlegmator system whereby the size of the backflow region can be predicted.

Various designs have been developed in order to solve the problems associated with tube row effects in double row dephlegmator systems [80BE1]. Equal heat transfer rates in both dephlegmator tube rows can be achieved by reducing the fin pitch, and thus increasing the airside surface area of the second tube row. This is known as the matching of the respective tube row heat transfer capabilities. Appendix C illustrates the matching of the tube rows of a particular ACC system by means of a simulation programme.

2.3 Ejector operation

The ejector system is not only responsible for the constant removal of non-condensables, but also ensures that the vacuum conditions in the ACC system are maintained. Adequate suction by the ejector system limits the accumulation of non-condensable gases within the dephlegmator bundle tubes. A sound understanding of the factors that cause the accumulation of non-condensable gases and the formation of dead-zones inside dephlegmator tube bundles enable designers to select ejector systems with adequate suction capabilities.

2.4 Flooding of bundle tubes

The accumulation of condensate within dephlegmator bundle tubes may also result in flooding of the bundle tubes. Hewitt and Taylor [70HE1] state that flooding, in vertical tubes with counter flow conditions, commences when the gas flow rate inside a tube is

increased to the point where liquid starts to flow upward past the point of liquid injection. Figure 2.3 illustrates the onset of flooding in a vertical tube.

This flooding definition also applies to dephlegmator bundle tubes operating at an angle to the horizontal. At the onset of flooding in dephlegmator tubes, the inlet vapour velocity is sufficient to cause the draining condensate to flow upward, resulting in the accumulation of condensate within the bundle tubes. This phenomenon is accompanied by a sudden increase in the tube pressure drop as found by Schoenfeld [97SC1] and Zapke [97ZA1].

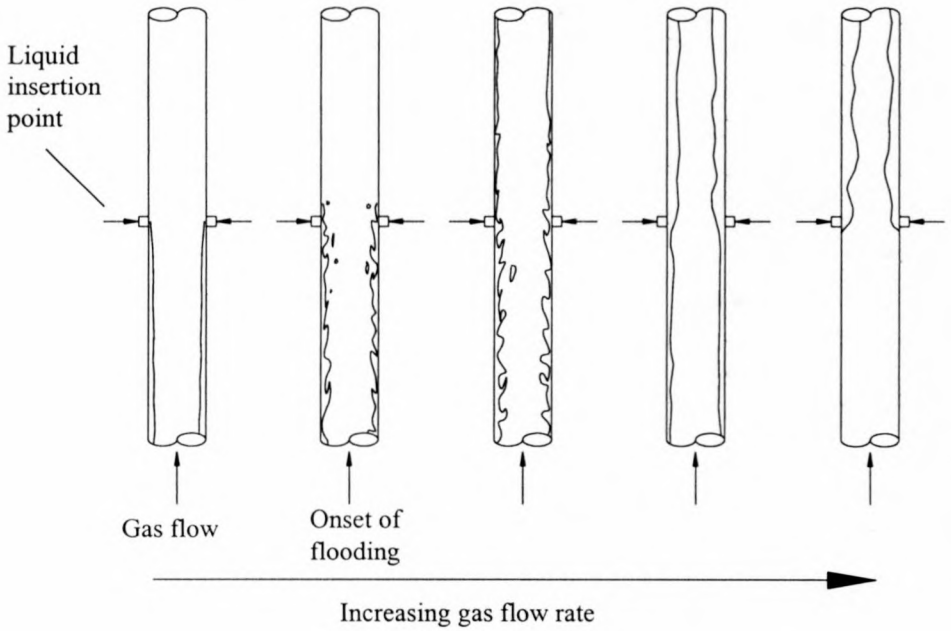

Figure 2.3: Flooding in tubes with counter-current flow conditions.

Schoenfeld [97SC1, 98SC1] conducted tests on a tube used in the design of an ACC system at a particular steam power plant. An inclination angle of 60° to the horizontal was investigated. The results proved that flooding occurs in the specific tube design at a densimetric gas Froude number, Fr_{Hsg}, of the order 0.4. The densimetric gas Froude number is evaluated at the inlet to the bundle tubes as given by equation (2.1).

$$Fr_{Hsg} = \frac{\rho_v v_{sv}^2}{g H_t (\rho_l - \rho_v)} \tag{2.1}$$

All fluid properties as well as the superficial vapour velocity, v_{sv}, are evaluated at the inlet to the finned tube.

Zapke and Kröger [97ZA1] devised an analysis (as given in Appendix A) which can accurately predict the flooding in inclined rectangular ducts, such as dephlegmator bundle tubes. The predicted densimetric gas Froude number at which flooding will occur is given by the following correlation:

$$Fr_{Hsg} = K_o \exp\left(-nFr_{dsl}^{0.6} / Zk_d^{0.2}\right) \tag{2.2}$$

2.5 Inlet manifold design

Dephlegmator inlet manifold designs often pose limitations on the effective operation of these units, as poor designs may contribute to liquid entrainment[1] and the formation of dead-zones in the dephlegmator finned tube bundles. The D- and box-type inlet manifold designs are investigated and discussed as part of this dissertation in order to illustrate the influence of these designs on the operation of typical ACC dephlegmator units.

2.5.1 D-type inlet manifold

Figure 2.4 shows the schematics of an ACC system which incorporates the D-type inlet manifold. Excess steam, as well as non-condensable gases from the primary condenser, is fed to the dephlegmator via the header pipe. At the dephlegmator, the excess steam and non-condensables flow through the draining stubs into the D-manifold and eventually into the finned tube bundles where the steam is condensed. By means of gravity, condensate drains back to the D-manifold and the non-condensable gases are accumulated at the top header of the tube bundles to be removed by the ejector system.

[1]Entrainment is defined as liquid in the form of discrete masses carried in the main gas stream that originated from the liquid at some "earlier stage".

From within the D-manifold, the condensate flows back to the header pipe by means of the drain stubs.

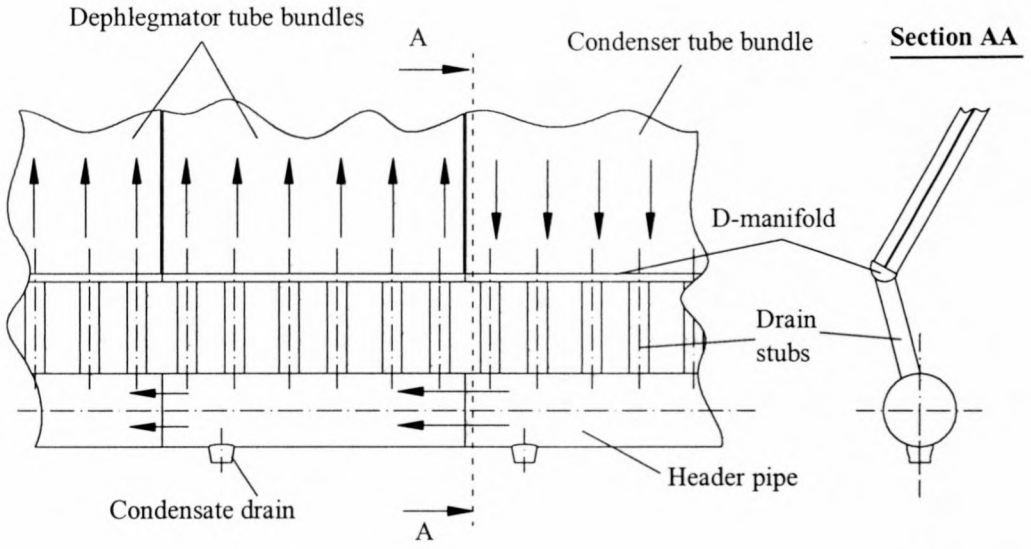

Figure 2.4: Illustration of an ACC system incorporating the D-type inlet manifold.

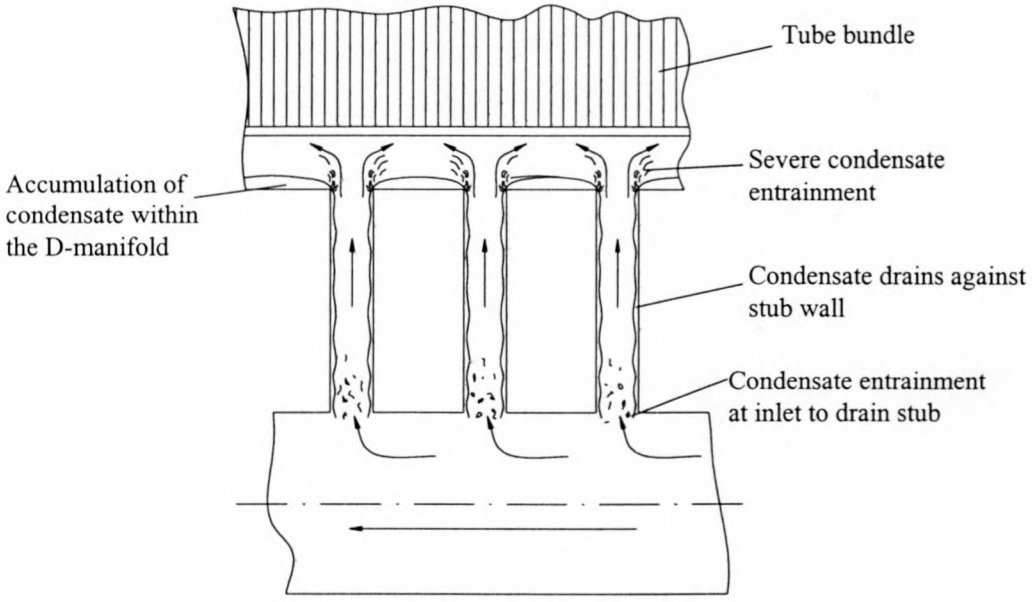

Figure 2.5: Schematic illustrating the accumulation of condensate within the D-manifold due to counter-current flow conditions within the drain stubs.

At full load operating conditions, the experienced two-phase counter-current flow conditions result in significant liquid entrainment at the respective in- and outlets to the drain stubs. As this phenomenon prevents the proper draining of condensate via the drain stubs, condensate is accumulated within the D-type inlet manifold and bundle

tubes as shown in figure 2.5. The accumulated condensate leads to an increase in turbine backpressure and aggravates the accumulation of non-condensables, forming dead-zones within the dephlegmator bundle tubes.

2.5.2 Box-type inlet manifold design

The box-manifold design, shown in figure 2.6, is an improvement on the D-type inlet manifold, as it ensures better liquid drainage from the bundle tubes and facilitates the easy assembly of the respective dephlegmator and condenser tube bundles. The upstream design of the box-manifold, however, still poses limitations on the effective operation of the dephlegmator tube bundles. This design causes flow separation and maldistribution in the upstream side of the manifold which may result in the formation of low pressure regions within the bundle tubes. Here non-condensables can accumulate to form dead-zones.

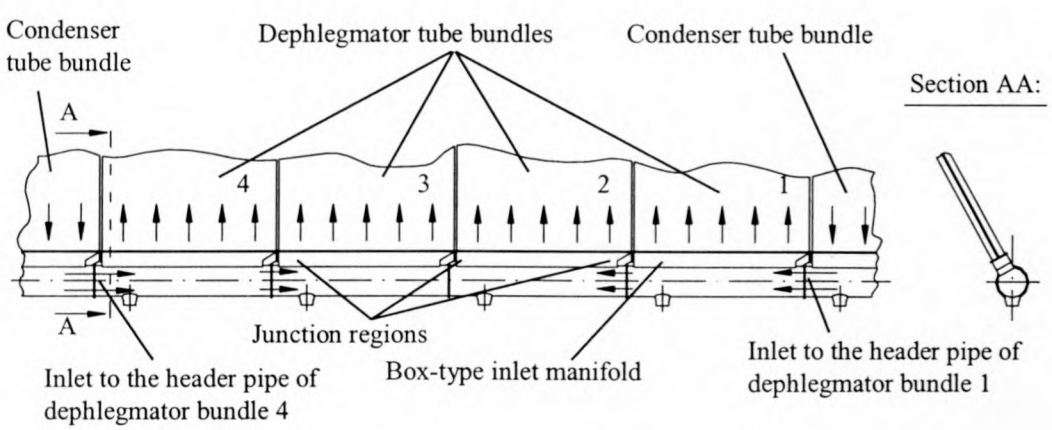

Figure 2.6: Schematics illustrating the different flow conditions experienced in the dephlegmator inlet manifolds.

In the case where a fan unit[2] situated near the middle of the ACC system acts as the dephlegmator, steam enters the dephlegmator from both sides of its header pipe. As shown in figure 2.6, different flow conditions are experienced within each of the

[2] A fan unit consists of a mechanically driven fan and its accompanying tube bundles.

respective dephlegmator inlet manifolds due to different gas flow rates and orientations with respect to the gas flow direction.

The steam mass flow at the inlet to the header pipes of tube bundles 1 and 4 approximately amounts to the steam mass condensed in two tube bundles. On the other hand, the steam mass flow entering the header pipes of manifolds 2 and 3 corresponds approximately to the steam mass condensed in a single tube bundle. This translates to an average steam velocity in the header pipes of manifolds 1 and 4, which is double the velocity in the header pipe of manifolds 2 and 3. The higher average steam velocity in the header pipes of bundles 1 and 4 causes greater flow distortions within their respective box-manifolds and has a subsequent greater influence on the performance of these tube bundles. Figure 2.7 shows a schematic of the dephlegmator tube bundles to illustrate the presence of potential dead-zones resulting from the box-type inlet manifold design.

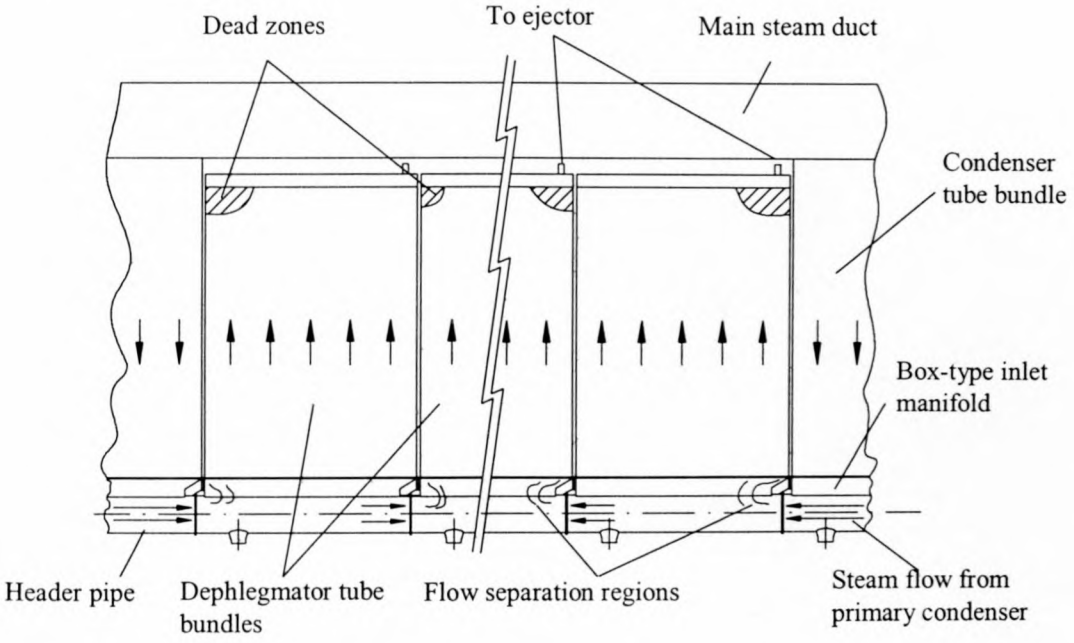

Figure 2.7: Schematics of an ACC system that utilises the box-type inlet manifold design.

Apart from actuating the formation of dead zones in the bundle tubes, the box-type inlet manifold also aggravates liquid entrainment at the tube inlets which are affected by the separated flow region. Entrained liquid may accumulate inside the bundle tubes and

cause an increase in the tube pressure drop of the affected tubes and aggravate tube row effects.

Scale models representing the D- and box-type inlet manifold designs were manufactured and tested in order to evaluate the influence of these designs on the entrance effects to dephlegmator tube bundles. The experimental apparatuses and test results are discussed in chapters 3 and 4 respectively.

CHAPTER 3

D-TYPE DEPHLEGMATOR INLET MANIFOLD FLOW CHARACTERISTICS

3.1 Introduction

A schematic of a dephlegmator system utilising the D-type inlet manifold design is shown in figure 2.4. This chapter discusses the results obtained from investigations conducted on an experimental D-type dephlegmator inlet manifold. These investigations were conducted in order to determine the influence of this specific design on the entrance effects[1] to its bundle tubes. Furthermore, the counter-flow conditions encountered between the draining liquid and gas supply were visualised in the drain stubs and D-type manifold. The experimental apparatus, observations and results obtained during the investigation are discussed.

3.2 Description of the experimental apparatus

The experimental apparatus used during the investigation was designed by Zapke [97ZA1] and is shown schematically in figure 3.1. A photograph of the experimental apparatus is shown in figure 3.2. Only a representative section of a full-scale dephlegmator unit was simulated by the experimental apparatus due to space limitations. Water and air are used to simulate representative dephlegmator operating conditions during a typical test run.

---

[1] Entrance effects are factors that influence the inlet pressure drop to the bundle tubes.

3.2.1 The test section

The test section of the experimental apparatus consists of an inlet header, a tube bundle and an outlet manifold as shown in figure 3.1. The inlet header in turn consists of the D-type inlet manifold, two drain stubs and the header pipe. To enable the visualisation of the two-phase counter-flow patterns within the inlet header, the D-type inlet manifold and the respective drain stubs are manufactured out of Perspex. Further visualisation of the flow patterns within the steel header pipe is made possible through a Perspex end flange, which is bolted onto the end of the header pipe.

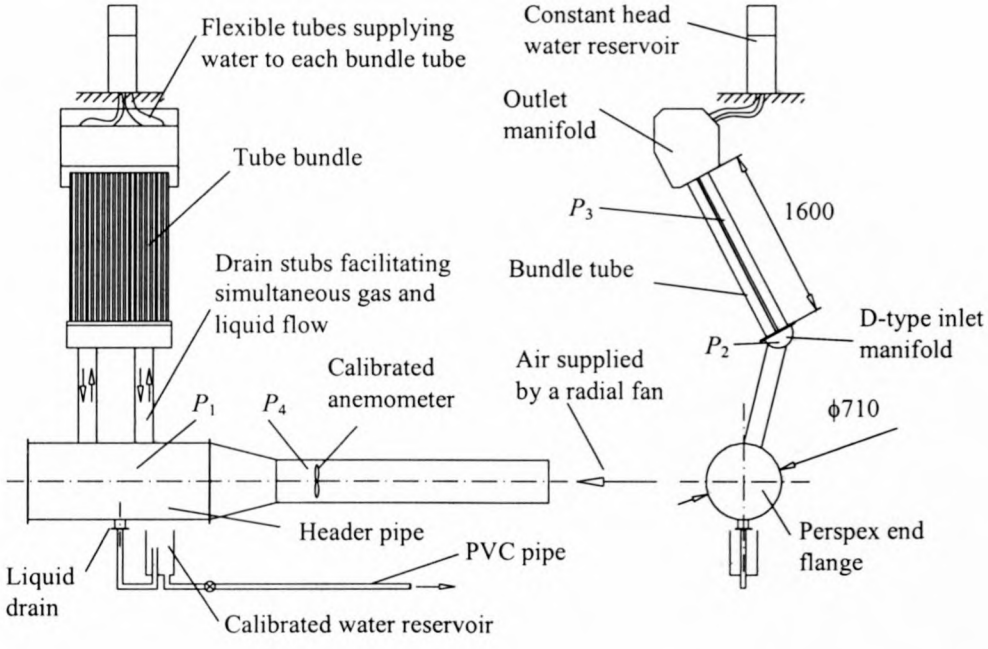

Figure 3.1: Schematics of the experimental apparatus used for the evaluation of the D-type inlet manifold.

The tube bundle consists of two tube rows, each having 19 elliptical tubes of length 1.6 m. All the relevant tube dimensions are presented in Appendix B. Each bundle tube is welded onto a 15 mm tube sheet, which is bolted onto the D-type inlet manifold. This forms the inlet to the tubes. The outlet of the bundle tubes is located within the outlet manifold which is constructed out of plywood and is open to the atmosphere. A scaffolding structure serves as a support for the apparatus and renders access to the constant head water reservoir at the top of the test section.

3.2.2 The water supply system

Flexible rubber tubes of equal length feed a constant water mass flow from a constant head water reservoir to each of the bundle tubes, thus simulating the condensate flow in the experimental apparatus. The water mass flow is set by adjusting the water head within the constant head water reservoir in order to present representative dephlegmator operating conditions. At the bottom of the header pipe, a liquid drain feeds the water to a calibrated water reservoir where the water flow rate can be measured by means of a stopwatch.

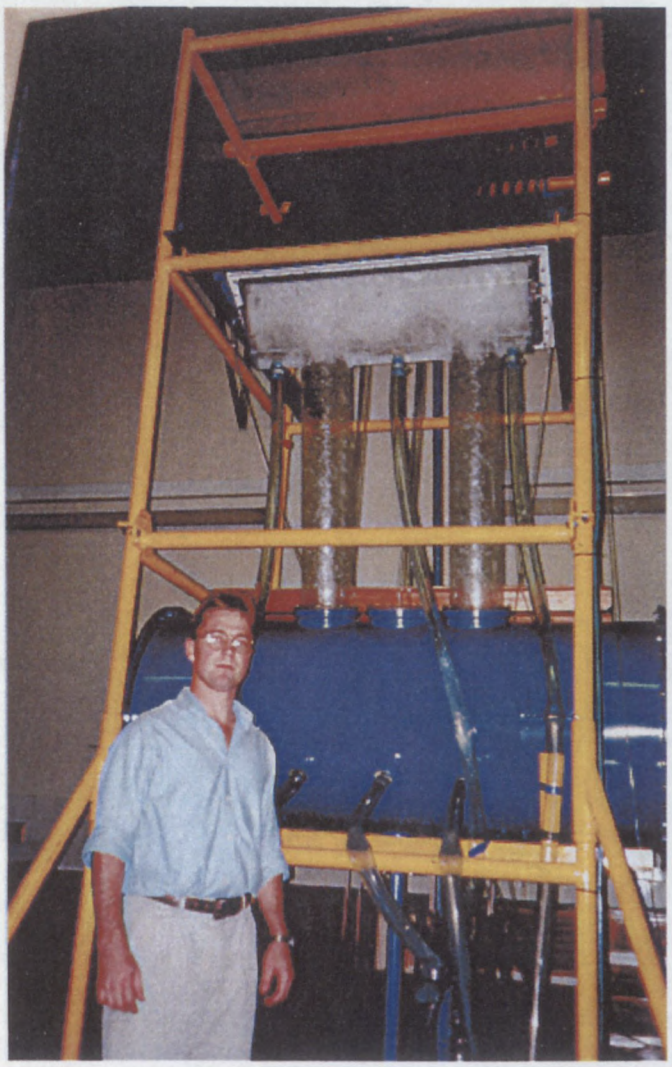

Figure 3.2: Photograph of the D-type inlet manifold experimental apparatus.

3.2.3 The air supply system

The steam flow through the dephlegmator is simulated by means of air that is supplied by a radial fan. Different operating conditions can be simulated in the test section by changing the air flow rate of the fan. Adjustment of the fan output is by means of an electrical variable speed control.

During a test run, the air supplied by the fan flows through the header pipe and drain stubs to the D-type inlet manifold. From within the D-type manifold the air enters each bundle tube to exit into the outlet manifold. As the air exits the tube bundle into the outlet manifold, the air velocity decreases due to the increase in cross-sectional area of the outlet manifold. This decrease in the air velocity ensures that the entrainment of liquid at the outlet of the bundle tubes is limited. From the outlet manifold, the air exits freely to the atmosphere.

3.2.4 Instrumentation

The total air mass flow rate is measured by an anemometer located within the experimental apparatus, as shown in figure 3.1. The anemometer was calibrated in a windtunnel prior to installation.

Type T thermocouples are used to measure the respective water temperature in the calibrated water reservoir and the air temperature at the location of the anemometer. These temperatures are used to determine the relevant fluid properties required by the investigation.

Pressure lines were connected to points P_1, P_2, P_3 and P_4 as shown in figure 3.1, in order to measure the required pressure differentials by means of six inductive-type *Hottinger Baldwin Messtechnick PD1 (HBM PD1)* differential pressure transducers. A *KWS 3073 Hottinger Baldwin Messtechnick* bridge amplifier amplifies the output of the pressure transducers to yield 0 to 10 V voltage signals. Prior to the investigation, the pressure transducers were calibrated by means of a *Betz* water manometer.

3.3 *Discussion of experimental results*

According to the flooding prediction presented by Zapke [97ZA1], dephlegmator bundle tubes utilising finned tubes of similar design to the tubes used in the experimental apparatus, should flood at a densimetric gas Froude number at the inlet to the bundle tubes in the range of $Fr_{Hsg} = 0.4$ to 0.5. As shown in figures 3.6 and 3.7, a dramatic increase in the respective stub and tube pressure differentials (Δp_{12} and Δp_{23}) is however noted at a tube densimetric gas Froude number in the order of 0.07.

At this operating condition ($Fr_{Hsg} = 0.07$), severe liquid entrainment at the in- and outlets of the drain stubs as well as at the inlet to the bundle tubes is noted. The severe entrainment results in the accumulation of liquid within the D-manifold and bundle tubes, which explains the sudden increase in the stub and tube pressure differentials shown in figures 3.6 and 3.7 respectively.

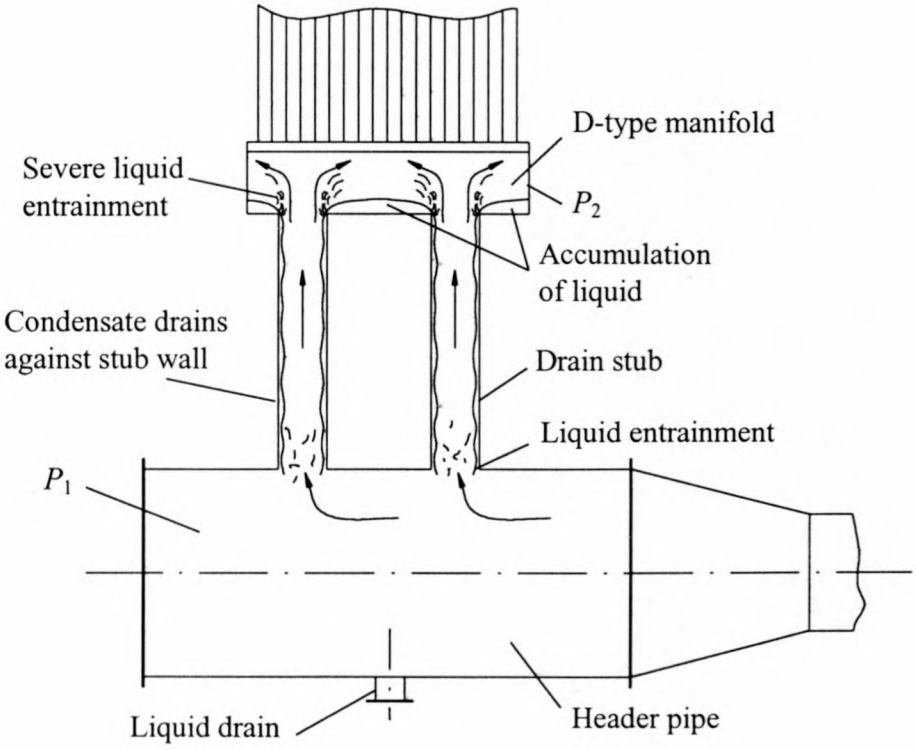

Figure 3.3: Schematic of the experimental D-type inlet manifold illustrating the accumulation of liquid within the D-manifold.

Figure 3.3 shows the visualised flow conditions within the D-type inlet manifold and drain stubs at operating conditions yielding a densimetric gas Froude number of $Fr_{Hsg} \approx 0.07$. Figure 3.3 clearly shows the experienced liquid accumulation within the D-manifold.

Kröger and Zapke [98KR2] proposed a modification to the present D-type manifold design as shown in figures 3.4 and 3.5. Drainage holes were drilled into the bottom of the D-type manifold to enable liquid drainage into a secondary manifold fixed below the original D-manifold. From within this secondary manifold, the liquid drains by means of flexible U-tube drain pipes into the header pipe. The liquid head within the U-tube drain pipes eliminates any gas flow in the flexible U-tube drain pipes.

The principle of this modification rests on the total separation of the phases at high condensation rates. Consequently, only gas (steam) flows upward through the existing drain stubs and liquid (condensate) drains back through the flexible U-tube drain pipes. Single-phase flow is thus created, and the troublesome counter-current steam-condensate flow is eliminated.

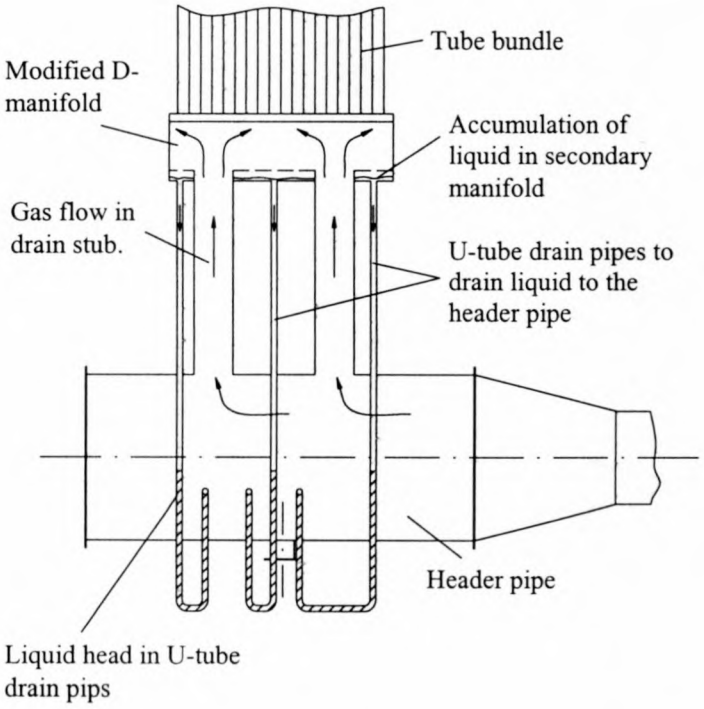

Figure 3.4: Schematic of the experimental apparatus with the modified D-manifold.

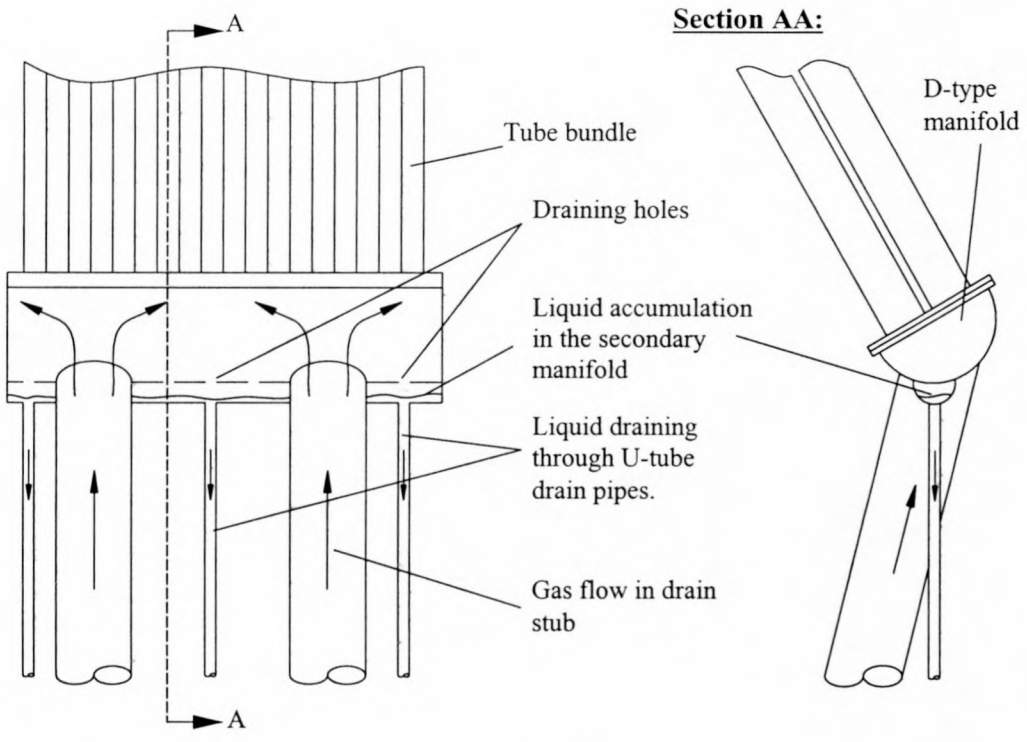

Figure 3.5: Schematics of the modified D-manifold.

Figures 3.6 and 3.7 show the respective stub- and tube pressure drop results (Δp_{12} and Δp_{23}) obtained during the investigation. Fr_{Hsg} is the densimetric gas Froude number at the inlet to the bundle tubes. These results were obtained at operating conditions where the superficial liquid velocity in the tube bundle of v_{sl} = 0.006 m/s. Equation (3.1) is used to calculate v_{sl}.

$$v_{sl} = \frac{m_l}{\rho_l A_{tc}} \tag{3.1}$$

From figure 3.6, it is clear that the sudden increase in the stub pressure drop, Δp_{12}, associated with flooding is not present in the case of the modified D-type inlet manifold. The subsequent tube pressure drop results, Δp_{23}, are shown in figure 3.7. Once again, the influence of the modified D-manifold is evident as the sudden increase in the tube pressure drop due the accumulation of liquid within the tubes is eliminated.

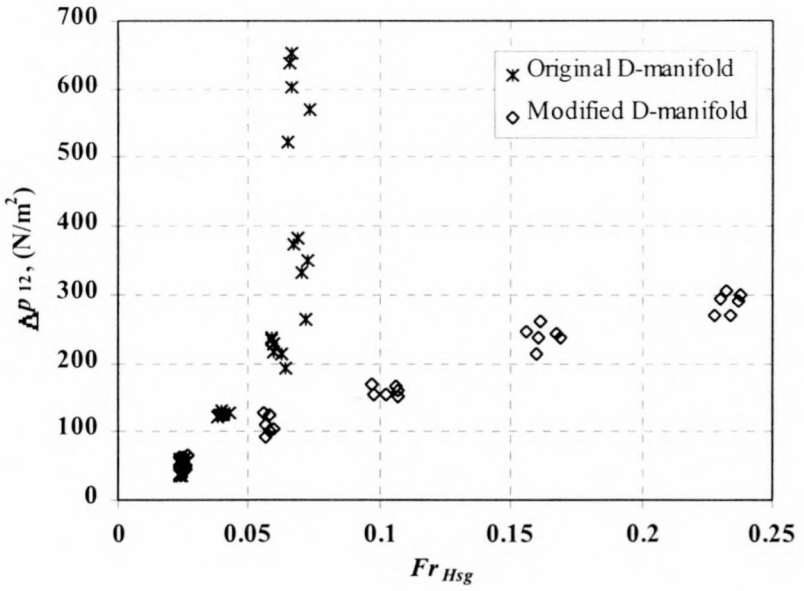

Figure 3.6: Comparison between the drain stub pressure drop results obtained from the original and modified D-manifold investigation.

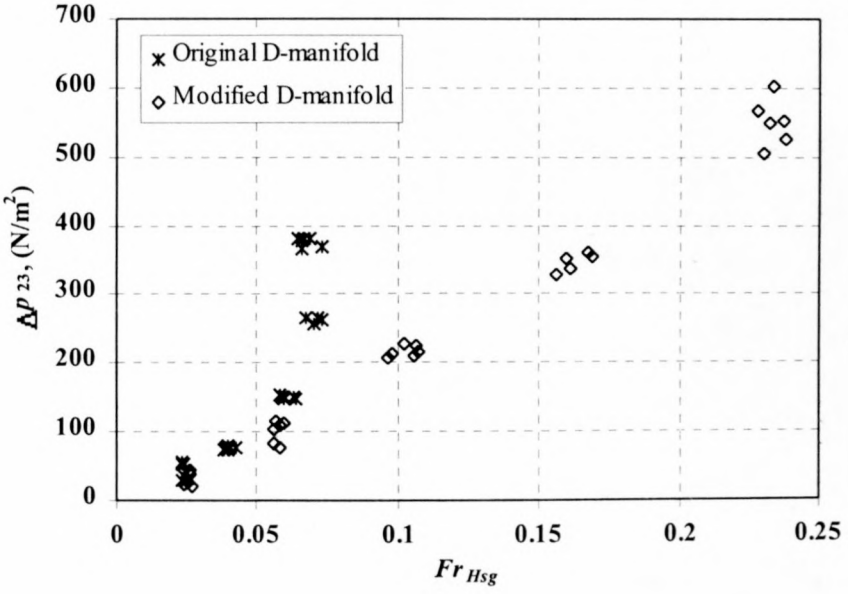

Figure 3.7: Comparison between the bundle tube pressure drop results obtained from the original and modified D-manifold investigation.

3.4 Field tests conducted on a particular dephlegmator with a D-type inlet manifold

The proposed modification to the D-type inlet manifold (discussed in the previous section) was implemented on a dephlegmator tube bundle of an ACC system of a particular power station. Field tests were conducted by Zapke [98ZA1] to investigate the influence of the modification on the dephlegmator's operation.

During these field tests the heat rejected by two adjacent dephlegmator tube bundles, one being the modified tube bundle, was determined by measuring the air outlet velocity and temperature distribution of the tube bundles. These measurements were made by a set of thermocouples and anemometers fixed onto a beam that was traversed vertically across the face of the tube bundles. Two 20-channel *Schlumberger IMPs* (Isolated Measurement Pod) and a personal computer were used for the data logging.

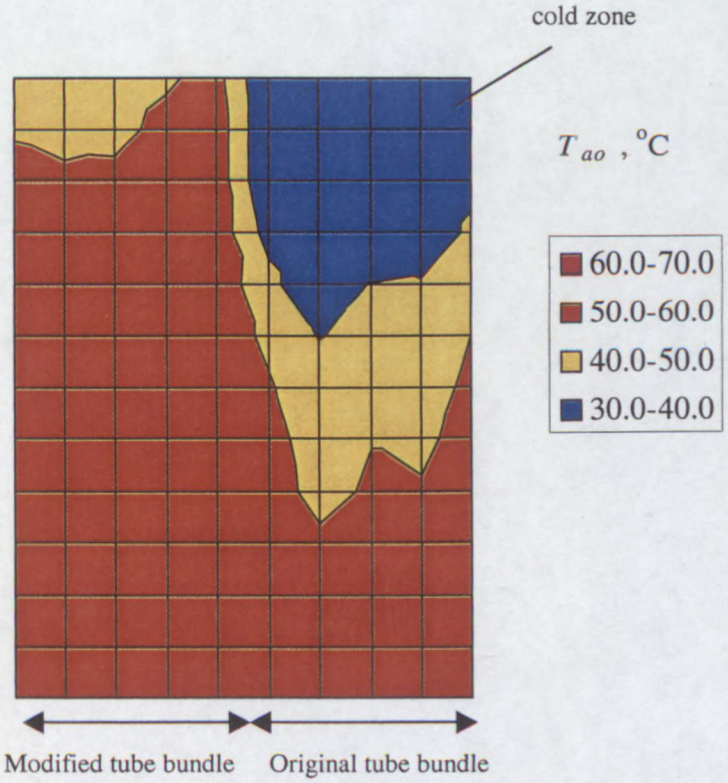

Figure 3.8: Outlet air temperatures of two dephlegmator tube bundles, illustrating the difference in the heat transfer capability of the bundle with the modified D-type header compared to the original design.

Figure 3.8 shows a graph representing the outlet air temperatures that were recorded during a specific test run. These results show a notable improvement in the heat transfer capabilities of the tube bundle with the modified inlet manifold, as compared to the tube bundle with the original inlet manifold design.

The presence of a so-called cold zone in the tube bundle with the original inlet manifold design, is clearly visible as indicated by the bundle area rendering an outlet air temperature in the order of T_{ao} = 30 to 40 °C. The outlet temperature in this region, which is approximately equal to the ambient air temperature, proves the poor heat transfer characteristics of the bundle tubes located in this region.

The analysis conducted on the D-type dephlegmator inlet manifold clearly shows the importance of proper inlet manifold design. Designs that do not facilitate the effective drainage of condensate while simultaneously supplying the bundle tubes with the required steam flow, will lead to inefficient dephlegmator operation.

CHAPTER 4

BOX-TYPE DEPHLEGMATOR INLET MANIFOLD FLOW CHARACTERISTICS

4.1 Introduction

Figures 2.6 and 2.7 show the schematics of an A-configuration dephlegmator system, utilising a box-type inlet manifold design. Each dephlegmator unit comprises eight tube bundles (four tube bundles on each side of the unit), each with its box-type inlet manifold. The different flow conditions encountered in each of these manifolds are also indicated.

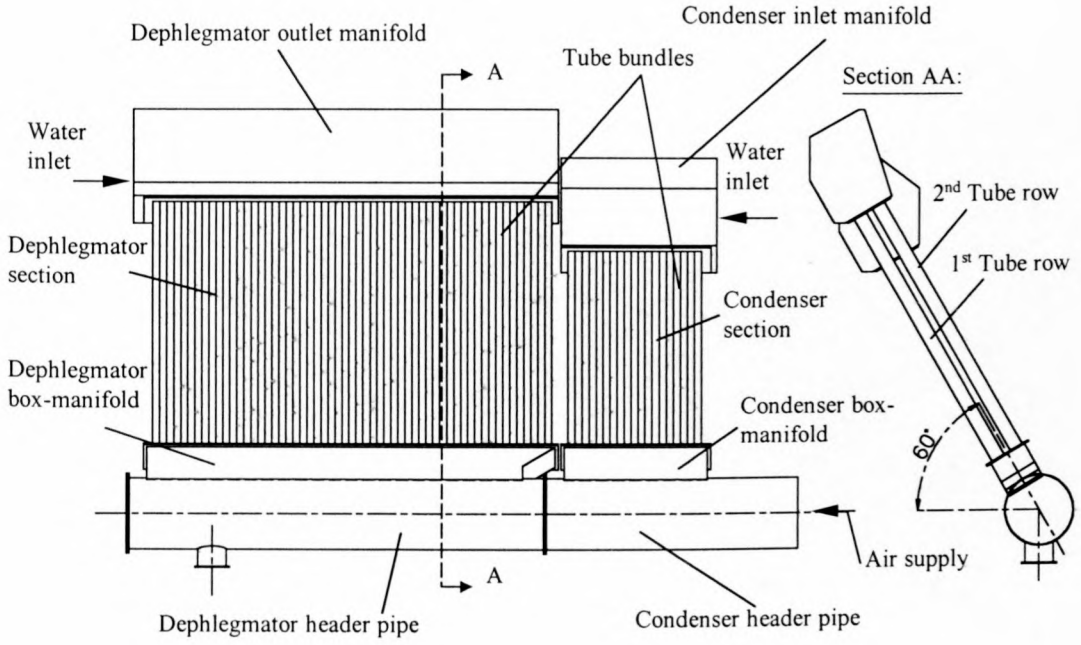

Figure 4.1: Experimental test section, used to conduct the investigation on the influence of the box-manifold design on dephlegmator operation.

An experimental apparatus, shown in figure 4.1, was designed and constructed in order to evaluate the influence of the various flow conditions within the dephlegmator inlet

manifolds on the inlet pressure drop to the dephlegmator bundle tubes. The static pressure drop across the inlet to the dephlegmator header pipe and its tube bundles is also investigated and presented in terms of a dimensionless, header pressure loss coefficient.

A photograph of the experimental apparatus is shown in figure 4.6. The operation of a dephlegmator tube bundle is simulated during a test run by using air and water as working fluids. This section discusses the experimental apparatus as well as the results obtained during the investigation.

4.2 Description of the experimental apparatus

To enable flow visualisation within the respective dephlegmator inlet- and condenser outlet headers, transparent Perspex was used for the construction of the headers. Each header consists of a header pipe and its accompanying box-type inlet manifold.

During a typical test run, the pressure differentials between the tube static- and atmospheric pressure, as well as the gas velocities within selected tubes are measured. These values are used to indicate the influence of the flow distribution within the dephlegmator box-manifold, on the inlet to its bundle tubes. Furthermore, the pressure differentials between the static pressure at the inlet to the dephlegmator header pipe and the static pressure within the bundle tubes were also measured. These pressure differentials are used to present the pressure distribution within the dephlegmator inlet header in terms of a header loss coefficient, K_h.

4.2.1 Experimental test section

The experimental test section, as shown in figure 4.1, consists of a partially modelled dephlegmator- and condenser test section, which is assembled within a steel structure. The steel structure serves as a support for the apparatus, and renders easy access to the top of the test section and the respective water supply systems.

The condenser test section:

This section consists of a condenser header pipe with its box-manifold, a tube bundle and the condenser inlet manifold. The influence of the inlet manifold design on the flow distribution within the dephlegmator is the focus of the investigation. Therefore the condenser section is only partially simulated. Figure 4.2 shows detailed sketches of the condenser outlet header with its box-type manifold, which is constructed of Perspex to enable flow visualisation.

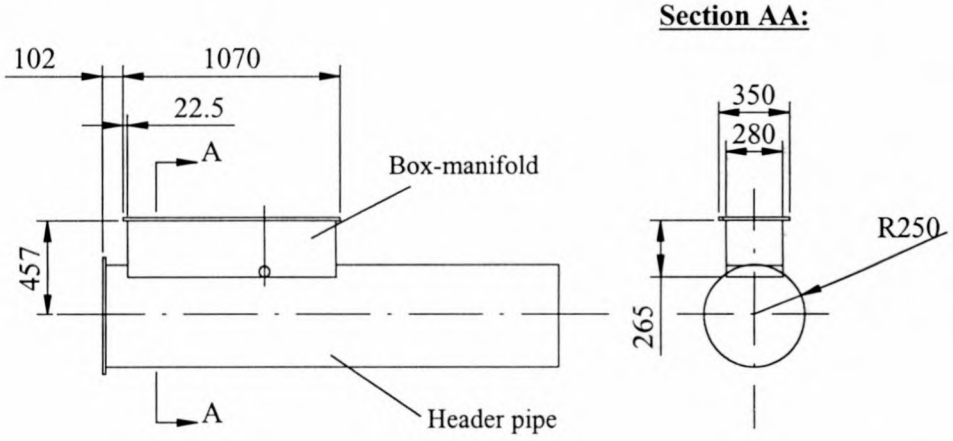

Figure 4.2: Detailed sketch of the Perspex condenser outlet header with its box-manifold.

A tube bundle with two staggered elliptical condenser tube rows is bolted onto the box-manifold flange. A tube row consists of 19 tubes each 1.6 m in length. Figure B.1 shows a detailed sketch of an elliptical finned tube cross-section, as used in the respective tube bundles of the test section. The air inlet to the condenser tubes is located at the top of the condenser tube bundle, inside the condenser inlet manifold, which is designed to ensure an even air flow distribution to the bundle tubes. A constant water mass flow rate is supplied to each bundle tube by means of a water dividing header, which is also situated inside the condenser inlet manifold.

The dephlegmator test section

This section consists of a dephlegmator inlet header and its box-type manifold, with dimensions corresponding to those of a full-scale dephlegmator, a tube bundle and an outlet manifold, as shown in figure 4.1. Details of the inlet header and box-manifold

are shown in figure 4.3. A tube bundle with two staggered rows of elliptical tubes, similar to the tubes used in the condenser test section, is bolted onto the box-manifold. The first tube row consists of 57 tubes and the second tube row of 58 tubes each 2m long. The dephlegmator tubes open to an outlet manifold, which is open to the atmosphere. A water dividing header, which supplies each tube with a constant water mass flow, is situated inside the dephlegmator outlet manifold.

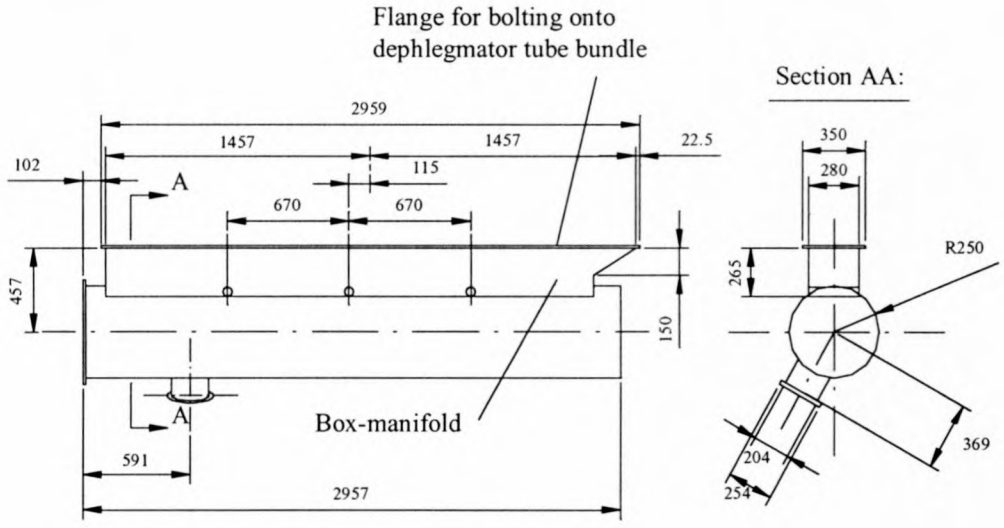

Figure 4.3: Detailed sketch of the dephlegmator inlet header.

4.2.2 Air supply

Figure 4.4 shows the air supply system that simulates the steam flow through a typical dephlegmator of similar design. Air is supplied to the test section by means of a radial fan, which is part of an atmospheric open-loop induced windtunnel. Figure C.1 shows a schematic of the windtunnel [98KR1]. A radial fan draws air uniformly through the rounded inlet section, where its wet- and dry bulb temperature is measured. To measure the air mass flow through the windtunnel, the relevant pressure differentials across one or more elliptical nozzles mounted inside the windtunnel are measured. A sample calculation of the air mass flow through the tunnel and a description of the windtunnel is given in Appendix C. The airflow can be varied by means of a throttle valve and / or by opening a selection of the elliptical nozzles within the windtunnel.

At the windtunnel outlet, the desired airflow distribution through the condenser and dephlegmator sections is adjusted by dividing the outlet air stream from the windtunnel by means of a door-valve, as illustrated in figure 4.4. One part of the airflow is supplied to the condenser header pipe and the other part to the condenser inlet manifold through flexible hoses. A calibrated anemometer is used to measure the airflow supplied to the condenser inlet manifold.

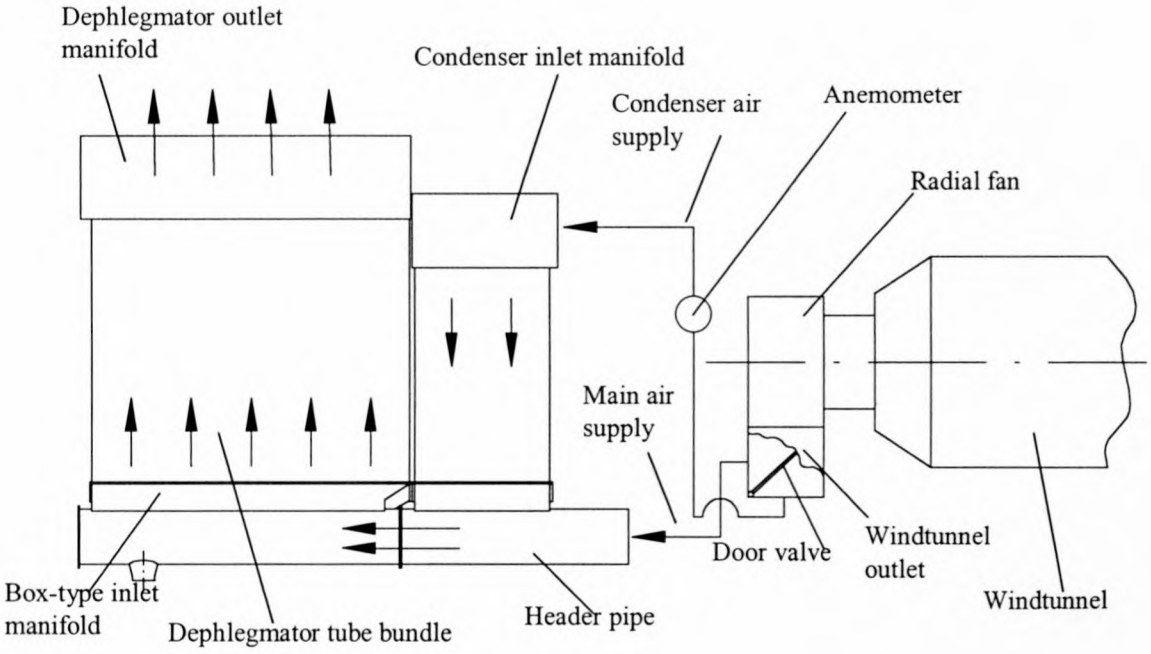

Figure 4.4: Schematics of the air supply system.

In the condenser section, air flows from the inlet manifold through the elliptical condenser tubes and exits in the condenser box-manifold where it rejoins the main air supply. From the condenser header pipe the air flows to the dephlegmator header pipe, from where it is fed to the dephlegmator bundle tubes via the box inlet manifold. The dephlegmator tubes join into the outlet manifold, which is open to the atmosphere.

4.2.3 Water supply

As shown in figure 4.5, a water pump circulates water from the main water reservoir through the test section to simulate the condensate flow through the dephlegmator. Each of the experimental dephlegmator- and condenser test sections has its own water supply system consisting of a constant head water reservoir and a dividing header. Two

gate valves located at the pump outlet are used to control the water flow rate through the respective sections.

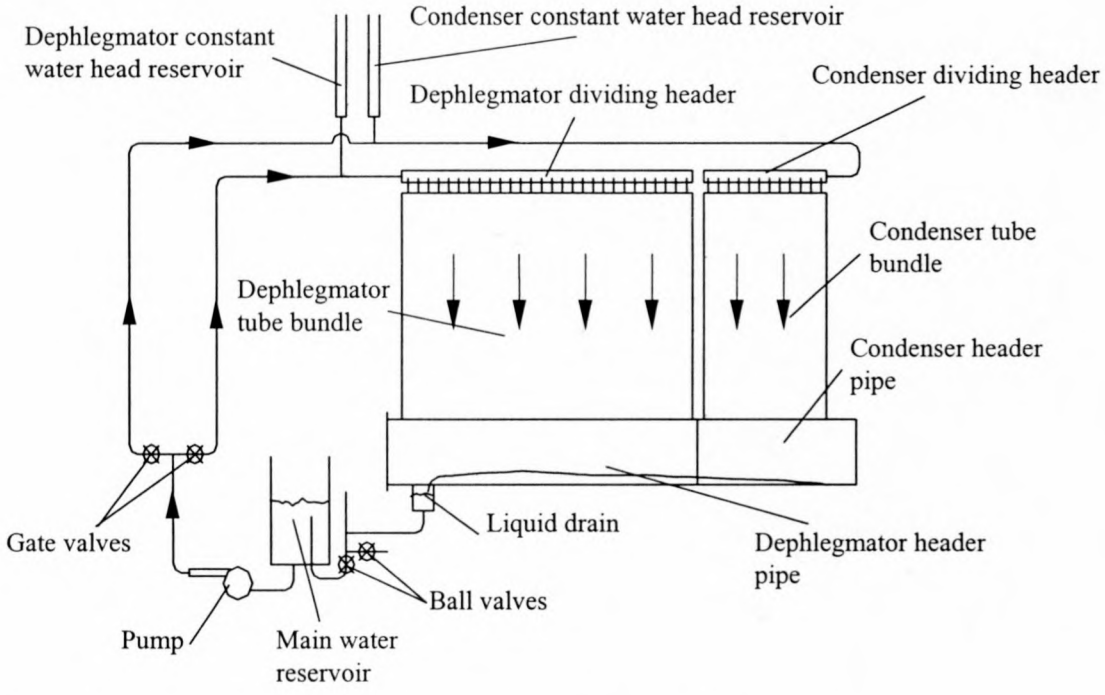

Figure 4.5: Schematics illustrating the test section water flow loop.

Water is pumped from the main reservoir to each of the two test section's constant head water reservoir, from where it flows through a PVC pipe system to the respective dividing headers. Rubber feeder tubes supply each bundle tube with water at a constant flow rate from the dividing header. A photograph of the dividing header along with its rubber feeder tubes is shown in figure 4.7.

From the top of the elliptical bundle tubes the water drains downward to the respective condenser- and dephlegmator header pipes by means of gravity. By varying the water head in a section's constant head water reservoir, the water mass flow through the section is varied. The maximum available head is 2.5 m, which renders a superficial tube velocity, v_{sl}, of 0.012 m/s. Inside the respective condenser- and dephlegmator header pipes the water accumulates and drains through the liquid drain back to the main water reservoir.

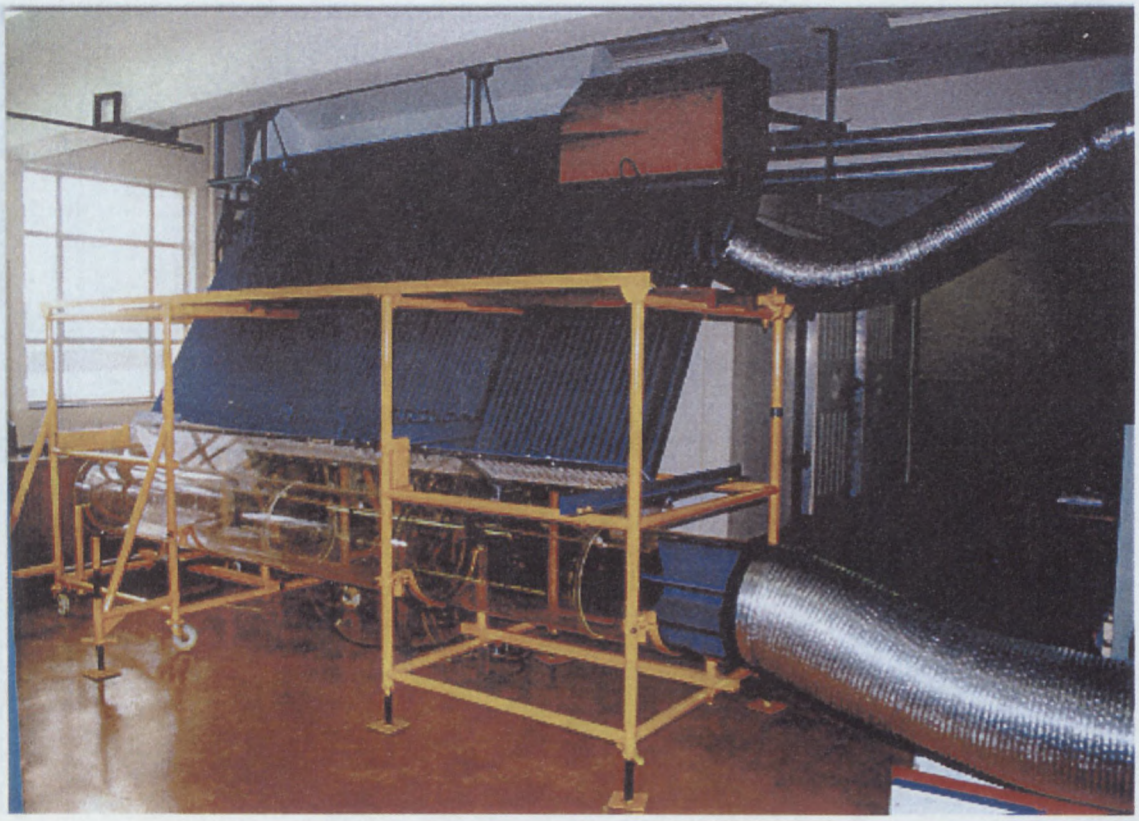

Figure 4.6: Photograph of the box-type inlet manifold experimental apparatus.

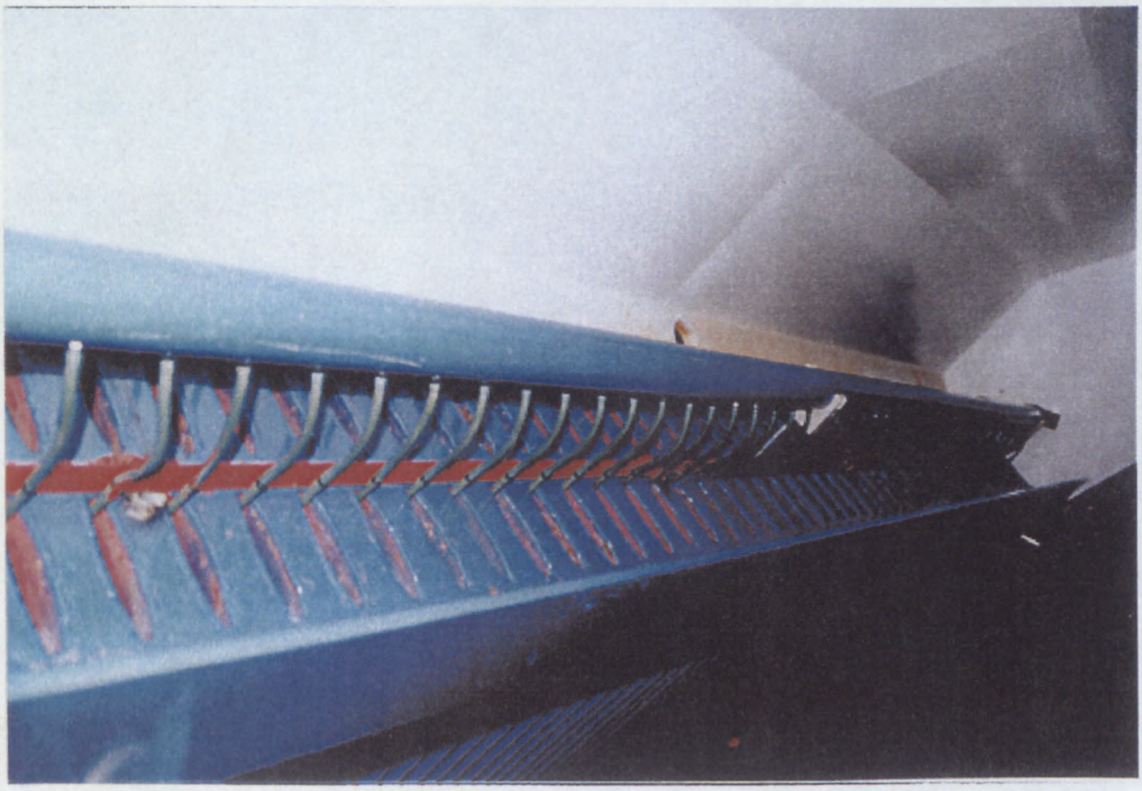

Figure 4.7: Photograph of the water dividing header.

4.2.4 Instrumentation

Copper-constantan thermocouples are used to measure the temperature of the air at the inlet to the windtunnel, the air flowing across the anemometer and the water temperature in the main reservoir. These temperatures are measured in order to calculate the applicable thermophysical properties required for the respective air- and water mass flow calculations.

Two *Endress and Hauser Deltabar PMD 130* differential pressure transducers measure the pressure differentials required to monitor the air mass flow through the windtunnel. One pressure transducer measures the pressure differential across the elliptical windtunnel nozzles and the other measures the pressure differential between the static, upstream nozzle pressure and the ambient pressure. The air flow to the condenser section is monitored by means of an anemometer. The anemometer was calibrated in a windtunnel prior to its installation within the experimental apparatus.

The maximum outlet bundle tube velocity is used as reference velocity in the calculation of the header loss coefficient and is measured by means of a hot-wire anemometer. Prior to the investigation the hot-wire anemometer was calibrated in the windtunnel, and its readings were found to be accurate.

In order to evaluate the influence of the air flow distribution inside the dephlegmator box-manifolds on the inlet loss coefficients to the bundle tubes, the pressure differentials between the inside of the bundle tubes and the atmosphere are measured. Pressure tappings were manufactured from Perspex and secured onto the front of selected bundle tubes, at a distance of 200 mm above the inlet to the tubes. Figures 4.9 and 4.11 show the location of the pressure tappings on the bundle tubes, while figure 4.8 shows a detailed sketch of such a pressure tapping. All the pressure tappings were connected to three pressure selection boxes by means of pressure lines. Each of the pressure selection boxes contains 10 channels that were connected in series. The output of the selection boxes was connected to a *Betz* manometer to read the selected output pressure differentials.

Prior to each test, the respective water flow rates of the test section are calibrated by measuring the mass and time taken to fill a bucket with outlet water from the dephlegmator drain stub.

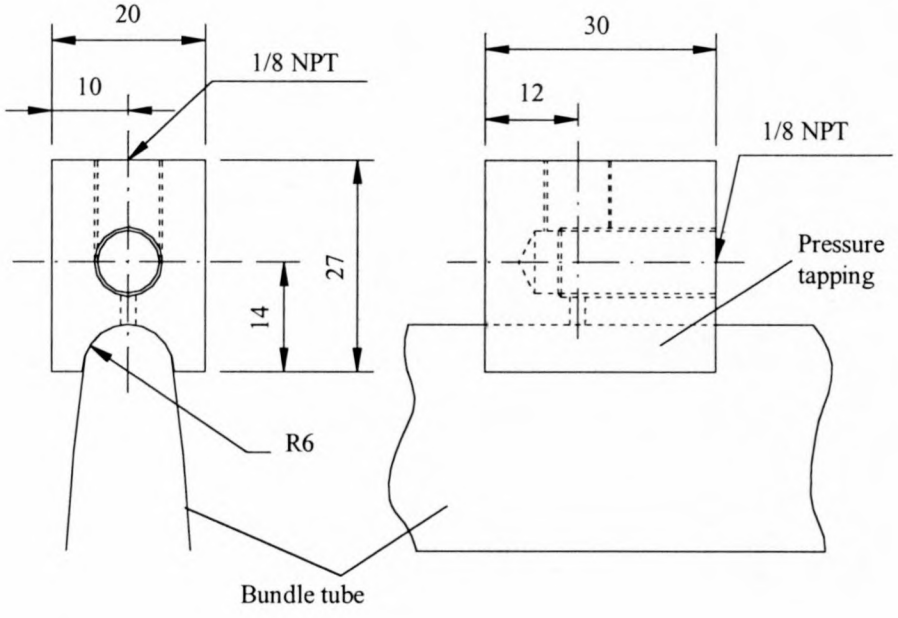

Figure 4.8: Tube pressure tap detail drawing.

4.3 Presentation of the experimental data

Observed flow distortions within the dephlegmator inlet header, a result of the box-manifold design, influence the pressure distribution within the dephlegmator inlet header and the entrance[1] effects to the bundle tubes situated in the upstream box-manifold region. K_{h2} is a dimensionless pressure loss coefficient that is derived in order to present the pressure differential between the static pressure at the inlet to the header pipe and the pressure within the bundle tubes.

Figure 4.9 shows a side view of the dephlegmator test section, indicating the different locations at which the relevant pressure measurements are taken. The pressure tappings, at section 2 on the tube bundles, are located 200 mm above the inlet to the tubes.

[1] Entrance effects: Factors that influence the inlet pressure drop to the bundle tubes.

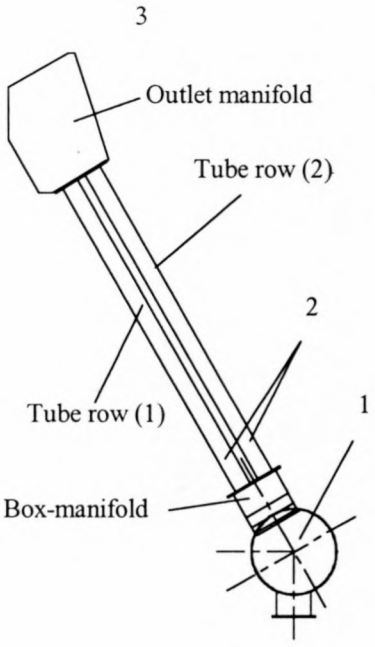

Figure 4.9: Schematic of the dephlegmator test section illustrating the different cross-sections at which the tube flow characteristics were evaluated.

4.3.1 Dephlegmator inlet header loss coefficient

The static pressure loss between the header pipe and the bundle tubes (sections 1 and 2 as shown in the schematic of the experimental apparatus presented in figure 4.10), is presented in terms of a dimensionless inlet header loss coefficient, K_{h2}. This section illustrates the derivation of K_{h2}.

During a typical test run, the static pressure differential between the atmospheric pressure 3 and the dephlegmator header pipe pressure 1, is measured as Δp_{13}. Similarly, the pressure differential between the atmospheric pressure 3 and the static bundle tube pressure 2, is measured as Δp_{23}.

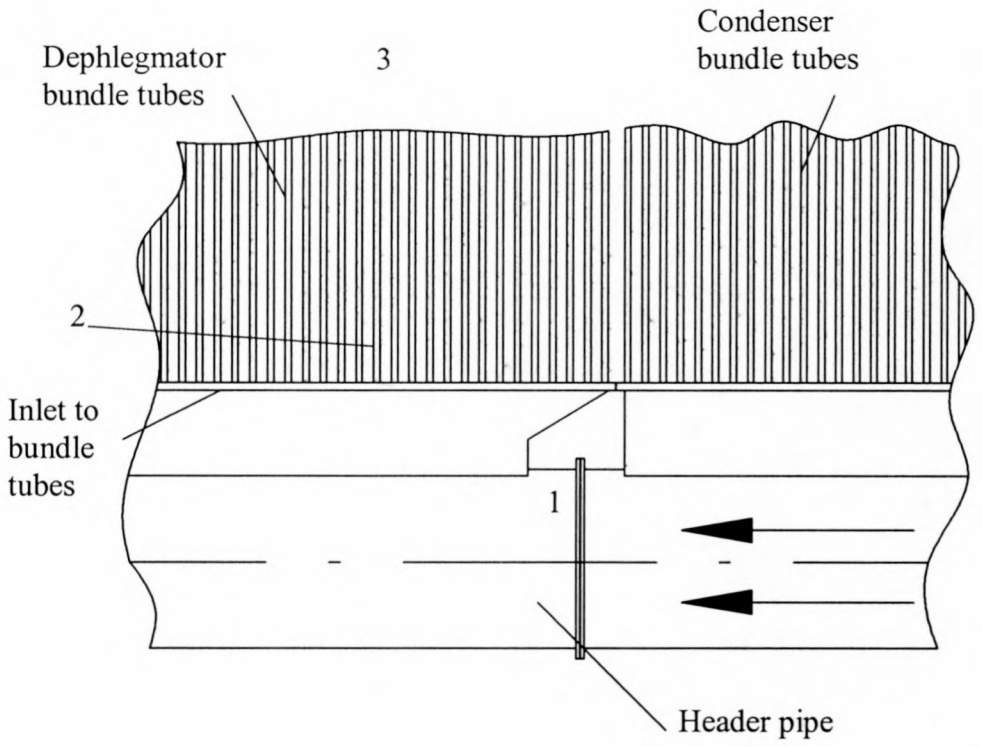

Figure 4.10: A schematic of the experimental apparatus, illustrating the locations at which the respective pressure differentials are measured.

According to Kröger [98KR1], the pressure loss between the sections indicated in figure 4.10 can be presented as follows:

Sections 1 and 2:

$$\left(p_1 + \tfrac{1}{2}\rho v_1^2\right) - \left(p_2 + \tfrac{1}{2}\rho v_2^2\right) = \tfrac{1}{2}\rho v_1^2 K_{h2} \tag{4.1}$$

where v_2 is the superficial tube gas velocity and v_1 the superficial gas velocity within the header pipe.

Sections 2 and 3:

$$\left(p_2 + \tfrac{1}{2}\rho v_2^2\right) - p_3 = \tfrac{1}{2}\rho v_2^2 K_f + \tfrac{1}{2}\rho v_2^2 K_e \tag{4.2}$$

Upon addition of equations (4.1) and (4.2), the following is obtained.

$$p_1 - p_3 = \tfrac{1}{2}\rho v_1^2 K_{h2} + \tfrac{1}{2}\rho v_2^2 \left[K_f + K_e\right] - \tfrac{1}{2}\rho v_1^2 \tag{4.3}$$

Substituting equation (4.2) into equation (4.3), the following expression for K_{h2} is derived:

$$K_{h2} = \frac{(p_1 - p_3) - (p_2 - p_3) - \tfrac{1}{2}\rho v_2^2}{\tfrac{1}{2}\rho v_1^2} + 1 \tag{4.4}$$

4.4 Discussion of experimental results

Firstly, the influence of the condenser test section on the flow distribution within the dephlegmator inlet header and the subsequent influence on the entrance effects to the bundle tubes are discussed. Refer to figure 4.1 for the schematics of the experimental apparatus that illustrates the mentioned test sections. The influence of the dephlegmator header pipe gas velocity and inlet header geometry on the operation of the dephlegmator tube bundles are discussed in sections 4.4.2 and 4.4.3 respectively.

4.4.1 The influence of the condenser unit on the flow distribution within the dephlegmator box-manifold

By adjusting the door valve at the outlet of the windtunnel (refer to figure 4.4), the air flow rate through the condenser tube bundle, and subsequently the ratio between the superficial condenser outlet- and dephlegmator inlet velocities, v_{sco}/v_{sdi}, can be altered. Two operating conditions ($v_{sco}/v_{sdi} = 0$ and $v_{sco}/v_{sdi} = 0.333$) are evaluated in order to determine the influence of the gas flow in the condenser section on the flow distribution within the box-manifold of the dephlegmator test section. The operating conditions that are simulated during these tests, are such that the average densimetric gas Froude number at the inlet to the bundle tubes is $Fr_{Hsg} = 0.2$, as calculated by means of equation (2.1).

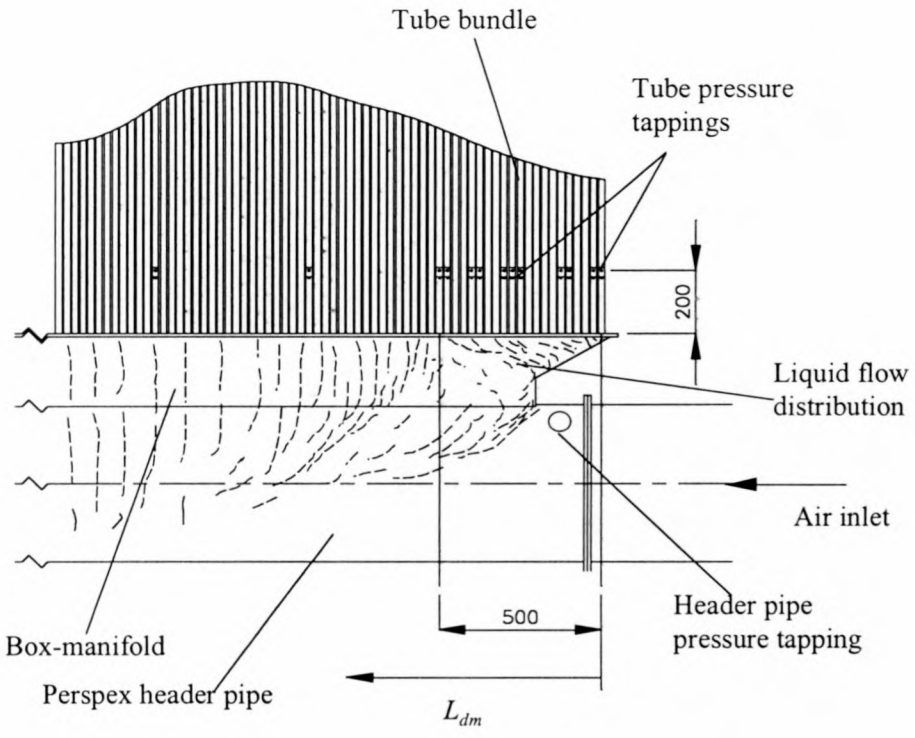

Figure 4.11: Liquid flow visualisation within the box-manifold.

The visualised liquid flow patterns within the box-manifold of the dephlegmator test section is shown in figure 4.11, and clearly shows flow separation in the upstream side of the box-manifold. The size of the flow separation area on the upstream side of the box-manifold is found to be in the order of L_{dm} = 0.5m. L_{dm}, is the downstream manifold distance as measured from the centre of the first tube in the second tube row of the dephlegmator tube bundle. The locations of the bundle tube- and header pipe pressure tappings are also indicated in this figure.

Figure 4.12 shows the measured pressure differentials between the static pressure within the selected bundle tubes and the atmospheric pressure, Δp_{23}, for operating conditions where $v_{sco}/v_{sdi} = 0.333$ and $v_{sco}/v_{sdi} = 0$. The pressure differentials are presented in terms of the downstream manifold distance, L_{dm}. From this figure, the influence of the flow distribution on the pressure differentials measured for the bundle tubes located in the upstream side of the box-manifold is evident.

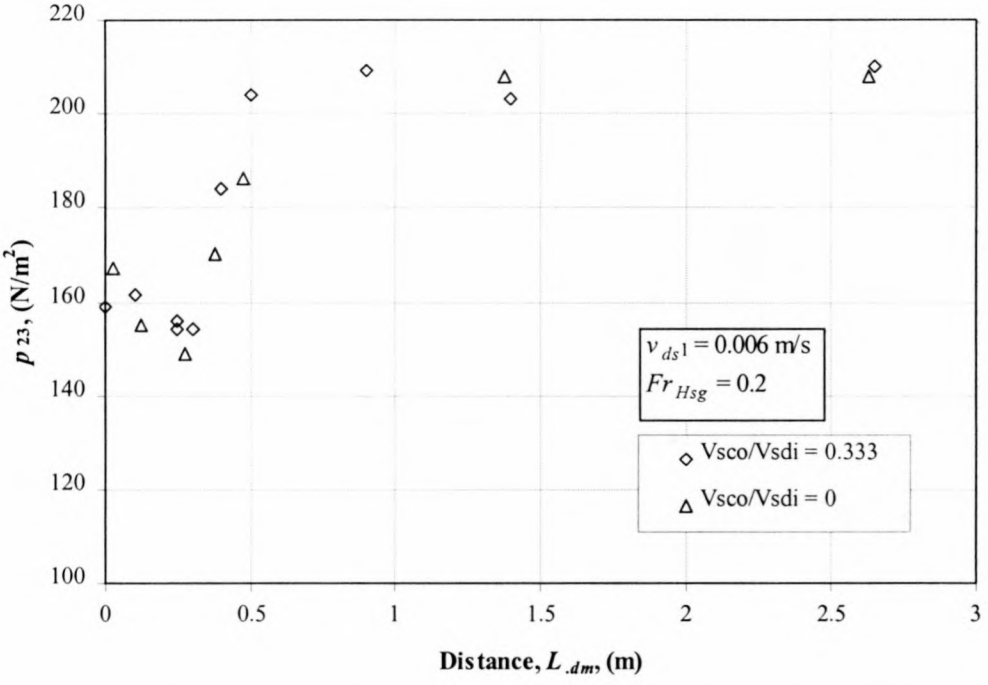

Figure 4.12: Tube pressure differential results for experimental operating conditions where $v_{sco}/v_{sdi} = 0.333$ and $v_{sco}/v_{sdi} = 0$.

These results show that the gas flow rate in the condenser section adjacent to the dephlegmator tube bundle has no significant influence on the flow distribution within the box-manifold. It can therefore be stated that the experienced box-manifold flow distortions, and subsequent influence on the inlet loss coefficient to the dephlegmator bundle tubes, are essentially a function of the vapour velocity within the header pipe at the upstream side of the box-manifold. The influence of the header pipe gas velocity and inlet header geometry on the flow distribution within the box-manifold, is therefore evaluated in the following section.

4.4.2 *The influence of the dephlegmator header pipe gas velocity on the entrance effects to the bundle tubes*

Figures 2.6 and 2.7 show the schematics of a particular A-configuration ACC unit with a dephlegmator fan unit utilising eight tube bundles (four tube bundles on each side of the unit), each with its own box-type inlet manifold and header pipe. Due to different

vapour velocities encountered in the header pipes of each inlet header and the geometry of the box-type inlet manifold, the flow conditions in each of the inlet manifolds differ.

Typical dephlegmator operating conditions render a header pipe Reynolds number at the inlet to the header pipes of tube bundles 1 and 4 in the order of $Re_{hp} \approx 650000$, and to tube bundles 2 and 3 in the order of $Re_{hp} \approx 350000$. (Refer to figure 2.6 for the schematics of the particular dephlegmator unit). The following equation gives the Reynolds number, Re_{hp}, at the inlet to the dephlegmator header pipe in terms of the gas velocity v_{ghp} and the header pipe diameter, d_{hp}.

$$Re_{hp} = \frac{\rho_g v_{ghp} d_{hp}}{\mu_g} \tag{4.5}$$

The header pipe gas velocity is given by the following equation,

$$v_{ghp} = \frac{m_g}{\rho_d \frac{\pi}{4} d_{hp}^2} \tag{4.6}$$

where m_g is the total air mass flow rate supplied by the wind tunnel to the experimental apparatus.

Due to a limited air mass flow supply of the windtunnel to the experimental apparatus, the maximum Reynolds number that could be obtained at the inlet to the dephlegmator header pipe ranged in the order of $Re_{hp} \approx 350000$. In order to achieve higher gas velocities within the inlet header, the header pipe of the original experimental apparatus was modified by the insertion of a PVC sheet as shown in figure 4.13. As the inserted PVC sheet blanks off half of the header pipe cross-flow area, the average gas velocity within the header pipe of the dephlegmator test section is increased. The increased gas velocity yields a header pipe Reynolds number in the order of $Re_{hp} \approx 650000$, thus representing the operating conditions experienced in dephlegmator tube bundle 1 as shown in figure 2.6.

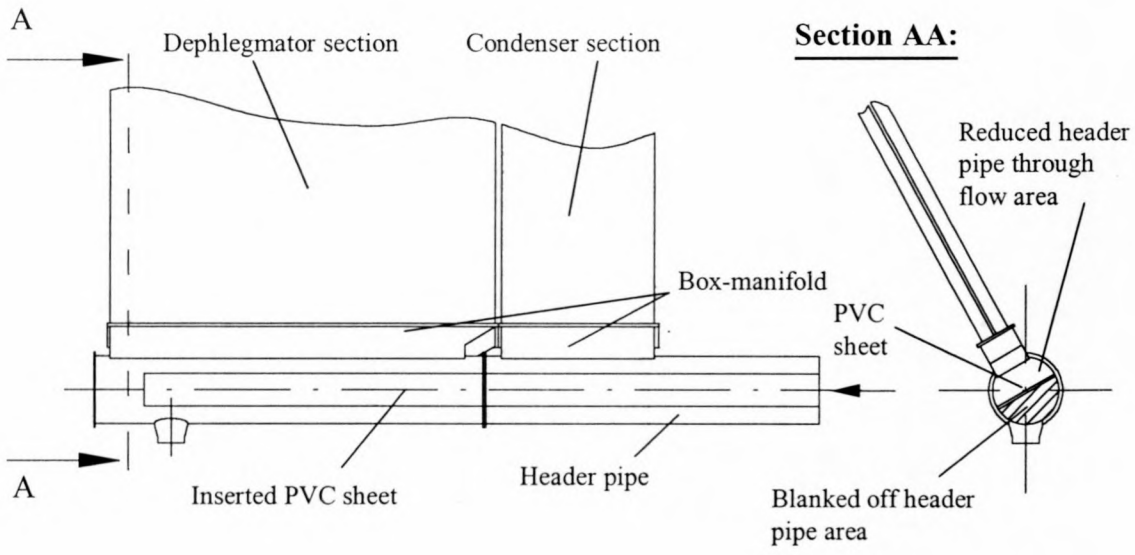

Figure 4.13: Test section with the inserted PVC sheet required for the simulation of flow conditions with $Re_{hp} \approx 650000$.

The visualised flow patterns within the box-manifold of the modified header pipe with the PVC insertion, are illustrated in figure 4.14. The size of the flow separation area on the upstream side of the box-manifold is found to be in the order of $L_{dm} = 0.75$m. In comparison, a flow separation area of $L_{dm} = 0.5$ m is experienced in the test case with the original header pipe design as shown in figure 4.11.

The measured pressure differential results obtained from a test conducted with the PVC insertion are shown in figure 4.15. Figure 4.16 shows a comparison between the measured pressure differentials of the evaluated header pipe flow conditions where $Re_{hp} = 676210$ and $Re_{hp} = 358669$ respectively. Both these tests were conducted at an air mass flow through the dephlegmator test section resulting in a densimetric gas Froude number at the inlet to the bundle tubes of $Fr_{Hsg} \approx 0.2$, as calculated by means of equation (2.1).

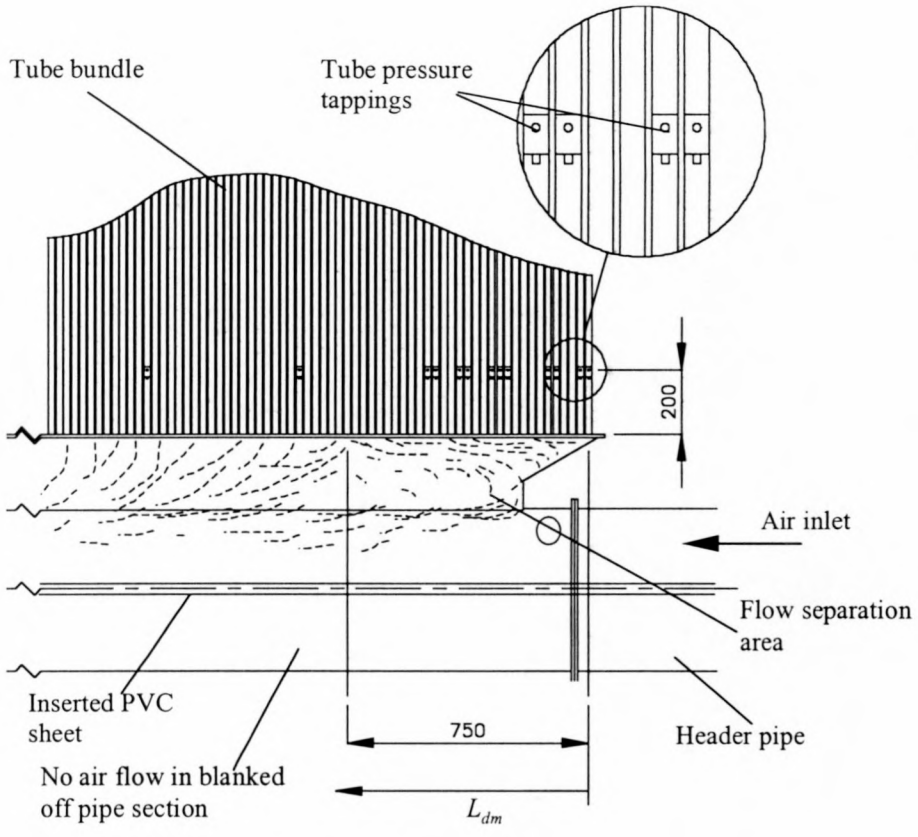

Figure 4.14: Liquid flow visualisation for a test case with the PVC sheet inserted into the header pipe.

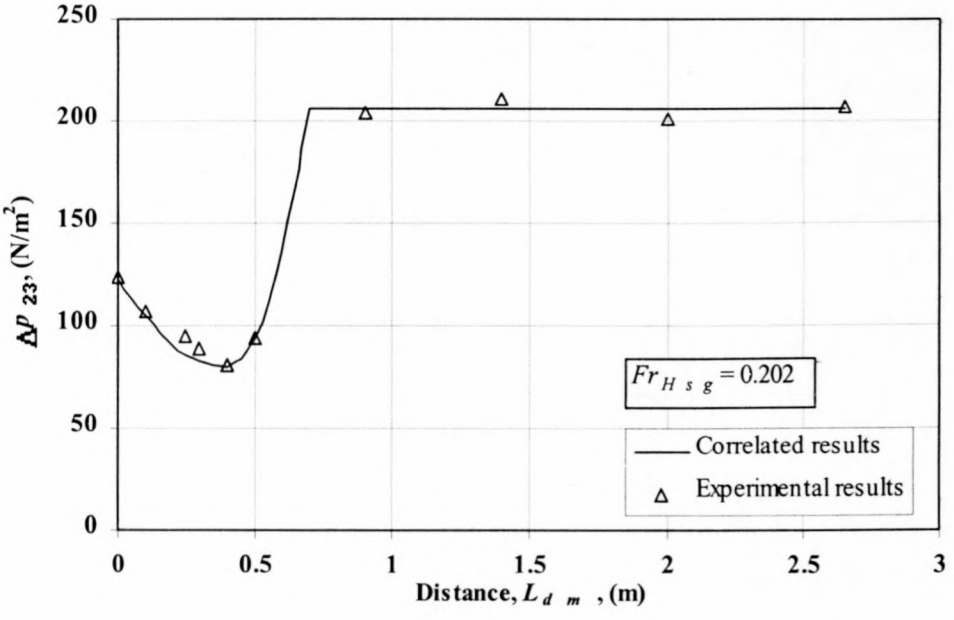

Figure 4.15: Measured pressure differential results obtained with the PVC insertion resulting in a densimetric header pipe gas Froude number, $Fr_{dsg} = 0.094$.

The evaluated operating conditions of $Re_{hp} = 676210$ and $Re_{hp} = 358669$ are representative of the flow conditions experienced in the steam dephlegmator tube bundles 1 and 2 as illustrated in figure 2.6.

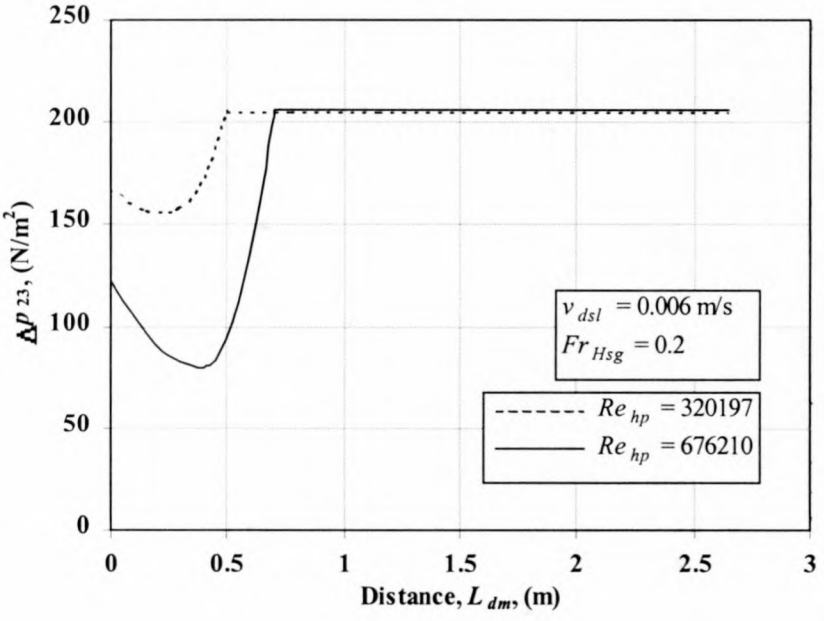

Figure 4.16: Comparison between the measured pressure differentials at different average header pipe gas velocities.

As shown, the box-manifold design results in a larger inlet pressure drop to the upstream bundle tubes. Due to the common top- and bottom headers shared by the finned tube bundles of this dephlegmator design, the larger inlet tube pressure drop may result in the formation of low pressure regions at the top of the upstream bundle tubes. This may lead to steam back-flow and the accumulation of non-condensable gases within the affected bundle tubes, to form a so-called dead zone. The formation of such a dead zone renders part of the finned tube unavailable for heat transfer and reduces its capability to transfer heat and condense steam effectively. However, the investigation shows that the flow distortions inside the box-manifold only affect a small number of tubes and therefore does not significantly affect the overall performance of the reflux condenser.

The influence of the header pipe gas velocity on the flow distribution within the header pipe is presented in terms of the header pipe, loss coefficient, K_{h2}, as given by equation (4.4). This loss coefficient represents the pressure drop between the static

pressure at the inlet to the header pipe and the static pressure within the bundle tubes, at a distance of 200 mm above the inlet to the tubes.

Figure 4.17 shows the header pipe loss coefficient results for the evaluated test cases. The operating conditions that were simulated are representative of the dephlegmator tube bundles 1 and 2, as shown in figure 2.6 where $Fr_{hsg} \approx 0.2$. The header pipe loss coefficient results are presented in terms of the downstream manifold distance, L_{dm}, to illustrate the influence of the box-manifold design on the header losses.

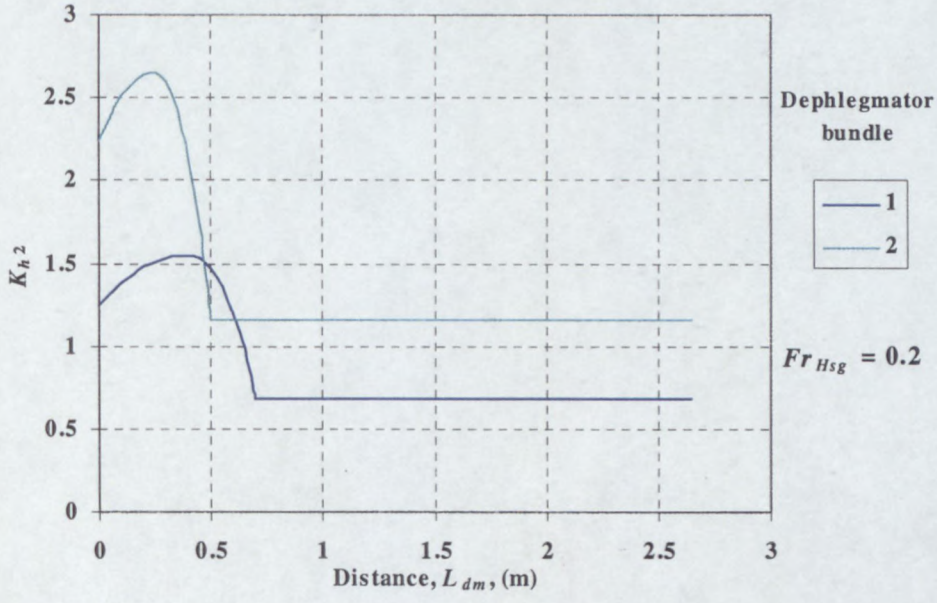

Figure 4.17: Header pipe loss coefficient in terms of the downstream manifold distance, L_{dm}.

4.4.3 *The influence of the dephlegmator box-manifold geometry on the entrance effects to the bundle tubes*

In order to investigate the influence of the upstream box-manifold geometry on the inlet loss coefficient to the dephlegmator bundle tubes, the experimental apparatus was modified by turning the upstream side of the manifold around, as shown in figure 4.18. The modified upstream section of the box-manifold, enabled the simulation of the flow conditions experienced in the box-manifolds and header pipes of dephlegmator tube bundles 3 and 4 as shown in figure 2.6. Tests were conducted with and without the PVC inserted sheet, in order to simulate the relevant manifold flow conditions. The

header pipe Reynolds number, Re_{hp}, for each of these evaluated test cases is calculated by means of equation (4.5), and found to be $Re_{hp} = 334916$ and $Re_{hp} = 636974$ respectively.

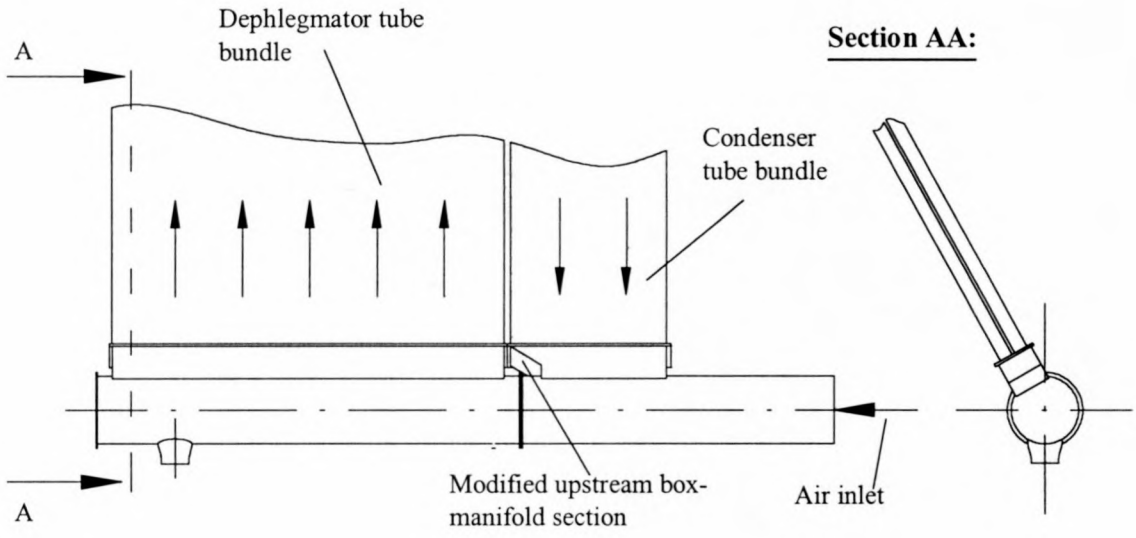

Figure 4.18: Modified experimental apparatus used to investigate the entrance effects of the flow distribution within the box-manifold on the dephlegmator bundle tubes.

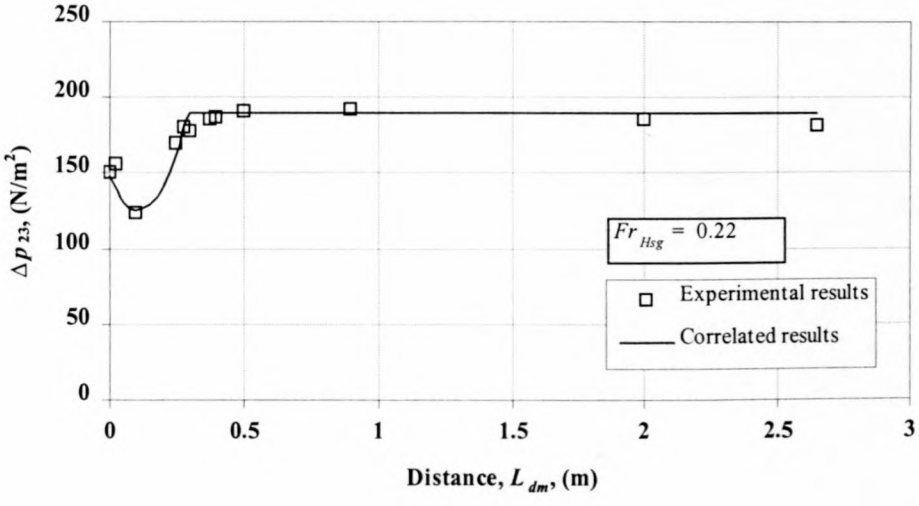

Figure 4.19: Tube pressure differential results for $Re_{hp} = 334916$.

Figures 4.19 and 4.20 show the respective tube pressure differential results. Both these tests were conducted at an air mass flow rate through the dephlegmator test section resulting in a densimetric gas Froude number at the inlet to the bundle tubes of, $Fr_{Hsg} = 0.2$, as calculated by means of equation (2.1).

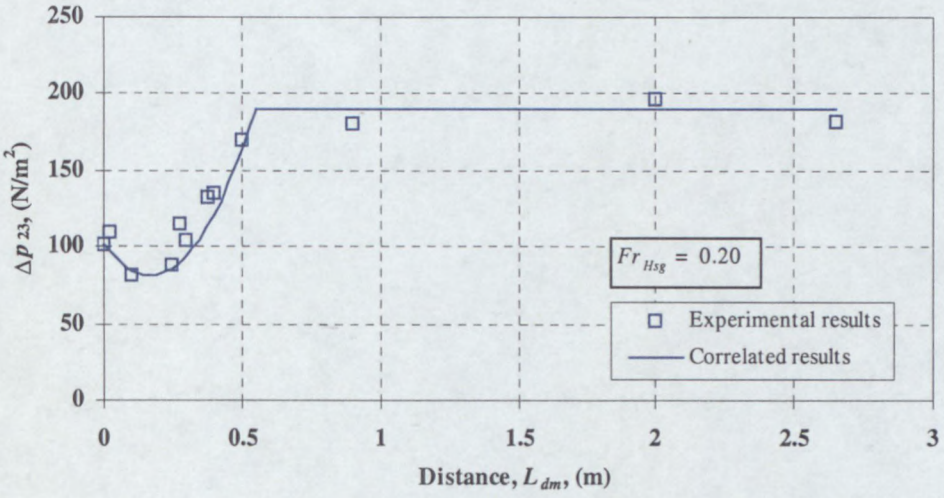

Figure 4.20: Tube pressure differential results for $Re_{hp} = 636974$.

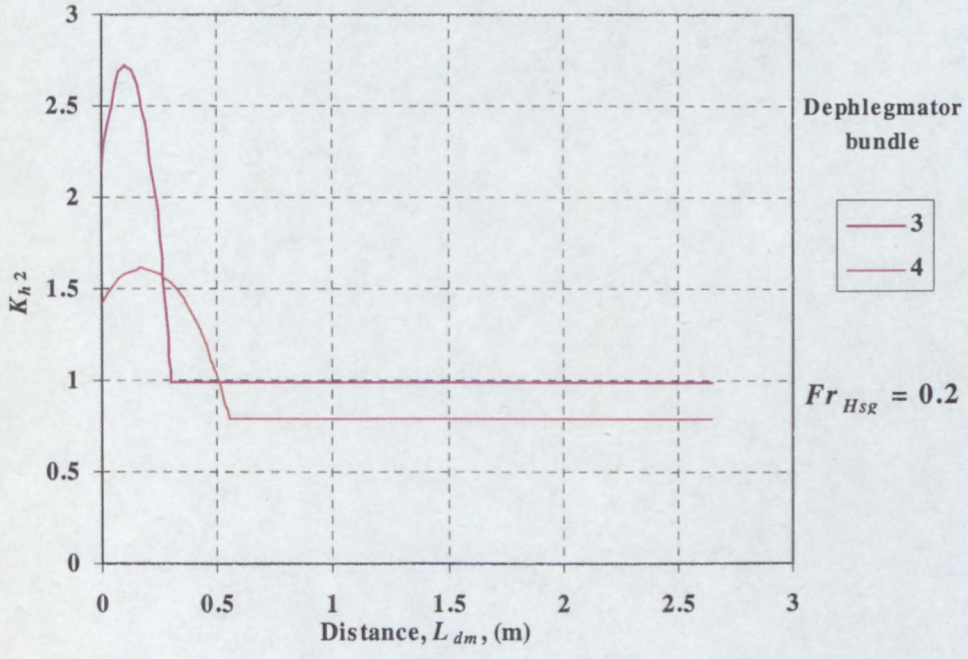

Figure 4.21: Inlet header loss coefficient results representing the operating conditions experienced in the inlet headers of bundles 3 and 4 as illustrated in figure 2.6.

The header pipe pressure loss coefficient results for the modified experimental apparatus, are presented in figure 4.21, where K_{h2} is determined by means of equation (4.4). The evaluated operating conditions of Re_{hp} = 636974 and Re_{hp} = 334916 are representative of the flow conditions experienced in inlet headers of dephlegmator tube bundles 3 and 4, as illustrated in figure 2.6.

4.4.5 Summary of the experimental results

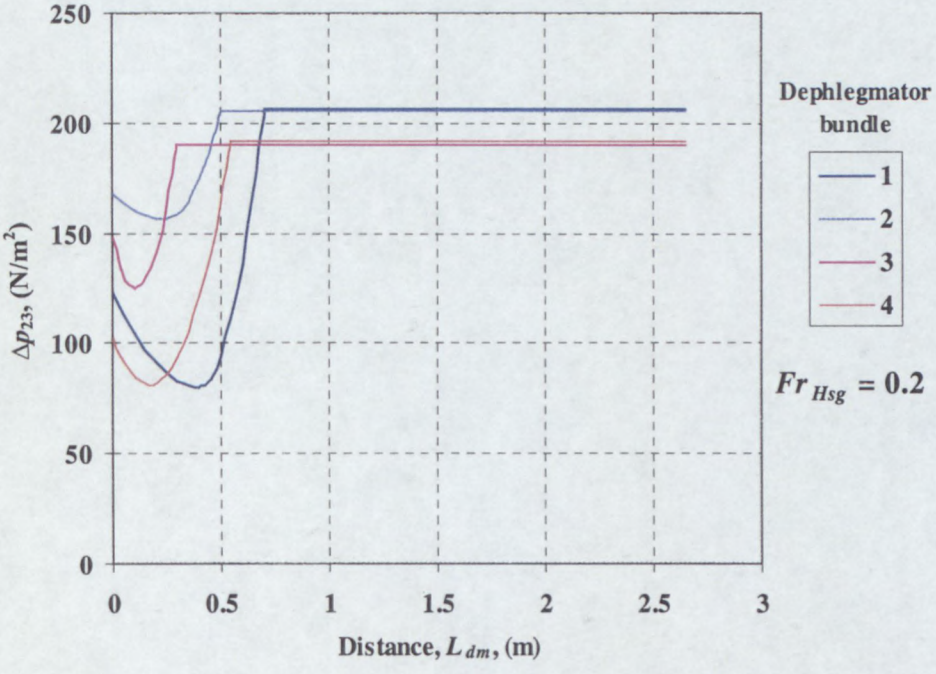

Figure 4.22: Summary of the measured tube pressure differentials, Δp_{23}, in terms of L_{dm}.

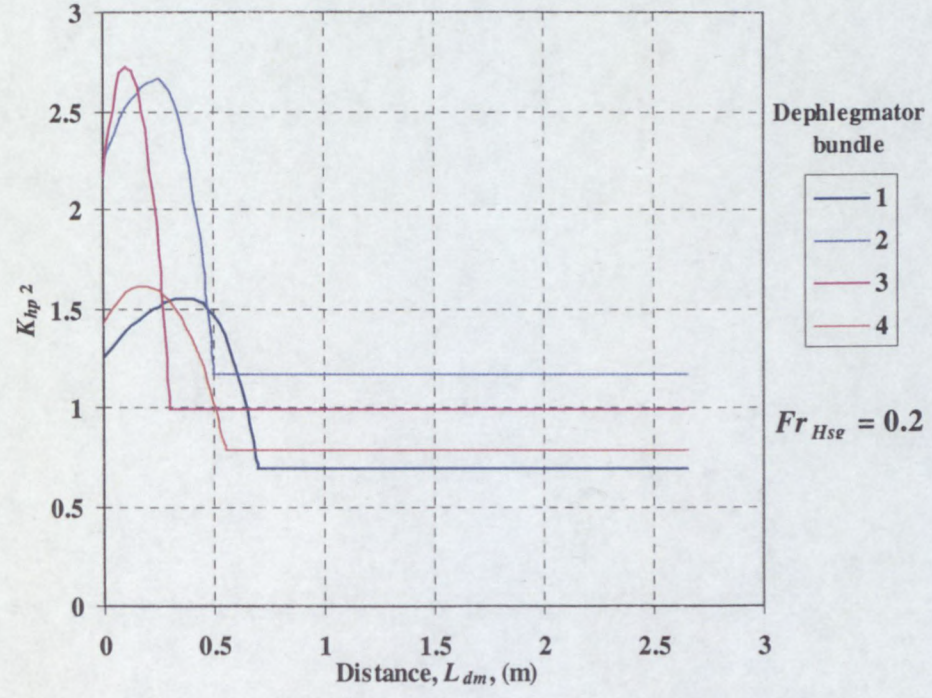

Figure 4.23: Summary of the inlet header loss coefficient, K_{h2}, results in terms of L_{dm}.

4.4.4 Liquid entrainment

Liquid entrainment was noted at the inlet to the bundle tubes situated in the upstream side of the box-manifold due to the flow distortions encountered in this region. Because of the short tube lengths of the experimental apparatus, the entrained liquid was ejected along with the air at the outlet of the bundle tubes and no accumulation of liquid within the bundle tubes was noted.

4.4.5 Summary of the experimental results

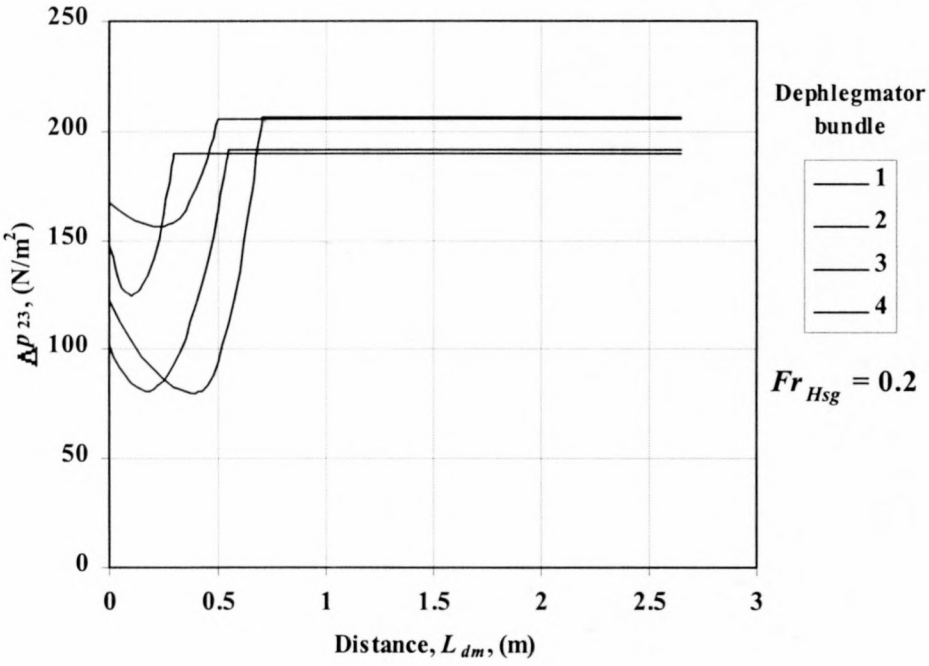

Figure 4.22: Summary of the measured tube pressure differentials, Δp_{23}, in terms of L_{dm}.

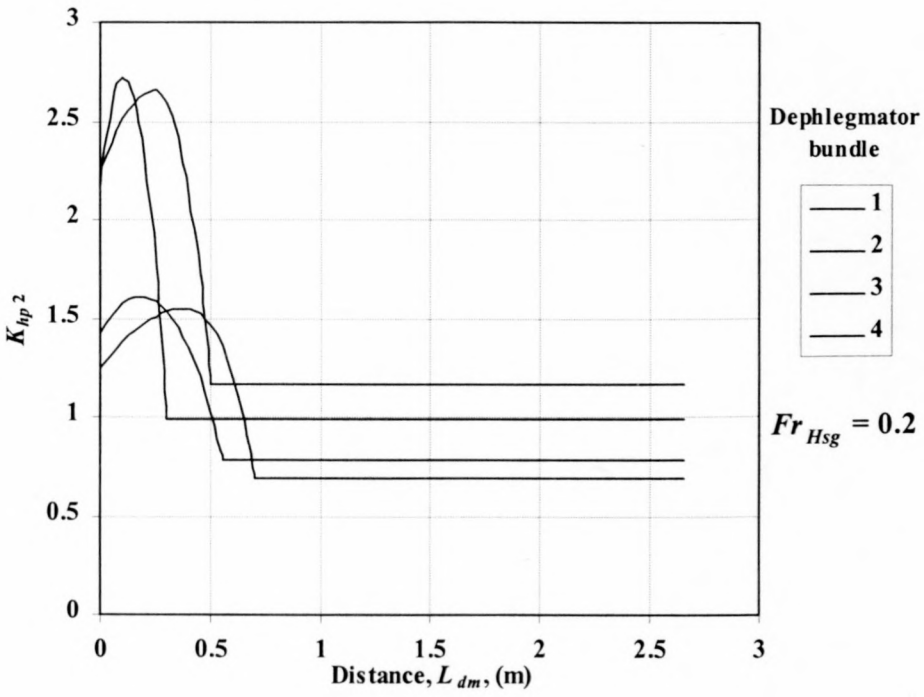

Figure 4.23: Summary of the inlet header loss coefficient, K_{h2}, results in terms of L_{dm}.

4.5 Conclusion on the evaluated box-type inlet manifold design

The simple box-type manifold design ensures easy manufacturing, handling and assembly of the tube bundles. The number of welding joints incorporated in this design is fewer than those used in the D-type inlet manifold design and thus limits potential leaks into the system. Furthermore, less material is required in the manufacture of the box-type manifold design, and this translates to a smaller dephlegmator mass compared to dephlegmators of the D-type manifold design.

The tube pressure differential and header loss coefficient results, as presented in figures 4.22 and 4.23, show that only a small number of the dephlegmator bundle tubes are affected by the box-type inlet manifold design. Only tubes situated in the upstream side of the box-manifold are affected by the flow separation encountered within the manifold and it proves to be an efficient and useful design.

CHAPTER 5

PROPOSED DEPHLEGMATOR DESIGN

5.1 Introduction

In view of the limitations that current A-configuration ACC designs pose to effective dephlegmator operation, a new ACC design is proposed as shown in figure 5.1. Each fan unit of the proposed ACC design consists of eight A-configuration primary condenser tube bundles, and two essentially horizontal dephlegmator tube bundles. This design aims to resolve the limitations of existing dephlegmators, which result from either poor inlet manifold design or counter-current flow conditions.

In this chapter it will be shown experimentally that the proposed, horizontal dephlegmator finned tubes encounter co-current steam and condensate flow and that no liquid or non-condensable gases are accumulated under these operating conditions. Thus, the formation of dead zones in the dephlegmator tube bundles is eliminated, providing more effective heat transfer.

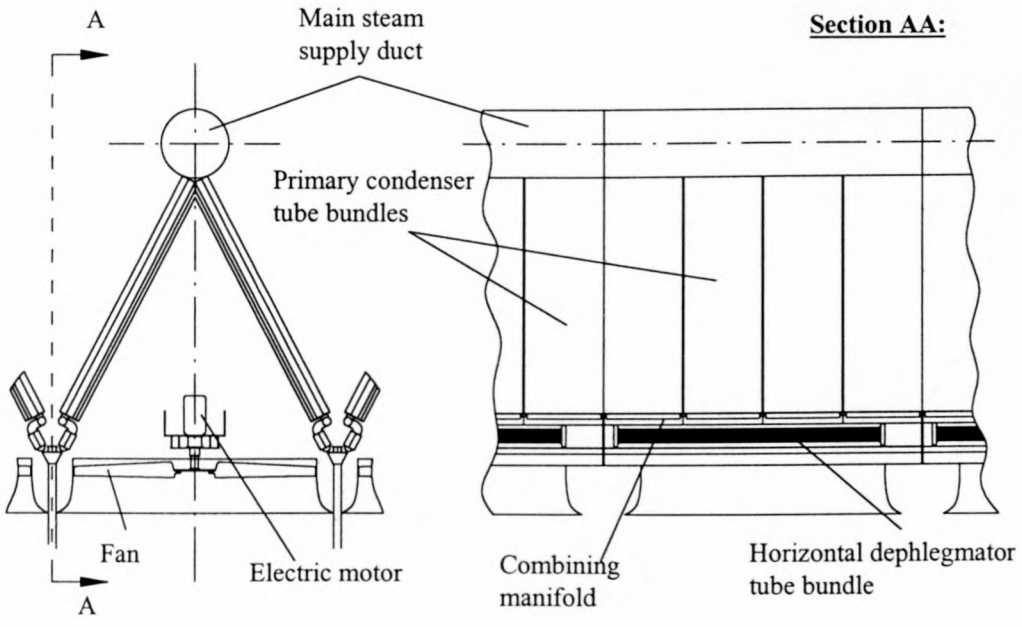

Figure 5.1: Schematic of a fan unit illustrating the proposed dephlegmator design.

5.2 *Performance evaluation of a finned tube operating at small inclination angles*

The performance characteristics, i.e. the heat transfer coefficient and the pressure drop of the proposed, essentially horizontal dephlegmator tubes, are verified with the aid of the single tube, experimental apparatus shown in figure 5.2. Steam at sub-atmospheric pressure, representative of the operating conditions in a steam power plant's ACC system, is condensed in the air-cooled test tube. The operating conditions that are investigated range for inclination angles of -5° to 4° and an inlet vapour temperature of T_{vi} = 60°C or 50°C. During a typical test run, the heat transfer and steam-side tube pressure drop characteristics are measured and the experimental results are compared to predicted values.

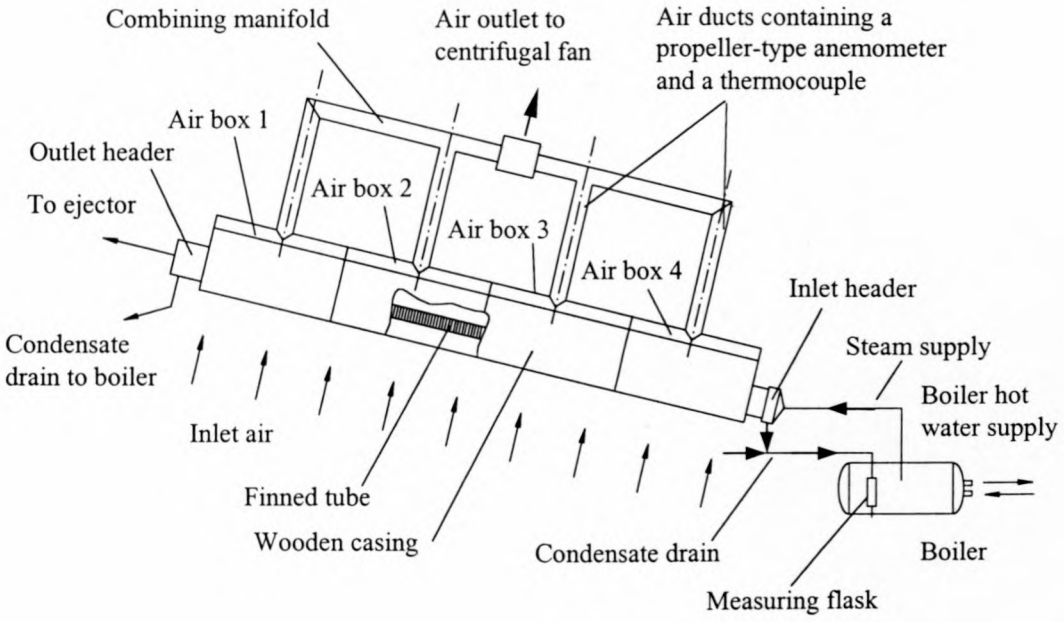

Figure 5.2: Schematics of the experimental apparatus.

5.2.1 *Experimental apparatus*

The experimental apparatus consists of a finned tube, enclosed inside a wooden casing as shown in figure 5.2. The finned tube employed in the experimental apparatus is of similar design to tubes used regularly in the design of steam power plant ACC units. Figure B.1 shows a detailed drawing of the test tube cross-section and all the relevant

tube dimensions are determined in Appendix B. The test tube is 6.982 m in legth, with an inside tube height and width of 97 mm and 16 mm respectively.

A radial fan supplies the airflow across the finned tube via a ducting system, by drawing air from the surroundings through the bell-mouth inlet into the wooden casing. After crossing the finned tube, the air flows via four air boxes into four equally spaced ducts. Each of these ducts contains a propeller-type anemometer which measures the air mass flow rate through respective air boxes. The summation of the air flow in each air box yields the total measured air flow through the experimental apparatus. To ensure accurate flow measurements in the air ducts, each anemometer was calibrated in a windtunnel prior to installation. Furthermore, a variable speed control system is used to adjust the centrifugal fan speed and subsequent air mass flow through the apparatus.

Six thermocouples, equally spaced along the bell-mouth inlet to the experimental apparatus, measure the air inlet temperature, while the air outlet temperature is measured by twelve equally spaced thermocouples situated in the air boxes located above the test tube. Two thermocouples measure the average air temperature in each of the four air ducts in order to determine the air-properties required for the calculations.

A water heated, shell-and-tube boiler is used to generate steam at sub-atmospheric conditions with a saturation temperature of 50°C or 60°C, depending on the requirements for a particular test. Hot water is circulated through the boiler by means of a centrifugal water pump. A flexible steel pipe connects the boiler to the radial test tube inlet header thereby ensuring that the steam entering the tube is vortex free. Condensate is returned from the tube headers via an insulated tube to a measuring flask, which is used, together with a stopwatch to determine the condensate mass flow during a test run. The in- and outlet steam temperatures at the respective test tube headers are measured by copper-constantan thermocouples and a low-range *Foxboro 823DP* differential pressure transducer measures the pressure differential across the tube inlet- and outlet headers. The pressure transducer was calibrated and the output of the transducer was verified as being linear.

During a typical test run, the air flow rate and the power input to the electrically heated boiler water are adjusted until the system stabilises at a predetermined steam inlet

temperature to the finned tube. Once equilibrium conditions have been attained, the applicable air and steam temperatures, pressure drop, air flow rate and condensation rates are recorded. The air flow rate is thereafter increased to a new value and the routine is repeated. With this procedure, the heat transfer characteristics of the test tube are determined and a pressure drop curve is generated as a function of the vapour flow rate entering the finned tube for a specific operating steam temperature and tube inclination angle.

5.2.2 Heat transfer and pressure drop prediction

The Zapke-Kröger [97ZA1] pressure drop model, which is presented in Appendix A, is used to predict the pressure drop across the test tube for situations where no flooding occurs. The heat transfer of the finned tube is predicted by solving a set of heat transfer equations. Appendix D gives a sample calculation that shows the relevant calculations for a chosen experimental data set.

Pressure drop prediction:

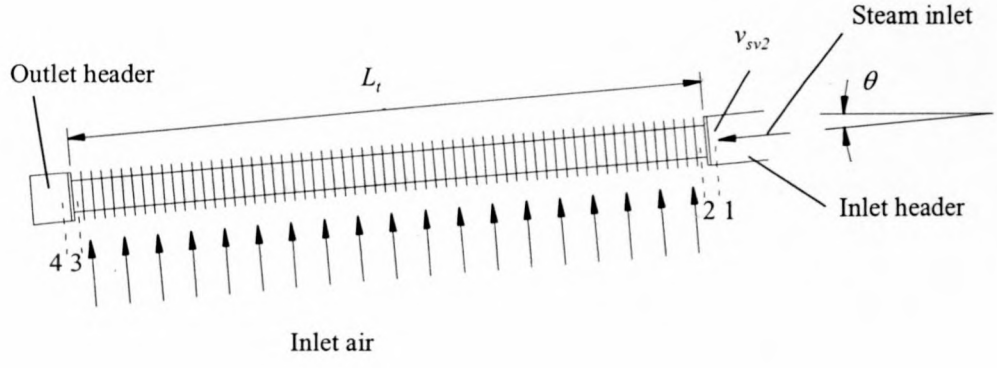

Figure 5.3: Schematics of the test tube.

Figure 5.3 shows the schematic of the test tube at an angle of θ to the horizontal. The total pressure drop across the headers of the finned tube consists of an inlet pressure loss, Δp_{12}, a pressure loss inside the test tube, Δp_{23}, and an outlet pressure loss, Δp_{34}, as given by the following equation:

$$\Delta p_{14} = \Delta p_{12} + \Delta p_{23} + \Delta p_{34} \tag{5.1}$$

For negative tube inclination angles to the horizontal, there is no condensate drainage at the inlet to the test tube and all condensate drains to the outlet header, from where it is fed back to the boiler via the measuring flask. In the absence of condensate drainage at the tube inlet, the inlet pressure drop can be expressed in terms of a single-phase incompressible contraction loss coefficient, K_{csp}. Kröger [98KR1] gives the following equation for the calculation of the static inlet pressure drop, Δp_{12}, due to a sudden contraction in flow area.

$$\Delta p_{12} = p_1 - p_2 = \tfrac{1}{2}\rho v_2^2\left(1 - \sigma_{21}^2 + K_{csp}\right) \tag{5.2}$$

where $\sigma_{21} = A_2/A_1$. A_1 and A_2 are the inlet header- and tube cross-sectional flow areas respectively. The irreversible losses are contained in the contraction coefficient K_{csp}, which can be expressed by the following equation for highly turbulent flow.

$$K_{csp} = 1 - \frac{2}{\sigma_c} + \frac{1}{\sigma_c^2} = \left(1 - \frac{1}{\sigma_c}\right)^2 \tag{5.3}$$

σ_c is given by the following empirical relation presented by Rouse [46RO1] for flow entering parallel plates.

$$\sigma_c = 0.6144517 + 0.04566493\sigma_{21} - 0.336651\sigma_{21}^2 + 0.4082743\sigma_{21}^3 + 2.672041\sigma_{21}^4 - 5.963169\sigma_{21}^5 + 3.558944\sigma_{21}^6 \tag{5.4}$$

In the case of positive tube inclination angles to the horizontal, condensate drainage occurs at the inlet to the test tube. Zapke [97ZA1] derived the following expression for the tube inlet pressure drop, Δp_{12}, in the presence of draining liquid:

$$\Delta p_{12} = \tfrac{1}{2}\rho_v v_{sv2}^2\left(K_{tp} - \sigma_{21}^2\right) \tag{5.5}$$

K_{tp}, is a two-phase loss coefficient and a function of the densimetric gas Froude number, Fr_{Hsg}, as given by equation (A.32). Equation (5.5) is valid for steady counter-flow conditions and does not incorporate the strong increase and unsteady nature of the pressure drop associated with the flooding of finned tubes.

The pressure drop inside the test tube, Δp_{23}, is the sum of a frictional, gravitational and momentum component as given by equation (A.33).

$$\Delta p_{23} = \Delta p_{23f} + \Delta p_{23g} + \Delta p_{23m}$$

$$= \int_0^{L_t} \beta \left(\frac{dp}{dz} \right)_{ftp} dz + \int_0^{L_t} g \rho_v \sin(\theta_t) + \int_0^{L_t} -\frac{d}{dz}\left(\rho_v v_{sv}^2\right) dz \qquad (5.6)$$

The following linear relation approximates the variation in the vapour velocity along the axial direction of the finned tube.

$$v_{sv} = \left(v_{sv3} - v_{sv2}\right) z / L_t + v_{sv2} \qquad (5.7)$$

Substitute equations (A.34) to (A.38) and (5.7) in equation (5.6) and integrate to obtain the following equation governing the pressure drop inside the test tube.

$$\Delta p_{23} = \frac{1}{2} \rho_v v_{sv2}^2 \left[\frac{L_t}{d_e} \frac{K\, Re_{sv2}^n}{\left(1 - v_{sv3} / v_{sv2}\right)} \left(\frac{a_1 \left(1 - \left(v_{sv3} / v_{sv2}\right)^{n+3}\right)}{n+3} \right.\right.$$

$$\left.\left. + \frac{a_2 \left(1 - \left(v_{sv3} / v_{sv2}\right)^{n+2}\right)}{(n+2) Re_{sv2}} \right] + \rho_v g L_t \sin(\theta_t) - \left(\rho_v v_{sv2}^2 - \rho_v v_{sv3}^2\right) \qquad (5.8)$$

Assuming that all the steam is condensed inside the finned tube section, the outlet vapour velocity, $v_{sv3} = 0$. Upon substitution of the zero outlet vapour velocity condition into equation (5.8) the pressure loss inside the test tube is as follows:

$$\Delta p_{23} = \frac{1}{2} \rho_v v_{sv}^2 \left[\frac{L_t}{d_e} K\, Re_{sv2}^n \left(\frac{a_1}{n+3} + \frac{a_2}{(n+2) Re_{sv2}} \right) \right] + \rho_v g L_t \sin(\theta_t) - \rho_v v_{sv2}^2 \qquad (5.9)$$

The pressure drop at the outlet to the test tube, Δp_{34}, where the vapour exits the tube is calculated with the aid of an expansion loss coefficient for single-phase flow between parallel plates [98KR1].

$$\Delta p_{34} = \tfrac{1}{2}\rho_v v_{sv3}^2 \left[K_{esp} - \left(1 - \sigma_{34}^2\right)\right] \tag{5.10}$$

K_{esp} is the expansion loss coefficient, and $\sigma_{34} = A_3/A_4$. In this instance, A_3 is the tube cross-sectional flow area and A_4 the effective cross-sectional outlet header area. Kays [50KA1] gives the following expression for the calculation of the expansion loss coefficient for highly turbulent flow.

$$K_{esp} = \left(1 - \sigma_{34}\right)^2 \tag{5.11}$$

From equation (5.10) it is clear that the outlet pressure drop will be zero in the absence of vapour outflow at the outlet of the finned tube. Substituting either equation (5.2) or (5.5) depending on the phase conditions at the test tube inlet, and equations (5.8) and (5.10) into equation (5.1) gives the predicted pressure drop across the test tube.

The governing dimensionless group for the evaluation of the test tube pressure loss is the densimetric vapour Froude number, Fr_{Hsg}, at the inlet to the test tube.

$$Fr_{Hsg} = \frac{\rho_v v_{sv}^2}{\left[gH_t\left(\rho_l - \rho_v\right)\right]} \tag{5.12}$$

Appendix D gives a sample calculation illustrating the relevant calculations in order to predict the tube pressure drop for a given operating condition.

For positive inclination angles, the predicted densimetric gas Froude number at which tube flooding will occur is calculated by means of equation (A.53).

$$Fr_{Hsg} = K_o \exp\left(-nFr_{dsl}^{0.6} / Zk_d^{0.2}\right) \tag{5.13}$$

Heat transfer prediction:

The heat transfer from the condensing steam to the air passing across the test tube according to equation (A.14) is given as

$$Q_a = m_a c_{pam}(T_{ao} - T_{ai}) = m_a c_{pam}(T_{vm} - T_{ai})e \tag{5.14}$$

where e is the effectiveness of the test tube, which is given by equation (A.15). Appendix D gives a sample calculation that illustrates the relevant calculations whereby the heat transfer of the test tube is predicted. The experimental results of the evaluated operating conditions are presented in tables D.1 to D.10

5.2.3 *Discussion of the experimental results*

The tube pressure drop results obtained from the conducted investigation are presented in figures 5.4 and 5.5. Tests conducted at positive inclination angles show a sudden increase in the measured test tube pressure drop, Δp_{14}, at a densimetric vapour Froude number in the order of $0.084 < Fr_{Hsv2} < 0.1$, depending on the tube inclination angle. This sudden increase in the pressure drop is caused by the accumulation of condensate within the test tube and is associated with the flooding phenomenon. Equation (5.13) accurately predicts the onset of flooding for positive inclination angles of $\theta \geq 2^{\circ}$ as indicated in the figures. Apart from the sudden increase in the tube pressure drop, it is also noted that at the onset of flooding, the pressure measurements are of a pulsating nature.

At inclination angles of 1° and 2° degrees, the inlet vapour velocity associated with the onset of flooding is sufficient to force the condensate into the outlet header of the test tube. As flooding occurs, the amount of condensate draining at the inlet header of the test tube decreases with an increase in the inlet vapour velocity, until the vapour velocity is sufficient to force all the condensate to drain through the outlet header. This phenomenon explains the trend of the experimentally measured tube pressure drop results for these inclination angles.

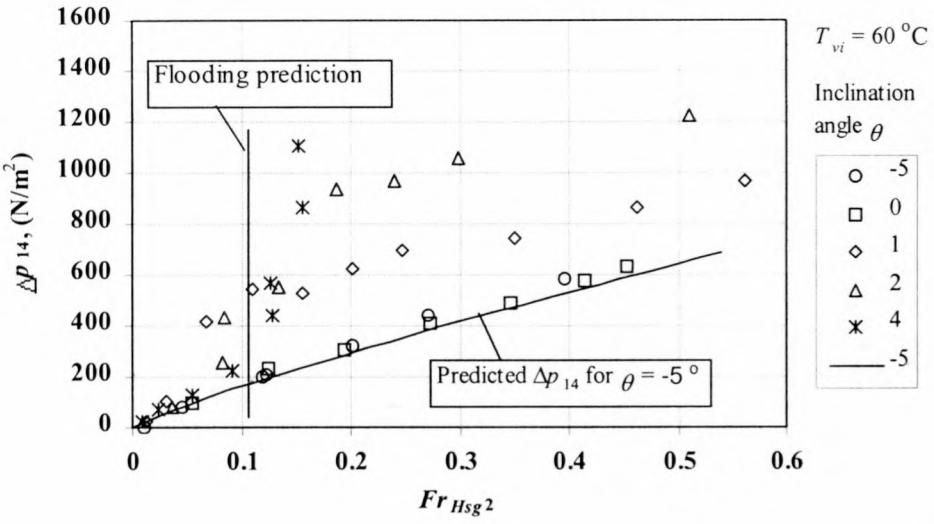

Figure 5.4: Comparison between experimental and predicted tube pressure drop for a vapour inlet temperature to the test tube of T_{vi} = 60 °C.

At an inclination angle of 4°, the inlet vapour velocity is insufficient to force the condensate to drain through the outlet header. This causes the accumulation of condensate in the test tube, which gives rise to the sudden increase in the measured tube pressure drop at the onset of flooding.

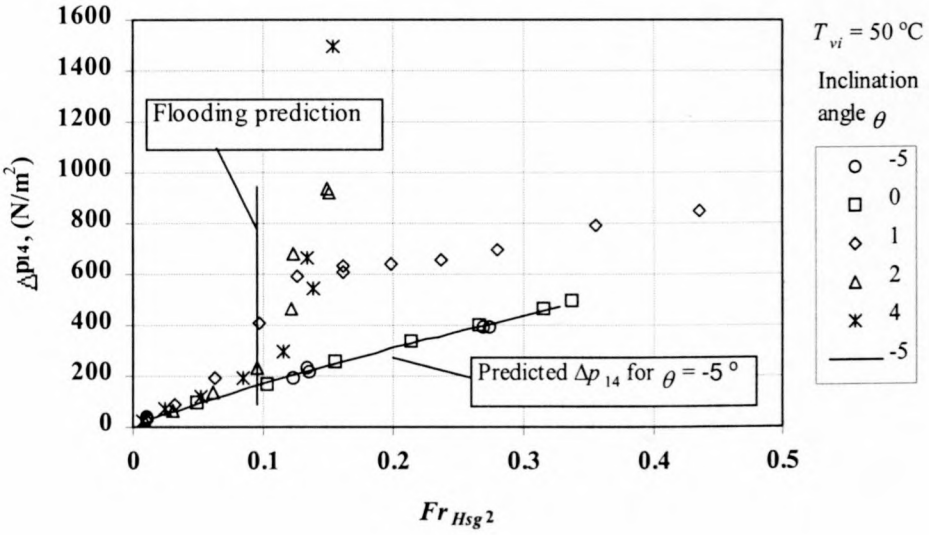

Figure 5.5: Comparison between experimental and predicted tube pressure drop for a vapour inlet temperature to the test tube of T_{vi} = 50 °C.

For negative tube inclination angles, the measured pressure drop compares well with the predicted values, no flooding is noted and all the condensate drains through the outlet

header. This proves that the proposed dephlegmator design incorporating the use of tube bundles inclined at 0° to –5° to the horizontal, will eliminate the accumulation of condensate and flooding of the dephlegmator bundle tubes.

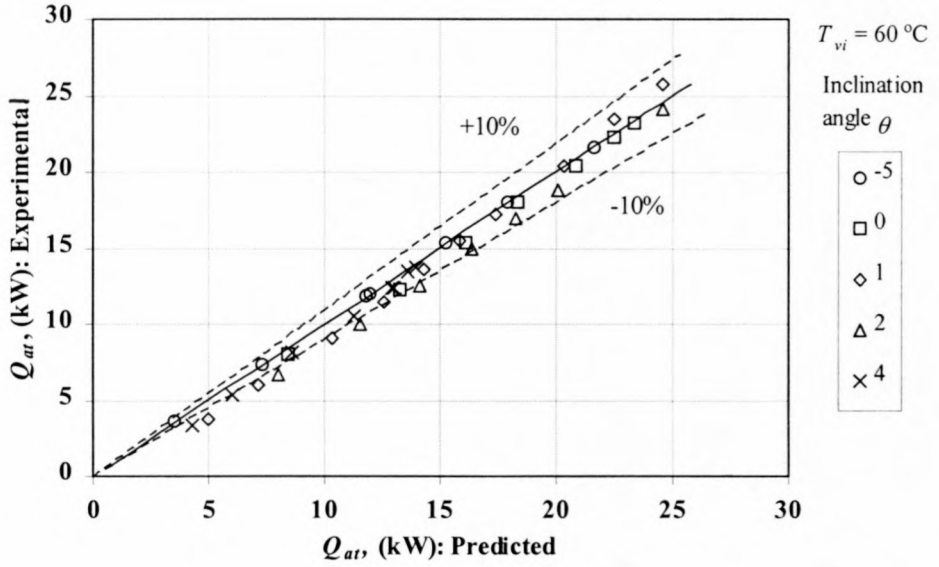

Figure 5.6: Comparison between the experimental and predicted heat transfer rate for an inlet vapour temperature of T_{vi} = 60 °C.

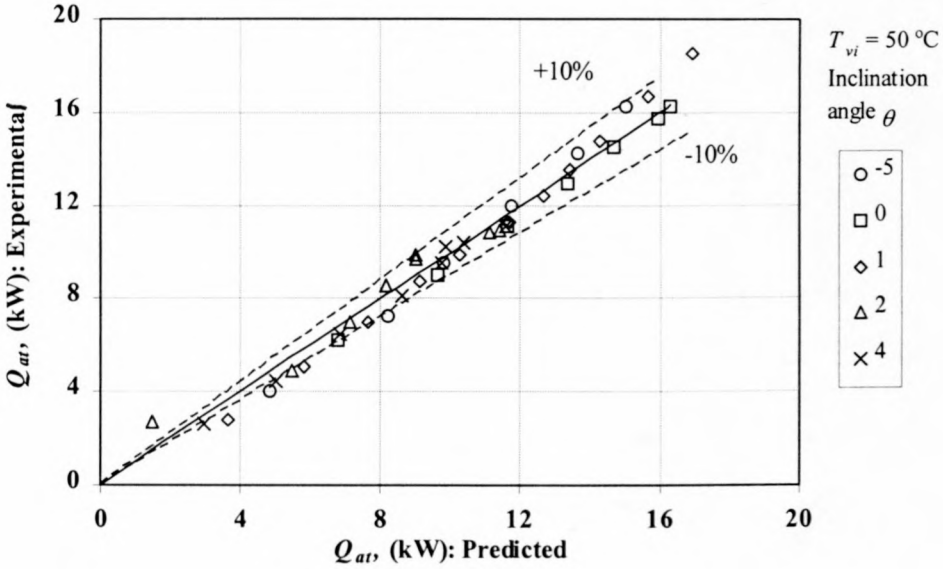

Figure 5.7: Comparison between the experimental and predicted heat transfer rate for an inlet vapour temperature of T_{vi} = 50 °C.

The comparison between the experimental and predicted heat transfer results of the investigation are presented in figures 5.6 and 5.7. As shown in these figures, the predicted results compare well with the experimental results.

No difference in the heat transfer capability is noted at the investigated tube inclination angles. It can thus be stated that the finned tube heat transfer is a function of the temperature difference between the saturated steam temperature inside the tube and the ambient air temperature and that the tube inclination angle does not influence the heat transfer characteristics for small inclination angles.

5.3 Pressure distribution within the steam supply duct and combining manifold of an A-configuration condenser system

The main steam supply duct and combining manifold, as shown in figure 5.1, facilitate the steam supply through the condenser bundle tubes of an A-configuration forced draught ACC system. Figure 5.8 shows two possible manifold configurations, i.e. a U- or Z-type configuration, for this particular ACC design.

According to Zipfel [96ZI1], the pressure in the main steam duct and combining manifold of a condenser unit varies due to frictional effects and changes in momentum. The pressure due to frictional effects always decreases in the flow direction while the change in momentum causes an increase in pressure in the flow direction. In most manifold systems, the frictional effects are significantly smaller than the effects due to the change in momentum. It can therefore be expected that the pressure in the main steam duct will increase in the flow direction while the pressure in the combining manifold will decrease in the flow direction. Due to the pressure distribution within the respective steam duct and combining manifold, a U-configuration manifold system is selected for the proposed dephlegmator design.

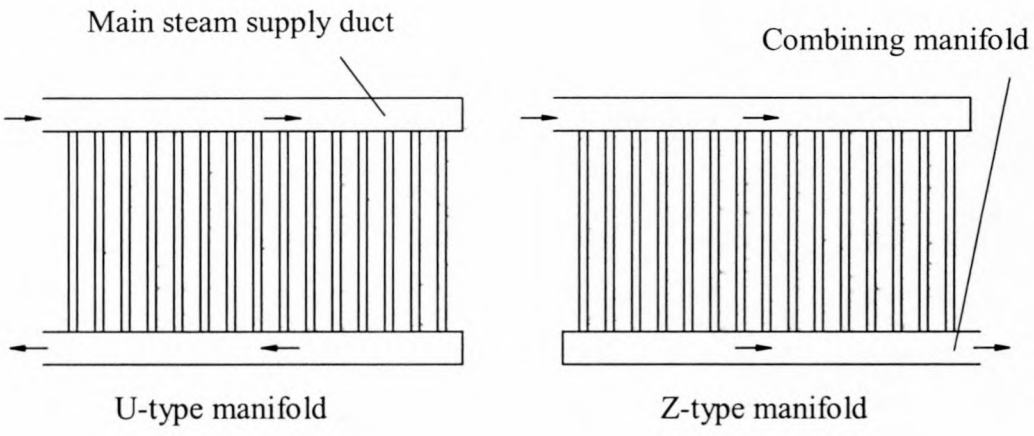

Figure 5.8: Condenser manifold configurations.

5.4 *Proposed ACC design*

Figures 5.1 and 5.9 show the schematics of a fan unit, illustrating the proposed ACC design. Each ACC fan unit consists of eight double row condenser tube bundles arranged in the U-type manifold configuration and two essentially horizontal, double row dephlegmators. The heat transfer characteristics of the condenser and dephlegmator tube rows should be matched at design air and steam temperatures, representing the average annual operating conditions. This will ensure matched heat transfer rates of the respective condenser and dephlegmator tube rows and ensure that backflow and tube row effects be minimised. Appendix C illustrates the tube row heat transfer matching of a particular double row ACC.

The tests conducted on the experimental fin tube show that flooding does not occur for operation angles of $\theta \leq 0$. The proposed dephlegmator design shown in the relevant figures therefore incorporates finned tube bundles with an inclination angle of $\theta = 0$ to eliminate any flooding phenomenon.

Turbine exhaust steam is fed to the top of the condenser tube bundles by means of the main steam supply duct, where it is partially condensed. Co-current flow conditions are encountered inside the condenser finned tube bundles as the condensate drains, by

means of gravity, downward to the combining manifold from where it is pumped back to the water reservoir.

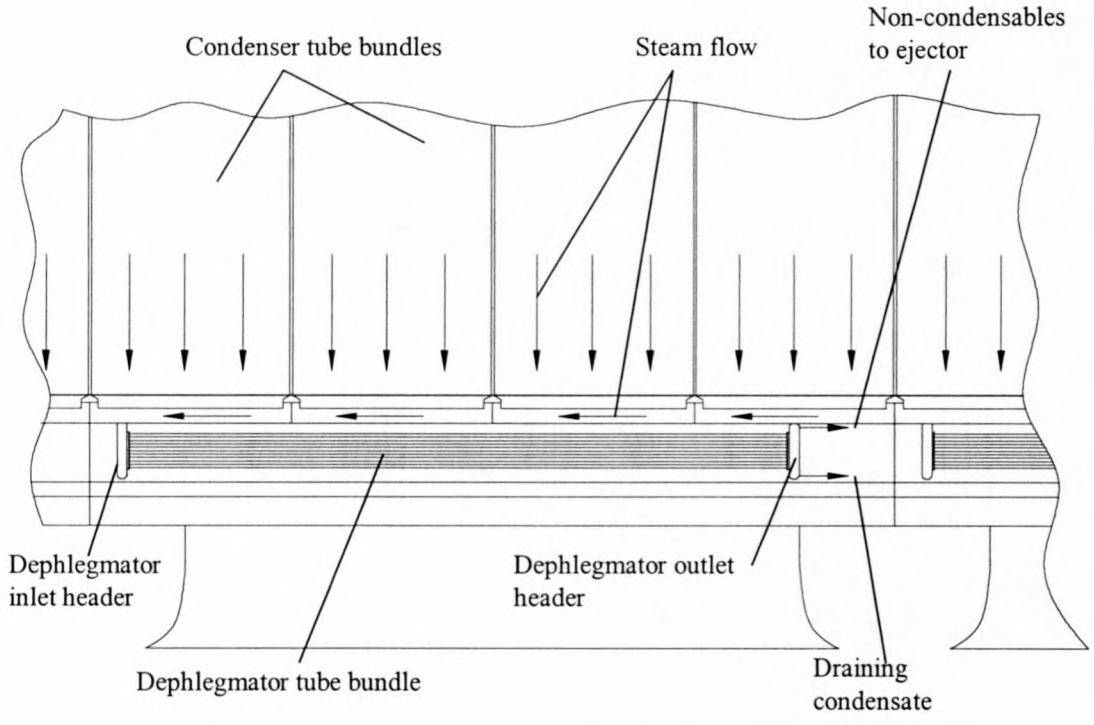

Figure 5.9: Schematics of the condenser and dephlegmator tube bundles.

Excess steam that is not condensed in the condenser bundles, together with the non-condensable gases, also exits into the combining condenser manifold and flows to the respective dephlegmator units. Within the dephlegmator bundle tubes, the steam is condensed and the non-condensable gases are fed to the dephlegmator outlet headers. At the outlet headers the non-condensables accumulate to be removed by a steam driven ejector system. The condensate from the dephlegmator tube bundles is also accumulated in the outlet headers, to be pumped back to the water reservoir.

5.5 Conclusion

The proposed design eliminates the troublesome counter-flow conditions in current dephlegmator designs. This ensures that no condensate accumulates within the condenser or dephlegmator bundle tubes, which may cause an increase in the turbine backpressure of the power station. Tube row effects that may aggravate the

accumulation of non-condensables to form dead zones are also minimised by properly matching the heat transfer characteristics of the bundle tubes.

As shown in figure 1.6, current dephlegmator designs require an additional fan unit for each dephlegmator of the ACC system. The proposed design, however, incorporates the dephlegmator as integral part of the fan unit so that each fan unit consists of a set of condenser tube bundles and its own dephlegmator system. The additional fan units required for the dephlegmators in previous ACC designs are thus eliminated.

CHAPTER 6

CONCLUSIONS AND RECOMMENDATIONS

6.1 Conclusions

In this dissertation factors such as tube row effects, ejector operation, flooding of bundle tubes and inlet manifold design that limit effective dephlegmator operation are discussed. Laboratory experiments are conducted to investigate the pressure drop and flow characteristics of the D- and box-type inlet manifold in order to quantify the effect of these designs on effective dephlegmator operation.

The investigation on the D-type inlet manifold shows severe entrainment of liquid entering the top of the drain stubs even at relatively low air flow rates. As a result a significant amount of liquid is retained in the D-type manifold. As shown in figure 3.6 a sudden increase in pressure drop, Δp_{23}, occurs at a densimetric Froude number in the order of $Fr_{Hsg} \approx 0.07$ as opposed to the prediction of $0.4 < Fr_{Hsg} < 0.5$ obtained by equation (A.53) [97ZA1]. To improve the performance of dephlegmators incorporating the D-type manifold design, the latter can be modified by draining condensate from the D-manifold through down-pipes located between the drain stubs. These down-pipes ensure proper condensate drainage and eliminate entrainment within the drain stubs. Figure 3.8 shows results obtained during an investigation on a dephlegmator system with the down-pipe modification showing notable heat transfer improvement compared to an unmodified dephlegmator bundle.

Flow visualisation within the box-type inlet manifold shows flow separation at the inlet (upstream side) to the box-manifold. This results in re-circulation and a lower inlet tube pressure drop, Δp_{23}, compared to a downstream position within the manifold. Insufficient ejector capacity may lead to the backflow of steam into bundle tubes situated in the upstream side of the manifold that can result in the accumulation of non-condensable gases. The pressure differential, Δp_{23}, and header pipe loss coefficient,

K_{h2}, results presented in figures 4.22 and 4.23 respectively show that only a small number of dephlegmator bundle tubes situated on the upstream side of the box-manifold are affected by the design.

The proposed, essentially horizontal dephlegmator design eliminates troublesome counter-flow conditions encountered in current A-configuration dephlegmator designs. The experimental tube pressure drop, Δp_{14}, results shown in figure 5.4 show that no flooding or the accumulation of condensate occurs at operating conditions with zero and negative tube angles to the horizontal. Tube row effects that may aggravate the accumulation of non-condensables to form dead zones are also minimized by properly matching the heat transfer characteristics of the dephlegmator bundle tubes as shown in Appendix C.

6.2 Recommendations

Due to fan capacity limitations, only a single representative operating condition rendering a densimetric gas Froude number $Fr_{Hsg} \approx 0.2$ was simulated during the investigation conducted on the box-type inlet manifold. It is therefore recommended to modify the existing experimental apparatus to enable the investigation of further operating conditions.

The numerical analysis of fluid dynamics associated with fluid flows forms an integral part of the modern study of fluids and Computational Fluid Dynamics (CFD) contribute to our understanding of complex flow conditions. The research conducted in this study can be complemented by future CFD investigations on the flow conditions experienced in dephlegmator inlet manifold designs.

REFERENCES

33CO1 Colburn, A.P., A Method of Correlating Forced Convection Heat Transfer Data and a Comparison with Fluid Friction, Trans. Am. Inst. Chem. Eng., Vol.29, pp. 174-210, 1933; reprinted in *International Journal of Heat and Mass Transfer*, Vol. 7, pp. 1359-1384, 1964.

46RO1 Rouse, H., *Elementary Mechanics of Fluids*, John Wiley and Sons, London, 1946.

50KA1 Kays, W.M., Loss Coefficients for Abrupt Changes in Flow Cross Section with Low Reynolds Number Flow in Single and Multiple-Tube Systems, *Transactions of the ASME*, Vol. 72, No. 8, pp. 1067-1074, 1950.

54FI1 Filonenko, G.K., Teploenergtika No. 4, 1954.

68KR1 Kröger, D.G. and Rohsenow, W.M., Condensation Heat Transfer in the Presence of a Non-Condensable Gas, *International Journal of Heat and Mass Transfer*, Vol. 11, pp. 15-26, 1968.

70HE1 Hewitt, G.F. and Hall-Taylor, N.S., *Annular Two-Phase Flow*, Pergamon Press, Oxford, 1970.

71DE1 Denny, V.E., Mills, A.F. and Jusionis, V.J., Laminar Film Condensation from a Steam-Air Mixture Undergoing Forced Flow Down a Vertical Surface, *Journal of Heat Transfer,* Vol. 93, pp. 297-304, 1971.

72KH1 Khan, R.A., Effect of Noncondensables in Sea Water Evaporators, *Chemical Engineering Progress,* Vol. 68, No. 7, pp. 79-80, 1972.

73AL1 Al-Diwany, H.K. and Rose, J.W., Free Convection Film Condensation of Steam Containing Small Concentrations of Air, *International Journal of Heat Mass Transfer,* Vol. 16, pp. 1359-1369, 1973.

74RA1 Rauscher, J.W., Mills, A.F. and Denny, V.E., Experimental Study of Film Condensation From Steam-Air Mixtures Flowing Downward Over a Horizontal Tube, *Journal of Heat Transfer*, Vol. 96, pp. 83-88, 1974.

74RO1 Rozemann, T. and Pundyk, J., Effect of Unequal Heat Loads on the Performance of Air Cooled Condensers, *AIChE Symposium Series*, Vol. 70, No. 138, pp. 178-184, 1974.

74ST1 Steinmeyer, D.E. and Mueller, A.C., Why Condensers don't operate as they are supposed to, *Chemical Engineering Progress,* Vol. 70, No. 7, pp. 78-82, 1974.

75GN1 Gnielinski, V., Forsch. Ing. Wesen, Vol. 41, No. 1, 1975.

80BE1 Berg, W.F. and Berg, J.L., Flow Patterns for Isothermal Condensation in One-Pass Air-Cooled Heat Exchangers, *Heat Transfer Engineering*, Vol. 1, No. 4, pp. 21-31, 1980.

84RO1 Roetzel, W., Berechnung von Wärmeübertragern, *VDI – Wärmeatlas*, pp. Ca1 – Ca31, VDI – Verlag GmbH, Düsseldorf, 1984.

85BE1 Bellstedt, M.O., Performance Prediction of Dry Cooling Towers, *M.Eng Thesis*, Department of Mechancical Engineering, University of Stellenbosch, Stellenbosch, South Africa, 1986.

85RO1 Rohsenow, W.M., Harnett, J.P. and Ganic, E.N., Condensation, *Handbook of Heat Transfer Fundamentals*, second edition, McGraw-Hill Book Company International, New York, 1985.

85VE1 Ventilatoren Stork Hengelo, General Instructions for E-type Fans, V.960874, 1985.

85VA1 Van Wylen, G.J. and Sonntag, R.E., *Fundamentals of Classical Thermodynamics*, third edition, John Wiley and Sons, New York, 1985.

86KO1 Kotzé, J.C.B., Ontwerp van Droë Direk Geforseerde en Inderek Natuurlike Konveksie Koeltorings, *M.Eng Thesis*, Department of Mechancical Engineering, University of Stellenbosch, Stellenbosch, South Africa. 1986.

86KR1 Kröger, D.G., Performance Characteristics of Industrial Finned Tubes Presented in Dimensional Form, *International Journal of Heat and Mass Transfer*, Vol. 29, No. 8, 1986.

88BE1 Bell, K.J., Design of Reflux Condensers, *Heat Transfer Equipment Design*, Ed. Shah, R.K., Subbarao, E.C. and Mashelkar, R.A., pp. 527-534, Hemisphere Publishing Corporation, New York, 1988.

88JE1 Jensen, M.K., Condensation with Non-condensables and in Multi-component Mixtures, *Heat Transfer Equipment Design*, Ed. Shah, R.K., Subbarao, E.C. and Mashelkar, R.A., pp 497-512, Hemisphere Publishing Corporation, New York, 1988.

88MU1 Mueller, A.C., Air Cooled heat Exchangers, *Heat Transfer Equipment Design*, Ed. Shah, R.K., Subbarao, E.C. and Mashelkar, R.A., pp. 179-189, Hemisphere Publishing Corporation, New York, 1988.

88SI1 Singh, K.P., Power Plant Surface Condenser Technology, *Heat Transfer Equipment Design*, Ed. Shah, R.K., Subbarao, E.C. and Mashelkar, R.A., pp 513-514, Hemisphere Publishing Corporation, New York, 1988.

89GO1 Goldwirt, F., Ghuzel, M. and Lemoine, P., Hydraulic Works Study of Golfech Cooling Towers, *Proceedings International Cooling-Tower Conference*, EPRI GS-6317, IAHR Cooling Tower Workshop, Pisa, Italy, 1989.

90VE1 Venter, S.J., The Influence of Distorted Flow Patterns on the Overall Performance of Axial Flow Fans, *Ph.D Thesis*, Departmant of Mechanical Engineering, University of Stellenbosch, Stellenbosch, South Africa, 1990.

91VE1 Venter, S.J. and Kröger, D.G., An Evaluation of Methods to Predict the System Effect Present in Air-Cooled Heat Exchangers, *Heat Recovery Systems and CHP*, Vol. 11, No. 5, pp. 431-440, 1991.

91CO1 Conradie, A.E., Evaluation of the performance Characteristics of Forced Draft Air-Cooled Heat Exchangers and the Effect of Plume Recirculation thereon, *M.Eng. Thesis*, Department of Mechanical Engineering, University of Stellenbosch, Stellenbosch, South Africa, 1991.

92CA1 Carey, Van P., *Liquid-Vapor Phase-Change Phenomena*, Hemisphere Publishing Corporation, Washington.

92HO1 Holman, J.P., *Heat Transfer*, Seventh Edition, McGraw-Hill Book Company International, Singapore, 1992.

93GR1 Groenewald, W., Heat Transfer and Pressure Change in an Inclined Air-Cooled Flattened Tube during Condensation of Steam, *M.Eng. Thesis*, Department of Mechanical Engineering, University of Stellenbosch, Stellenbosch, 1993.

93VA1 Van Aarde, D.J. and Kröger, D.G., Flow Losses Through an Array of A-frame Heat Exchangers, *Heat Transfer Engineering*, Vol. 14, No. 1, pp. 43-51, 1993.

94GE1 Gerald, C.F. and Wheatley, P.O., *Applied Numerical Analysis,* Fifth edition, Addison-Wesley Publishing Company, California, 1994.

94KR1 Kröger, D.G., Fan Performance in Air-Cooled Steam Condensers, *Heat Recovery Systems and CHP*, Vol. 14, No. 4, pp. 391-399, 1994.

94ZA1 Zapke, A., Pressure Gradient and Flooding during Two-Phase Counter-Current Flow in Inclined Tubes, *M.Eng. Thesis*, Department of Mechanical Engineering, University of Stellenbosch, Stellenbosch, South Africa, 1994.

95CO1 Conradie, A.E., Performance Optimization of Engineering Systems with Particular Reference to Dry-cooled Power Plants, *Ph.D Thesis*, Department of Mechanical Engineering, University of Stellenbosch, Stellenbosch, South Africa, 1995.

95DU1 Duvenhage, K. and Kröger, D.G., Plume Recirculation in Mechanical-Draft Air-Cooled Heat Exchangers, *Heat Transfer Engineering*, Vol. 16 No. 4, pp. 42-49, 1995.

95GR1 Groenewald, W. and Kröger, D.G., Effect of Mass Transfer on Turbulent Friction during Condensation inside Ducts, *International Journal of Heat and Mass Transfer*, Vol. 38, No. 18, pp. 3385-3392, 1995.

96ZA1 Zapke, A. and Kröger, D.G., The Influence of Fluid Properties and Inlet Geometry on Flooding in Vertical and Inclined Tubes, *International Journal of Multiphase Flow*, Vol. 22, No. 3, pp. 461-472, 1996.

96ZI1 Zipfel, T., Steam Flow Distribution in Air-Cooled Condensers, *M.Eng. Thesis*, Department of Mechanical Engineering, University of Stellenbosch, Stellenbosch, South Africa, 1996.

97SC1 Schoenfeld, P.D. and Kröger, D.G., Pressure Drop and Flooding During Reflux Condensation of Steam in an Inclined Duct, Department of Mechanical Engineering, University of Stellenbosch, Stellenbosch, South Africa, 1997.

97FA1 Fabbri, G., Analysis of the Non-condensable Contaminant Accumulation in Single-Pass Air Cooled Condensers, *Heat Transfer Engineering*, Vol. 18, No. 2, pp. 50-60, 1997.

97FA2 Fabbri, G., Analysis of Vapor Back Flow in Single-pass Air-cooled Condensers, *International Journal of Heat and Mass Transfer,* Vol. 40, No. 16, pp. 396-3979, 1997.

97ZA1 Zapke, A., Characteristics of Gas-Liquid Counterflow in Inclined Ducts with Particular Reference to Reflux Condensers, *Ph.D Thesis*, Department of Mechanical Engineering, University of Stellenbosch, Stellenbosch, South Africa, 1997.

97ZA2 Zapke, A., Personal Communication, Department of Mechanical Engineering, University of Stellenbosch, Stellenbosch, South Africa, 1997.

98KR1 Kröger, D.G., *Air-Cooled Heat Exchangers and Cooling Towers*, Begell House, New York, 1998.

98KR2 Kröger, D.G. and Zapke, A., Personal Communication, Department of Mechanical Engineering, University of Stellenbosch, Stellenbosch, South Africa, 1998.

98SC1 Schoenfeld, P.D., Pressure Drop During Reflux Condensation of Steam in an Inclined Elliptical Tube, *M.Eng. Thesis*, Department of Mechanical Engineering, University of Stellenbosch, Stellenbosch, South Africa, 1998.

98ZA1 Zapke, A., Personal Communication, Department of Mechanical Engineering, University of Stellenbosch, Stellenbosch, South Africa, 1998.

99MA1 Makhema, T., Personal Communication, Elliptical finned tube performance evaluation to be submitted for MSc.Eng. degree, Department of Mechanical Engineering, University of Stellenbosch, Stellenbosch, South Africa, 1999.

APPENDIX A

ANALYSIS OF A FORCED DRAUGHT DEPHLEGMATOR

A.1 Introduction

This appendix discusses the heat transfer and draught equations upon which the performance of a forced draught dephlegmator is based. The operating point of the dephlegmator is defined as that combination of air mass flow rate and air exit temperature that will simultaneously satisfy these equations. Furthermore, a pressure drop model proposed by Zapke [97AZ1], by which the inside pressure drop of the dephlegmator finned tubes can be predicted is also discussed.

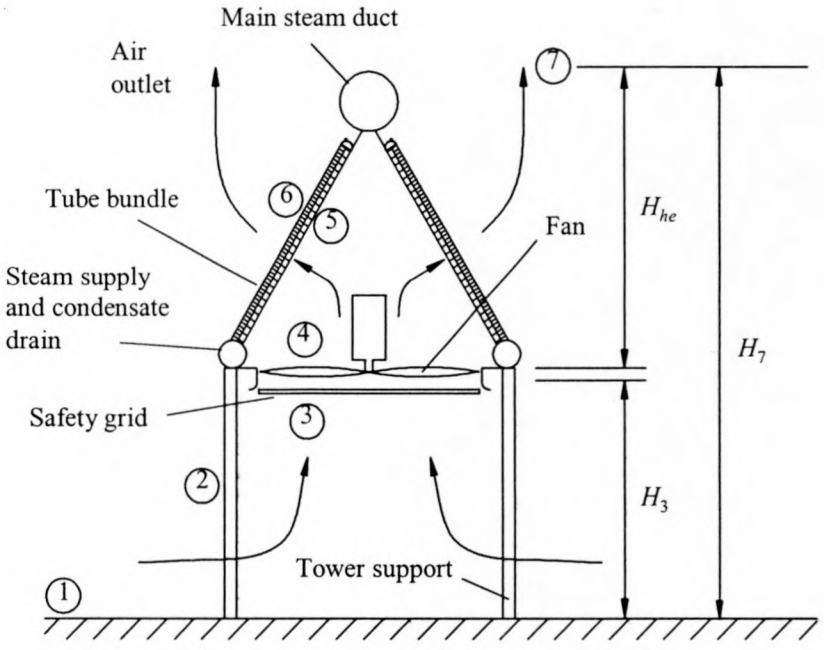

Figure A.1: Schematics of a typical forced draught dephlegmator unit.

A.2 The draught equation

As shown in figure A.1, a forced draught dephlegmator consists of a fan and a heat exchanger comprising of finned tube bundles. The system is installed at a reasonable height above the ground, H_3, to ensure adequate air supply to the system. As the air passes through the system, flow resistances imposed by the heat exchanger bundles and other flow obstacles have to be overcome. Equation (A.1) gives the draught equation as presented by Kröger [98KR1] with reference to figure A.1.

$$\begin{aligned} p_{a1} - p_{a7} = {} & \tfrac{1}{2}\rho_{a1}v_{a1}^2 K_{ts} + \tfrac{1}{2}\rho_{a3}v_{a3}^2 K_{up} - \tfrac{1}{2}\rho_{a3}v_{a3}^2 K_{Fs} + \tfrac{1}{2}\rho_{a4}v_{a4}^2 K_{do} \\ & + \tfrac{1}{2}\rho_{a56}v_{a56}^2 K_{he\theta} + p_{a1}\left[1-\left(1-0.00975H_3/T_{a1}\right)^{3.5}\right. \\ & + p_{a6}\left[1-\left(1-0.00975\left(H_7-H_6\right)/T_{a6}\right)^{3.5}\right] \end{aligned} \tag{A.1}$$

Substituting the relation $m_a = \rho_a v_a A$ into equation (A.1) gives the following.

$$\begin{aligned} p_{a1} - p_{a7} = {} & \frac{1}{2\rho_{a1}}\left(\frac{m_a}{A_2}\right)^2 K_{ts} + \frac{1}{2\rho_{a3}}\left(\frac{m_a}{A_{Fe}}\right)^2 K_{up} - \frac{1}{2\rho_{a3}}\left(\frac{m_a}{A_{Fc}}\right)^2 K_{Fs} \\ & + \frac{1}{2\rho_{a4}}\left(\frac{m_a}{A_{Fe}}\right)^2 K_{do} + \frac{1}{2\rho_{a4}}\left(\frac{m_a}{A_{Fe}}\right)^2 K_{he\theta} + p_{a1}\left[1-\left(1-0.00975H_3/T_{a1}\right)^{3.5}\right] \\ & + p_{a6}\left[1-\left(1-0.00975\left(H_7-H_6\right)/T_{a6}\right)^{3.5}\right] \end{aligned} \tag{A.2}$$

The draught equation implies that the pressure gain across the fan should be equal to the total pressure loss resulting from the flow obstacles at the operating point of the dephlegmator. The following section elaborates on the respective dimensionless loss coefficients of the draught equation.

A.2.1 Draught equation loss coefficients

K_{ts} is the loss coefficient of the dephlegmator tower supports, and is based on the conditions at the supports 2. Equation (A.3) gives K_{ts} as

$$K_{ts} = 2\Delta p_{ats} / \left(\rho_{a1} v_{a2}^2\right) = C_{Dts} L_{ts} d_{ts} n_{ts} / A_2 \tag{A.3}$$

where L_{ts} and d_{ts} is the tower support length and effective diameter or width respectively. A_2 is the area at the dephlegmator inlet, n_{ts}, is the number of tower supports and C_{Dts} is the drag coefficient of the tower supports.

According to Venter [90VE1] the fan static pressure rise coefficient is defined as follows:

$$K_{Fs} = 2\Delta p_{Fs} \rho_{a3} / \left(m_a / A_{Fc}\right)^2 \tag{A.4}$$

K_{up} and K_{do}, are the loss coefficients due to obstacles such as the fan safety grid, walkway and fan support structure at the up- and downstream sides of the fan. These loss coefficients are determined according to the bulk method proposed by Venter and Kröger [91VE1]. This method [85VE1] relates the total blockage area of the different flow distorting components, as well as the distance between the fan rotor and the respective components.

$$K_{up} = \Delta p_{up} / \left(\tfrac{1}{2} \rho_{a3} v_{a3}^2\right) = 2\Delta p_{up} \rho_{a3} / \left(m_a / A_{Fs}\right)^2 \tag{A.5}$$

$$K_{do} = \Delta p_{do} / \left(\tfrac{1}{2} \rho_{a4} v_{a4}^2\right) = 2\Delta p_{do} \rho_{a4} / \left(m_a / A_{Fs}\right)^2 \tag{A.6}$$

The flow area required in equations (A.5) and (A.6), is defined as $A_{Fs} = A_{Fc} - A_{Fh}$, where A_{Fc} and A_{Fh} are the fan casing and fan hub cross-sectional areas respectively.

The total heat exchanger loss coefficient, $K_{he\theta}$, takes into account the pressure loss across the inclined finned tube bundles, the turning and jetting losses and the kinetic

energy at 7. $K_{he\theta}$, is derived by Van Aarde and Kröger [93VA1], for an A-frame heat exchanger array operating under non-isothermal, oblique flow conditions as presented in equation (A.7).

$$K_{he\theta} = K_{heiso} + \frac{2}{\sigma^2}\left(\frac{\rho_{a5} - \rho_{a6}}{\rho_{a5} + \rho_{a6}}\right) + \left(\frac{1}{\sin\theta_m} - 1\right)\left(\frac{1}{\sin\theta_m} - 1 + 2K_c^{0.5}\right)$$
$$x\left(\frac{2\rho_{a6}}{\rho_{a5} + \rho_{a6}}\right) + K_d\left(\frac{2\rho_{a5}}{\rho_{a5} + \rho_{a6}}\right) \qquad \text{(A.7)}$$

σ is the ratio of the minimum free flow area through the heat exchanger bundle to the bundle frontal area. The isothermal heat exchanger loss coefficient for normal flow through the bundle, K_{heiso}, is determined under idealised isothermal conditions (See Appendix C) and accounts for the inlet-, frictional- and exit losses of the heat exchanger bundle. K_{heiso} is expressed in terms of the characteristic flow parameter, Ry, in exponential form as follows:

$$K_{heiso} = a_k Ry^{b_k} \qquad \text{(A.8)}$$

The third term on the right hand side of equation (A.7) accounts for additional losses incurred due to the oblique flow at the inlet to the tube bundles in terms of the bundle entrance loss coefficient, K_c. Kays [50KA1] gives the following expression for K_c for normal flow where σ_{21} is the ratio of the flow area between the fins to the free stream flow area at the inlet to the finned tube bundles.

$$K_c = \left[\frac{1}{\sigma_{21}}\left(\frac{1}{\sigma_c} - 1\right)\right]^2 \qquad \text{(A.9)}$$

The contraction coefficient, σ_c, may be approximated by the jet contraction ratio for parallel plates as given by Kröger [98KR1].

$$\sigma_c = 0.6144517 + 0.04566493\sigma_{21} - 0.336651\sigma_{21}^2 + 0.4082743\sigma_{21}^3 + 2.672041\sigma_{21}^4 - 5.963169\sigma_{21}^5 + 3.558944\sigma_{21}^6 \quad \text{(A.10)}$$

Owing to the flow distortion downstream of the tube bundle, the actual mean flow incidence angle will not be uniform along the bundle face. This effect causes the actual mean flow incidence angle to differ from the semi-apex angle, θ_b. Kotze [86KO1] gives the following equation for the mean incidence angle.

$$\theta_m = -3.1558 + 0.9133\theta_b + 0.0019\theta_b^2 \quad \text{(A.11)}$$

K_d, is the loss coefficient at the downstream side of the tube bundles. This loss coefficient consists of two components namely, K_{dj}, representing the losses due to the turning and jetting of the flow in the V-region, and K_o, representing the loss of kinetic energy into the atmosphere. Van Aarde and Kröger [93VA1], gives the following empirical correlations for the respective downstream loss components.

$$K_{dj} = \left\{ \left[-2.81919\left(\frac{0.5L_w}{L_t}\right) + 2.9329\left(\frac{0.5L_w}{L_t}\right)^2 \right] \left[\sin\theta_b - \frac{d_{sd}}{2L_t} + \frac{0.5L_w}{L_t} \right]^{-1} x \left(\frac{28}{\theta_b}\right)^{0.4} \left[1 - \frac{0.5d_{sd}/L_t}{\sin\theta_b + 0.5L_w/L_t} \right]^{-1} + \left[exp\left(2.36987 + 5.8601x10^{-2}\theta_b - 3.3797x10^{-3}\theta_b^2\right) \right]^{0.5} x \left[1 - \frac{0.5d_{sd}/L_t}{\sin\theta_b + 0.5L_w/L_t} \right]^{0.5} \left[1 + \frac{0.5L_w}{L_t \sin\theta_b} \right]^{-1} \right\}^2 \quad \text{(A.12)}$$

and

$$K_o = \left\{ \left[-2.89188\left(0.5\frac{L_w}{L_t}\right) + 2.9329\left(0.5\frac{L_w}{L_t}\right)^2 \right] \left[1 - \frac{0.5d_{sd}/L_t}{\sin\theta_b + 0.5L_w/L_t} \right]^3 + 1.9874 - 3.02783\left[\frac{0.5d_{sd}/L_t}{\sin\theta_b + 0.5L_w/L_t} \right] + 2.0817\left[\frac{0.5d_{sd}/L_t}{\sin\theta_b + 0.5L_w/L_t} \right]^2 \right\} x \left(\sin\theta_b - \frac{d_{sd}}{2L_t} + \frac{L_w}{L_t} \right)^{-2} \quad \text{(A.13)}$$

L_t is the tube length of a cooling unit, L_w is the width of the walkway between the fan units and d_{sd} is the diameter of the main steam duct on top of the ACC system. Thus, $K_d = K_{dj} + K_o$. Both equations (A.12) and (A.13) are valid in the following ranges.

$$20° \le \theta_b \le 35°$$

$$0 \le \frac{0.5 d_{sd} / L_t}{\sin\theta_b + L_w / L_t} \le 0.17886$$

$$0 \le L_w / L_t \le 0.09033$$

$$0 \le d_{sd} / L_t \le 0.303 \qquad \text{for } L_w = 0$$

$$K_{he} \ge 30$$

A.3 Heat transfer equations

To satisfy the heat transfer equations, the heat absorbed by the air flowing across the finned tubes of the heat exchanger, should be equal to the heat rejected in the condensation process of the steam inside the finned tubes.

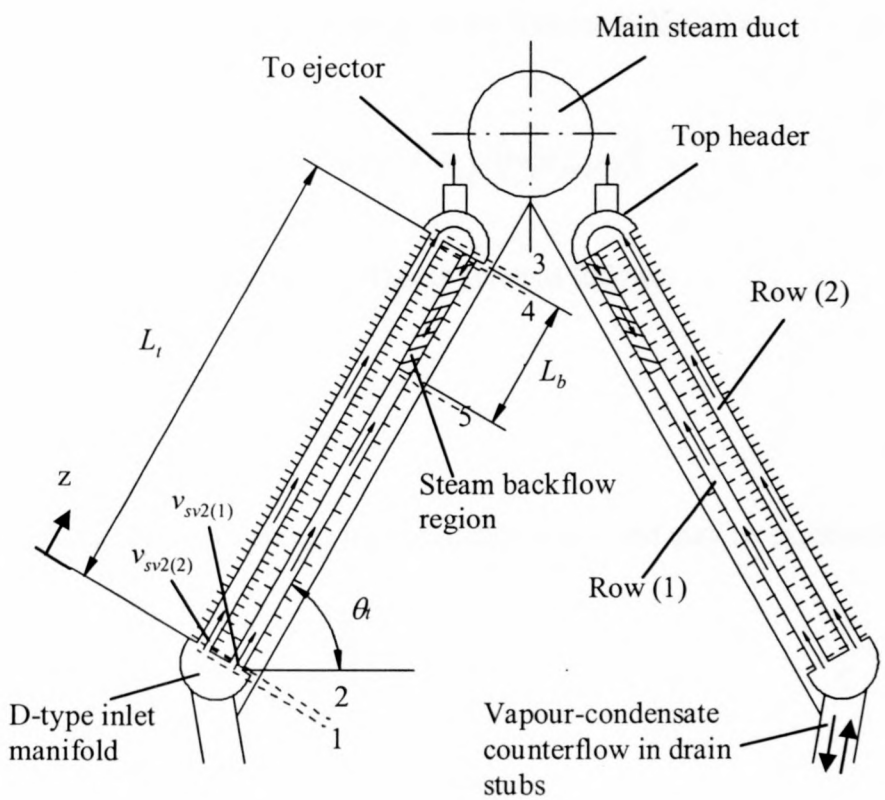

Figure A.2: Schematics of a forced draught double-row dephlegmator.

Zapke [97ZA1] gives the following heat transfer analysis, of a forced draught dephlegmator system as shown in figure A.2. Equation (A.14) gives the heat transfer from the condensing steam to the air passing through the finned tube bundles of a dephlegmator fan unit.

$$Q_a = \sum_{i=1}^{n_{tr}} Q_{a(i)} = \sum_{i=1}^{n_{tr}} m_a c_{pam(i)} e_{(i)} \left(T_{vm(i)} - T_{ai(i)}\right) = \sum_{i=1}^{n_{tr}} m_{c(i)} i_{lg(i)}$$

$$= \sum_{i=1}^{n_{tr}} m_a c_{pam(i)} \left(T_{ao(i)} - T_{ai(i)}\right) \qquad \text{(A.14)}$$

The heat transfer analysis applies for each of the respective tube rows and the heat transfer should be calculated for each tube row individually. In order to satisfy the heat transfer criteria of the dephlegmator unit, equation (A.14) must be satisfied.

In the case of condensation, where the fluid temperature stays essentially constant, the effectiveness for each tube row, $e_{(i)}$, is given by Holman [92HO1] as

$$e_{(i)} = 1 - exp\left(-UA_{(i)} / C_{min(i)}\right) = 1 - exp\left(-UA_{(i)} / \left(m_a c_{pam(i)}\right)\right) \qquad \text{(A.15)}$$

The overall thermal conductance, $(UA)_{(i)}$, is given as follows:

$$\left(UA\right)_{(i)} = \left[1 / h_{ae(i)} A_{a(i)} + 1 / h_{c(i)} A_{c(i)}\right]^{-1} \qquad \text{(A.16)}$$

where $h_{ae}A_a$ is the effective airside thermal conductance and may be expressed as

$$\left(h_{ae} A_a\right)_{(i)} = \left[\frac{1}{h_{a(i)} e_{f(i)} A_{a(i)}} + \sum_n \frac{R_n}{A_n}\right]^{-1} \qquad \text{(A.17)}$$

The summation term represents the thermal resistances owing to the tube wall, fouling and thermal contact resistance between the tube and fin. $h_{ae}A_a$ of the specific finned

tube bundle may be determined experimentally, under idealised conditions in a windtunnel, and presented in the dimensional form as proposed by Kröger [86KR1]

$$\left(h_{ae}A_a\right)_{(i)} = Ny_{(i)}k_{am(i)}\,Pr_{am(i)}^{1/3}\,A_{fr(i)} \tag{A.18}$$

Appendix C gives a description of the experimental apparatus and test procedure used to determine the effective airside thermal conductance. Ry [m^{-1}] is known as the characteristic flow parameter and is given by the following relation.

$$Ry_{(i)} = \frac{m_a}{\mu_{am(i)}A_{fr(i)}} \tag{A.19}$$

Groenewald [93GR1] developed the following correlation to determine the condensation heat transfer coefficient for flattened tubes.

$$h_{c(i)} = 0.9245\left[\frac{L_t k_{c(i)}^3 \rho_{c(i)}^2 g\cos(\theta_t) i_{lg(i)}}{\mu_{c(i)} m_{ah(i)} c_{pam(i)}\left(T_{vm(i)} - T_{ai(i)}\right)\left\{1-\exp\left\{-\left(U_{c(i)}H_t L_t\right)/\left(m_{ah}c_{pam(i)}\right)\right\}\right\}}\right]^{0.333} \tag{A.20}$$

m_{ah} is the air mass flow rate flowing on one side of the test tube as given by the following

$$m_{ah} = m_a / 2 \tag{A.21}$$

The overall heat transfer coefficient based on the condensation surface area may be approximated by

$$U_{c(i)}H_t L_t = \left(h_{ae}A_a\right)_{(i)} / \left(2n_{tb}n_b\right) \tag{A.22}$$

where the thermal resistance of the condensate film has been neglected. The inside exposed tube surface area of each tube row is determined as follows

$$A_{c(i)} = n_b n_{tr(i)} A_{ti} L_t \tag{A.23}$$

The heat transfer and subsequent rate of condensation, of each tube row is calculated by means of equations (A.14) to (A.23) with the air flow rate, inlet air temperature and saturation steam temperature as input values. All properties are evaluated at the relevant arithmetic mean temperature.

The mean vapour temperature, $T_{vm(i)}$, required in equations (A.14) and (A.20) is approximated as the saturation vapour temperature corresponding to the mean, static tube row pressure, $p_{vm(i)}$. Zapke [97ZA1] gives the following equation for mean static pressure, $p_{vm(i)}$, in the tube

$$p_{vm(i)} = p_{v1} - \Delta p_{12(i)} - \tfrac{1}{2}\rho_{v(i)} v_{sv2(i)}^2 \frac{L}{d_e} \frac{K\, Re_{sv2(i)}^n}{\left(1 - v_{sv3(i)}/v_{sv2(i)}\right)} \left[\frac{a1}{n+3} x \right.$$

$$\left. \left(1 - \frac{v_{sv3(i)}^{n+4} - v_{sv2(i)}^{n+4}}{v_{sv2(i)}^{n+3}(n+4)\left(v_{sv3(i)} - v_{sv2(i)}\right)}\right) + \frac{a_2}{(n+2) Re_{sv2(i)}} \left(1 - \frac{v_{sv3(i)}^{n+3} - v_{sv2(i)}^{n+3}}{v_{sv2(i)}^{n+2}(n+4)\left(v_{sv3(i)} - v_{sv2(i)}\right)}\right)\right]$$

$$+ \tfrac{1}{2}\rho_{v(i)} g L_t \sin\theta_t + \rho_{v(i)} \left(\tfrac{1}{3} v_{sv3(i)}^2 + \tfrac{1}{3} v_{sv2(i)} v_{sv3(i)} + \tfrac{2}{3} v_{sv2(i)}^2\right) \tag{A.24}$$

where K = 0.5046 and n = -0.2883. The vapour and condensate properties for each tube row are evaluated at the saturation temperature corresponding to the mean vapour pressure. Kröger [98KR1] gives the following expression for the saturated steam temperature, given the mean saturated vapour pressure.

$$T_{vm} = 5149.6889682 / \left[\ln\left(1.020472843 x 10^{11} / p_{vm}\right)\right] \tag{A.25}$$

The operating point of a the dephlegmator is defined as that combination of air mass flow rate and air exit temperature that will simultaneously satisfy the draught- and heat transfer equations.

Conradie [91CO1] developed a computer simulation program with which the performance characteristics of forced draught direct air-cooled condensers for power stations can be evaluated. The program provides a fast and effective method to determine the cooling capacity of such systems under various design conditions.

A.3.1 Inside tube pressure drop model

Zapke [97ZA1] gives the following analysis by which the inside pressure drop across the finned tubes of a dephlegmator unit can be accurately predicted. Figure A.2 shows the schematics of a forced draught, double-row dephlegmator unit. The heat transfer characteristics of the tube rows of the investigated system are such that row (1) condenses slightly more steam than row (2). It can therefore be assumed that steam backflow will occur from the top of row (2) into the top of row (1). This backflow region is clearly shown in figure 3.2 and the length of the backflow region is denoted by L_b.

A.3.2 Conservation of mass.

The following mass flow balance applies for each tube row respectively.

$$m_{v2(1)} + m_{v3(1)} = m_{c(1)} \tag{A.26}$$

$$m_{v2(2)} - m_{v3(2)} = m_{c(2)} \tag{A.27}$$

where m_v and m_c are the vapour and condensate mass flow rates respectively.

The heat transfer along the finned tubes can be considered as a constant heat flux process and thus:

$$\frac{m_{v3(2)}}{m_{c(2)}} = \frac{L_b}{L_t} \tag{A.28}$$

Due to the backflow phenomena, outflow vapour from tube row (2) enters row (1) via the top header and at the same time, vapour along with accumulated non-condensable gases are removed by the ejector. The top header mass balance is therefore

$$m_{v3(1)} + m_{ej} = m_{v3(2)} \tag{A.29}$$

A.3.3 Momentum equations

The pressure drop across tube row (2) is evaluated firstly and is given by the following equation.

$$\Delta p_{14(2)} = \Delta p_{12(2)} + \Delta p_{23(2)} + \Delta p_{34(2)} \tag{A.30}$$

where $\Delta p_{12(2)}$ is the change in pressure experienced by the vapour entering the second tube row from the bottom header, while $\Delta p_{23(2)}$ is the inside tube pressure drop experienced through the length of the finned tube. The pressure loss, $\Delta p_{34(2)}$, is experienced at the outlet of row (2) due to steam exiting this tube row as a result of the backflow phenomena.

According to Zapke the entrance pressure drop in the presence of draining condensate can be expressed as

$$\Delta p_{12(2)} = \tfrac{1}{2} \rho_{v(2)} v_{sv2(2)}^2 \left[K_{tp} - \sigma_{21}^2 \right] \tag{A.31}$$

where K_{tp} is a two-phase entrance loss coefficient, and a function of the densimetric gas froude number, Fr_{Hsg}. Zapke [97ZA1] gives the following correlation for the two-phase loss coefficient

$$K_{tp} = 1.622 + 2.078 Fr_{Hsg} \tag{A.32}$$

This correlation is only valid for steady, counter-flow conditions where $0.03 \leq Fr_{Hsg} \leq 0.4$, and for a tube inclination angle of $\theta_t = 60\ ^{\circ}$. Equation (A.32) does therefore not incorporate the unsteady nature of the pressure drop associated with tube flooding.

The inside pressure drop between any two sections, c and *d*, of a typical inclined dephlegmator finned tube is presented in terms of a frictional, gravitational and momentum component, as follows:

$$\Delta p_{cd} = \Delta p_f + \Delta p_g + \Delta p_m$$

$$= \int_{L_c}^{L_d} \beta \left(\frac{dp}{dz} \right)_{ftp} dz + \int_{L_c}^{L_d} g \rho_v \sin\theta_t dz + \int_{L_c}^{L_d} -\frac{d}{dz}\left(\rho_v v_{sv}^2 \right) dz \tag{A.33}$$

where $(dp/dz)_{ftp}$ is the frictional pressure gradient experienced by a gas during adiabatic counter-current gas-liquid flow. At high vapour flows, entrainment and wave action at the vapour-liquid interface cause the two-phase friction factor to rise above the single-phase friction prediction. Zapke [97ZA1] however states that the operating range of the dephlegmator is such that the two-phase friction factor does not deviate significantly from the single-phase friction factor. The friction factor may therefore be correlated in the form of a Blasius-type relation, as a function of the superficial vapour Reynolds number

$$f_{sv} = K\, Re_{sv}^{n} \tag{A.34}$$

where K = 0.2259 and n = -0.2088 for turbulent flow between parallel plates. In the absence of significant vapour-condensate interactions along the entire finned tube length, Groenewald and Kröger [95GR1] gives the following approximation for the frictional pressure gradient.

$$\left(\frac{dp}{dz}\right)_{ftp} = f_{sv}\frac{1}{d_e}\frac{1}{2}\rho_v v_{sv}^2 \tag{A.35}$$

The following function is also presented by Groenewald and Kröger [95GR1] and gives β for condensation during turbulent flow inside flattened tubes or rectangular ducts of high aspect ratio.

$$\beta = a_1 + a_2 / Re_{sv} \tag{A.36}$$

a_1 and a_2 are functions of the suction Reynolds number Re_{vn} and presented as follows:

$$a_1 = 1.0649 + 1.0411x10^{-3}\, Re_{vn} - 2.011x10^{-7}\, Re_{vn}^3 \tag{A.37a}$$

$$a_2 = 290.1479 + 59.3153\, Re_{vn} + 1.5995x10^{-2}\, Re_{vn}^3 \tag{A.37b}$$

Equation (A.37) is valid for $0 \le Re_{vn} \le 40$ and Re_{vn} is expressed as:

$$Re_{vn} = m_c d_e / (\mu_v n_{tb} n_b L_t A_{ti}) \tag{A.38}$$

Due to condensation of the steam inside tube row (2), the variation in the vapour velocity along the axial direction of the finned tube may be approximated by the following, linear relation.

$$v_{sv(2)} = (v_{sv3(2)} - v_{sv2(2)})z / L_t + v_{sv2(2)} \tag{A.39}$$

Substitute equations (A.34) to (A.39) into equation (A.33) and integrate to obtain the total inside pressure loss across tube row (2).

$$\Delta p_{23(2)} = \tfrac{1}{2}\rho_{v2}v_{sv2(2)}^2\left[\frac{L_t}{d_e}\frac{K\,Re_{sv2(2)}^n}{\left(1-v_{sv3(2)}/v_{sv2(2)}\right)}\left(\frac{a_1\left(1-\left(v_{sv3(2)}/v_{sv2(2)}\right)^{n+3}\right)}{n+3}\right.\right.$$

$$\left.\left.+\frac{a_2\left(1-\left(v_{sv3(2)}/v_{sv2(2)}\right)^{n+2}\right)}{(n+2)Re_{sv2(2)}}\right)\right]$$

$$+\rho_{v(2)}gL_t\sin\theta_t+\left(\rho_{v(2)}v_{sv2(2)}^2-\rho_{v(2)}v_{sv3(2)}^2\right) \qquad \text{(A.40)}$$

According to Kröger [98KR1], the pressure loss due to steam outflow at the exit of tube row (2), may be presented in terms of a single-phase exit coefficient, K_{esp}.

$$\Delta p_{34(2)} = \tfrac{1}{2}\rho_{v(2)}v_{sv3(2)}^2\left[\left(\sigma_{34}^2-1\right)+K_{esp}\right] \qquad \text{(A.41)}$$

Upon substitution of the relevant pressure drop components as given by equations (A.31), (A.40) and (A.41) into equation (A.30), the total pressure drop across the headers of row (2) is found to be

$$\Delta p_{14(2)} = \tfrac{1}{2}\rho_{v(2)}v_{sv2(2)}^2\left(K_{tp(2)}-\sigma_{21}^2\right)+\tfrac{1}{2}\rho_{v(2)}v_{sv2(2)}^2\left[\frac{L_t}{d_e}\frac{K\,Re_{sv2(2)}^n}{\left(1-v_{sv3(2)}/v_{sv2(2)}\right)}x\right.$$

$$\left.\left(\frac{a_1\left(1-\left(v_{sv3(2)}/v_{sv2(2)}\right)^{n+3}\right)}{n+3}+\frac{a_2\left(1-\left(v_{sv3(2)}/v_{sv2(2)}\right)^{n+2}\right)}{(n+2)Re_{sv2(2)}}\right)\right]+\rho_{v(2)}gL_t\sin\theta_t$$

$$-\left(\rho_{v(2)}v_{sv2(2)}^2-\rho_{v(2)}v_{sv3(2)}^2\right)+\tfrac{1}{2}\rho_{v(2)}v_{sv3(2)}^2\left[\left(\sigma_{34}^2-1\right)+K_{esp}\right] \qquad \text{(A.42)}$$

The pressure drop across tube row (1) is now evaluated and presented by the following equation.

$$\Delta p_{14(1)} = \Delta p_{15(1)}+\Delta p_{54(1)} = \left(\Delta p_{12(1)}+\Delta p_{25(1)}\right)+\left(\Delta p_{53(1)}+\Delta p_{34(1)}\right) \qquad \text{(A.43)}$$

where $\Delta p_{15(1)}$ is the change in pressure experienced by the vapour entering from the bottom header, while $\Delta p_{54(1)}$ is the pressure rise experienced in the backflow region.

The entrance pressure drop, $\Delta p_{12(1)}$, is calculated in similar fashion to the entrance pressure drop of row (2), by means of equation (A.31).

The inside tube pressure drop, $\Delta p_{25(1)}$, is calculated by means of equation (A.33), and is the resultant pressure drop between the bottom of the tube and the start of the backflow region. The variation of the vapour velocity in the upflow region of row (1) is given by

$$v_{sv(1)} = v_{sv2(1)}\left(1 - z/\left(L_t - L_b\right)\right) \tag{A.44}$$

Substitute equations (A.34) to (A.38) and (A.44) into equation (A.33) and integrate to obtain

$$\Delta p_{25(1)} = \tfrac{1}{2}\rho_{v(1)}v_{sv2(1)}^2\left[\frac{\left(L_t - L_b\right)}{d_e}K\,Re_{sv2(1)}^n\left(\frac{a_1}{n+3} + \frac{a_2}{\left(n+2\right)Re_{sv2(1)}}\right)\right]$$

$$+ \rho_{v(1)}g\left(L_t - L_b\right)\sin\theta_t - \rho_{v(1)}v_{sv2(1)}^2 \tag{A.45}$$

The pressure drop for the backflow region can be evaluated in similar fashion and the same governing equations are used. Due to co-current flow conditions in the backflow region, there is no condensate drainage at the top of the tube, and the entrance pressure drop can be presented in terms of a single-phase loss coefficient, K_{csp}.

$$\Delta p_{34(1)} = -\tfrac{1}{2}\rho_{v(1)}v_{sv3(1)}^2\left[\left(1 - \sigma_{34}^2\right) + K_{csp}\right] \tag{A.46}$$

Upon substitution of the relevant equations into equation (A.33) and integrating gives the inside tube pressure loss in the backflow region as

$$\Delta p_{53(1)} = -\tfrac{1}{2}\rho_{v(1)}v_{sv3(1)}^2\left[\frac{L_b}{d_e}K\,Re_{sv3(1)}^n\left(\frac{a_1}{n+3} + \frac{a_2}{\left(n+2\right)Re_{sv3(1)}}\right)\right]$$

$$- \rho_{v(1)}gL_b\sin\theta_t + \rho_{v(1)}v_{sv3(1)}^2 \tag{A.47}$$

Substitution of the relevant pressure drop components into equation (A.43) gives the pressure drop across the headers of tube row (1) as

$$\Delta p_{14(1)} = \tfrac{1}{2}\rho_{v(1)}v_{sv2(1)}^2\left[\left(K_{tp(1)} - \sigma_{21}^2\right) + \frac{L_t - L_b}{d_e}K\,Re_{sv2(1)}^n\left(\frac{a_1}{n+3} + \frac{a_2}{(n+2)Re_{sv2(1)}}\right)\right]$$

$$-\tfrac{1}{2}\rho_{v(1)}v_{sv3(1)}^2\left[\left(1 - \sigma_{34}^2 + K_{csp(1)}\right) + \frac{L_b}{d_e}K\,Re_{sv3(1)}^n\left(\frac{a_1}{n+3} + \frac{a_2}{(n+2)Re_{sv3(1)}}\right)\right]$$

$$+\rho_{v(1)}gL_t\sin\theta_t - \left(\rho_{v(1)}v_{sv2(1)}^2 - \rho_{v(1)}v_{sv3(1)}^2\right) \qquad \text{(A.48)}$$

Since the two tube rows share a common inlet manifold and outlet header, the following relation must be satisfied.

$$\Delta p_{14(1)} = \Delta p_{14(2)} \qquad \text{(A.49)}$$

Given the respective condensation rates, $m_{c(1)}$ and $m_{c(2)}$ and the ejector suction rate m_{ej}, equations (A.26) to (A.29) and the equal header pressure drop condition stated by equation (A.49) can be used in order to solve for the five variables $v_{sv2(1)}$, $v_{sv2(2)}$, $v_{sv3(1)}$, $v_{sv3(2)}$ and L_b.

This pressure drop model is only valid for cases where no flooding of the dephlegmator bundle tubes are present.

A.3.4 Flooding prediction for inclined ducts operating under two-phase counter-flow conditions

Zapke and Kröger [96ZA1] devised the following analysis by which the flooding in inclined rectangular ducts, such as dephlegmator bundle tubes, can be accurately predicted. Flooding is governed by the vapour Froude number, and flooding data is therefore presented in terms of a dimensionless densimetric gas Froude number based on the duct or tube height, H_t.

$$Fr_{Hsg} = \frac{\rho_g v_{sg}^2}{gH_t(\rho_l - \rho_g)} \tag{A.50}$$

In order to predict the densimetric gas Froude number at which flooding will occur in inclined ducts, the relevant fluid properties and duct dimension are presented in the dimensionless *Zk*-number.

$$Zk_d = \frac{(\rho_l d_e \sigma)^{0.5}}{\mu_l} \tag{A.51}$$

As is the case for most liquids, the surface tension for water decreases almost linearly with an increase in temperature. Carey [92CA1] gives the following correlation for the water surface tension required by equation (A.51).

$$\sigma = 75.83 - 0.1477T_w \tag{A.52}$$

Equation (A.52) is valid over the temperature range of 10 °C < T_w < 100 °C.

The following correlation predicts the densimetric gas Froude number at which flooding will occur in rectangular, inclined tubes, upon substitution of the *Zk* number.

$$Fr_{Hsg} = K_o \exp\left(-nFr_{dsl}^{0.6} / Zk_d^{0.2}\right) \tag{A.53}$$

where n and K_o are empirical constants related to the duct inclination angle. These constants are given by the following correlated equations.

$$K_o = 7.9143x10^{-2} + 4.9705x10^{-3}\theta + 1.5183x10^{-4}\theta^2 - 1.9852x10^{-6}\theta^3 \tag{A.54}$$

$$n = 1.8149x10^{1} - 1.9471\theta + 6.7058x10^{-2}\theta^2 - 5.3227x10^{-4}\theta^3 \tag{A.55}$$

Equations (A.53) and (A.54) are valid for inclination angles $2^{o} \leq \theta \leq 80^{o}$. Fr_{dsl}, is the densimetric liquid Froude number, based on the equivalent diameter, and presents the liquid flow rate.

$$Fr_{dsl} = \frac{\rho_l v_{sl}^2}{g d_e (\rho_l - \rho_g)} \tag{A.56}$$

Schoenfeld [97SC1] investigated reflux condensation in a full scale, inclined elliptical finned tube condensing low-pressure steam. Good agreement was obtained between the experimental results and the tube pressure drop and flooding models presented by Zapke and Kröger [96ZA1].

A.4 Conclusion

This analysis is of importance to the design of ACC systems and enables one to predict the various heat transfer and pressure drop characteristics of the system beforehand. Small design modifications in ACC systems may result in major savings in capital and running costs over the projected life of the power station.

APPENDIX B

FINNED TUBE CROSS-SECTIONAL FLOW GEOMETRY

B.1 Introduction

Figure B.1 shows a detailed cross-section drawing of an elliptical finned tube similar to the tubes used in the various experimental tests applicable to this dissertation. This appendix illustrates the calculation of the finned tube cross-sectional flow area, inside wetted area per meter length as well as the finned tube hydraulic tube diameter. These geometry values are required for the various sample calculations in the following Appendixes.

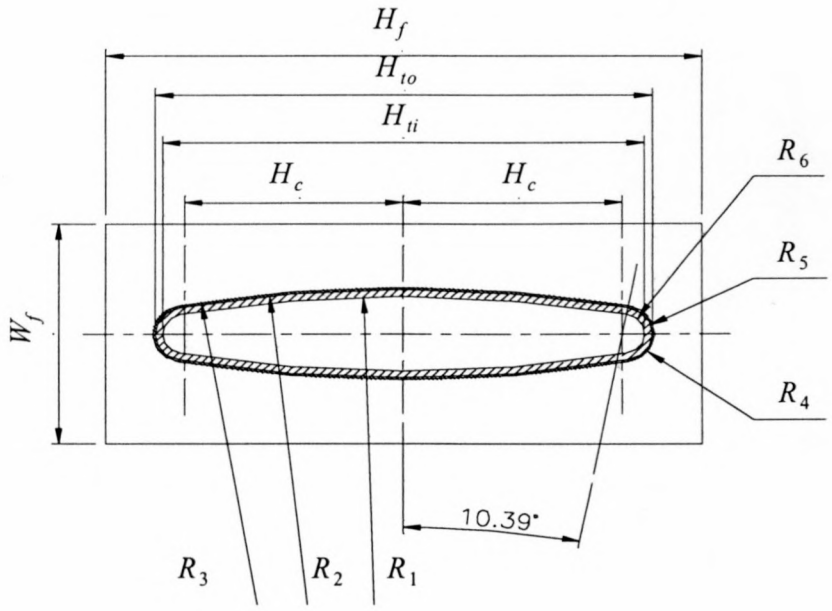

Figure B.1: Detailed drawing of the finned tube cross-section.

B.2 Calculations

Tube geometry as shown in figure B.1:

Outside tube height	H_{to}	=	0.1 m
Inside tube height	H_{ti}	=	0.097 m
Fin height	H_f	=	0.12 m
Fin width	W_f	=	0.05 m
Outside tube width	W_{ti}	=	0.02 m
Radius 1	R_1	=	0.2485 m
Radius 2	R_2	=	0.25 m
Radius 3	R_3	=	0.2505 m
Radius 4	R_4	=	0.0065 m
Radius 5	R_5	=	0.006 m
Radius 6	R_6	=	0.0045 m
Tube Height 1	H_c	=	0.044 m

Inside tube cross-sectional flow area, A_{tc}:

$$A_{tc} = 4\left[\left(\frac{\phi}{360}\right)R_1^2\pi - \tfrac{1}{2}H_c\left(R_2 - W_{ti}/2\right)\right] + 4\left[\frac{90-\phi}{360}R_6^2\pi\right] \qquad \text{(B.1)}$$

where

$$\phi = arctan\left(\frac{H_1}{R_2 - W_{ti}/2}\right) = arctan\left(\frac{0.044}{0.25 - 0.02/2}\right) = 10.388858\ ^{o}$$

Substituting into equation (B.1) gives

$$A_{tc} = 4\left[\frac{10.388858}{360}0.2485^2\pi - \frac{1}{2}0.044(0.25 - 0.01)\right] + 4\left[\frac{90-10.388858}{360}0.0045^2\pi\right]$$

$$= 1330.08228\ x\ 10^{-6}\ \text{m}^2$$

Inside wetted area per unit length, A_{ti}:

$$A_{ti} = 4\left[\frac{\phi}{180} R_1 \pi\right] + 4\left[\frac{90-\phi}{180} 2R_6 \pi\right] \tag{B.2}$$

$$= 4\left[\frac{10.388858}{360} x2x0.2485x\pi\right] + 4\left[\frac{90-10.388858}{360} x2x0.0045x\pi\right]$$

$$= 205.242437 \; x \; 10^{-3} \; \text{m}^2/\text{m}$$

Hydraulic tube diameter, d_e:

$$d_e = \frac{4A_{tc}}{P_w} \tag{B.3}$$

where

$$P_w = 4\left[\frac{\phi}{180} R_1 \pi\right] + 4\left[\frac{90-\phi}{180} R_6 \pi\right]$$

$$= 4\left[\frac{10.388858}{360} x2x0.2485x\pi\right] + 4\left[\frac{90-10.388858}{360} x2x0.0045x\pi\right]$$

$$= 205.242437 \; x \; 10^{-3} \; \text{m}$$

Substituting into equation (B.3) gives

$$d_e = \frac{4x1330.08228x10^{-6}}{205.25237x10^{-3}} = 25.922169x10^{-3} \; \text{m}$$

Projected tube pitch area, A_{tp}:

$$A_{tp} = H_f x W_f = 0.12x0.05 = 0.006 \, \text{m}^2$$

APPENDIX C

FINNED TUBE PERFORMANCE EVALUATION AND THE MATCHING OF HEAT TRANSFER CHARACTERISTICS IN A DOUBLE ROW, AIR-COOLED CONDENSER SYSTEM

C.1 Introduction

Matching heat transfer of the first and second tube row of a double row condenser or dephlegmator system, can be achieved by reducing the fin pitch of the second tube row as stated by Berg and Berg [80BE1]. These matched heat transfer characteristics will however only be valid for a particular operating condition.

The performance characteristics of four different, single row finned tube bundles, with fin pitch of 2.2, 2.3, 2.4, and 2.5 mm respectively are determined and used to illustrate the row heat transfer matching of a particular ACC system. Account is also given of the experimental heat exchanger performance data presentation as proposed by Kröger [86KR1] and the experimental apparatus that is used to generate the finned tube performance data is discussed.

C.2 Presentation of heat exchanger performance data

The presentation of heat exchanger performance data must be clear and should enable easy comparison between different heat exchangers. A method proposed by Kröger [86KR1] is used to present the experimentally obtained finned tube performance data for the respective evaluated finned tube bundles.

Heat transfer characteristics are presented in terms of the characteristic heat transfer- and flow parameter as given by the following equation.

$$Ny = h_{ae} A_a / \left(k A_{fr} \, Pr^{0.333} \right) = a_{Ny} Ry^{b_{NY}} \tag{C.1}$$

Ny is the characteristic heat transfer parameter and Ry is the characteristic flow parameter. Equation (C.2) gives Ry as follows:

$$Ry = G_{fr} / \mu = m / \left(\mu A_{fr} \right) \tag{C.2}$$

The effective heat transfer coefficient, h_{ae}, is given by the following equation.

$$h_{ae} A_a = \left(\frac{1}{h_a e_f A_a} + \sum_n \frac{R_n}{A_n} \right)^{-1} = \left(\frac{F_T \Delta T_{lm}}{Q_a} - \frac{1}{h_w A_w} \right)^{-1} \tag{C.3}$$

The R_n/A_n terms represent the heat transfer resistances owing to the tube wall, fouling and a thermal contact resistance between the tube and the fin. These resistances are usually poorly defined, and the effective heat transfer coefficient is therefore determined by means of the right hand side of equation (C.3). The required variables such as the logarithmic mean temperature difference, ΔT_{lm}, the air-side heat transfer, Q_a, and the water-side heat transfer coefficient, h_w, are experimentally determined during a performance test in a windtunnel. Equations (C.4) and (C.5) respectively gives ΔT_{lm} and Q_a as follows:

$$\Delta T_{lm} = \frac{\left(T_{wo} - T_{ai} \right) - \left(T_{wi} - T_{ao} \right)}{ln\left[\left(T_{wo} - T_{ai} \right) / \left(T_{wi} - T_{ao} \right) \right]} \tag{C.4}$$

$$Q_a = m_a c_{pm} \left(T_{ao} - T_{ai} \right) \tag{C.5}$$

The required temperature correction factor, F_T, is calculated by means of equation (C.6) as given by Roetzel [84RO1].

$$F_T = 1 - \sum_{i=1}^{4}\sum_{k=1}^{4} a_{i,k}\left(1-\phi_{cf}\right)^k \sin\left(2i \arctan\frac{\phi_h}{\phi_c}\right) \tag{C.6}$$

where the dimensionless temperature changes of the two streams are respectively defined as

$$\phi_h = \frac{T_{hi} - T_{ho}}{T_{hi} - T_{ci}} \tag{C.7}$$

and

$$\phi_c = \frac{T_{co} - T_{ci}}{T_{hi} - T_{ci}} \tag{C.8}$$

In the case of counter-flow conditions, a dimensionless mean temperature difference can be expressed in terms of the logarithmic mean temperature difference as follows:

$$\phi_{cf} = \frac{\Delta T_{lm}}{T_{hi} - T_{ci}} \tag{C.9}$$

The test bundle has a cross-flow, single pass, single row heat exchanger geometry. Table C.1 gives the sixteen values, as presented by Kröger [98KR1], of the empirical constant $a_{i,k}$, required for the calculation of F_T for such a geometry.

Table C.1: Cross-flow heat exchanger with a single tube row single pass geometry.

$a_{i,k}$	i = 1	2	3	4
k = 1	-4.62×10^{-1}	-3.13×10^{-2}	-1.74×10^{-1}	-4.20×10^{-2}
2	5.08×10^{0}	5.29×10^{-1}	1.32×10^{0}	3.47×10^{-1}
3	-1.57×10^{1}	-2.37×10^{0}	-2.93×10^{0}	-8.53×10^{-1}
4	1.72×10^{1}	3.18×10^{0}	1.99×10^{0}	6.49×10^{-1}

The water-side heat transfer coefficient, h_w, required for the calculation of the characteristic heat transfer parameter, is given by the following equation

$$h_w = \frac{Nu_w d_e}{k_w} \tag{C.10}$$

where the water-side Nusselt number is calculated by means of equation (C.11) as proposed by Gnielinski [75GN1].

$$Nu_w = \frac{(f_D/8)(Re-1000)Pr\left[1+(d_e/L)^{0.67}\right]}{1+12.7(f_D/8)^{0.5}\left(Pr^{0.67}-1\right)} \tag{C.11}$$

Equation (C.11) requires the Darcy friction factor, f_D, for the water flow inside the bundle tubes, which is calculated by means of the following equation presented by Filonenko [54FI1] for turbulent flow within smooth tubes.

$$f_D = \left(1.82 log_{10} Re_w - 1.64\right)^{-2} \tag{C.12}$$

The pressure loss characteristics of the respective evaluated finned tube bundles are presented in terms of a heat exchanger pressure loss coefficient, K_{he}, and the characteristic flow parameter, Ry, as follows:

$$K_{he} = \frac{\Delta p_t}{\frac{1}{2}\rho_m v_m^2} = a_k Ry^{b_k} \tag{C.13}$$

All physical properties are evaluated at the arithmetic mean temperature $T_m = (T_i + T_o)/2$.

C.3 Experimental procedures and test facilities

The heat transfer performance characteristics of the evaluated finned tubes are determined under idealised conditions in a windtunnel. Figure C.1 shows the schematics of the windtunnel used during this study.

The finned tubes under investigation, are assembled as a cross-flow, single pass, single row, heat exchanger test bundle shown in figure C.2, and mounted onto the inlet to the windtunnel 1. A radial fan 8 draws air uniformly through the rounded inlet section, where its wet- and dry-bulb temperature is measured, and then across the heat exchanger bundle.

The rounded inlet section ensures a uniform velocity profile before flowing across the bundle 1, which is heated by water flowing inside the tubes. A *Betz* manometer is used to measure the static pressure difference across the bundle, Δp_b, at points located in the duct wall 3. After the heat exchanger, the air passes through an insulated connection section 2 and two sets of air mixers 4.

The air discharged from the heat exchanger may have a non-uniform temperature distribution together with a non-uniform velocity distribution. To ensure accurate discharge temperature measurements, the discharge temperature measurements are taken after a set of air mixers 4. The air mixers consist of a series of vanes arranged to divide the airflow into many small streams, which are diverted across each other. The air flow rate is determined by measuring the pressure drop 3 across a selection of one or more open elliptical nozzles, Δp_n, mounted in a plate 7 located between two perforated plates 6. The perforated plates ensure that any up- or downstream flow disturbances, which may influence the airflow through the open nozzles, are eliminated. To determine the air properties upstream to the nozzles 7, the difference between the static upstream pressure and the atmospheric pressure , Δp_u, is also measured by means of a *Betz* manometer.

In this particular investigation, warm water in the order of 60°C is passed through finned the tubes of the test bundle. The design of the respective bundle manifolds, ensured that a uniform water flow distribution is maintained during each test. Since the difference between the inlet and outlet water temperature is small, the sets of thermocouples measuring the respective temperatures are readily calibrated before and after testing. The calibration of the thermocouples is done by operating the system under isothermal conditions with no airflow.

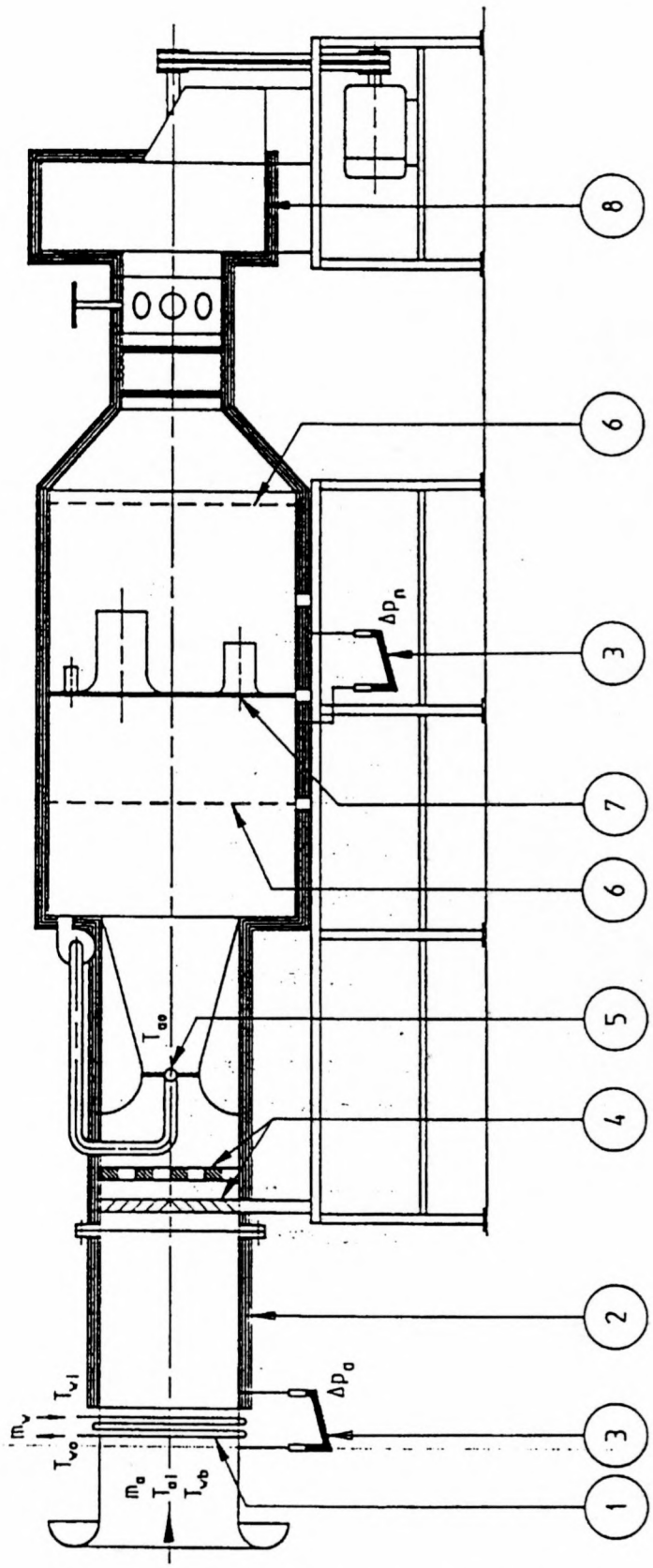

Figure C.1: Schematics of the windtunnel used for the various finned tube performance tests.

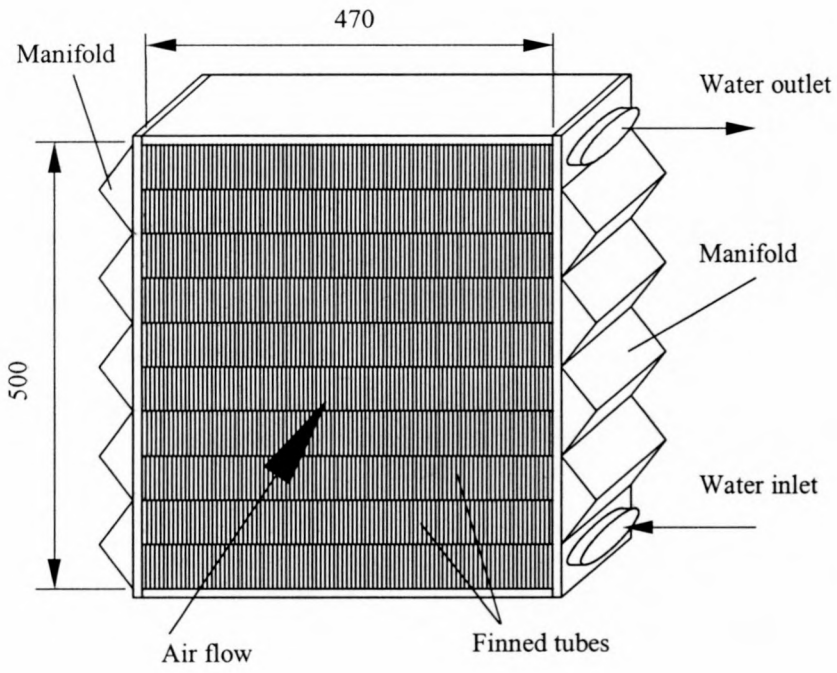

Figure C.2: Heat exchanger test bundle.

C.3.1 Windtunnel air mass flow

According to Kröger [98KR1], the air mass flow rate through an elliptical nozzle can be calculated by means of equation (C.14), given the static pressure drop across the nozzle, Δp_n, and the relevant thermophysical properties.

$$m_{an} = C_n \phi_g Y A_n \left(2 \rho_n \Delta p_n\right)^{0.5} \tag{C.14}$$

Equation (C.14) does not take into account any influences on the air mass flow, due to thermal expansion or contraction of the nozzles. The nozzle coefficient of discharge, C_n, is a function of the nozzle Reynolds number. For $30000 < Re_n < 100000$,

$$C_n = 0.954803 + 6.37817x10^{-7}\, Re_n - 4.65394x10^{-12}\, Re_n^2 + 1.33514x10^{-17}\, Re_n^3 \quad \text{(C.15a)}$$

For $100000 < Re_n < 350000$,

$$C_n = 0.9758 + 1.08x10^{-7}\, Re_n - 1.6x10^{-13}\, Re_n^2 \quad \text{(C.15b)}$$

and for $Re_n > 350000$, $C_n = 0.994$.

The nozzle Reynolds number is given by the following equation

$$Re_n = \frac{m_{an} d_n}{A_n \mu_{avn}} \quad \text{(C.16)}$$

The gas expansion factor, ϕ_g, may be approximated by the following relation:

$$\phi_g = 1 - 3\Delta p_n \left(4 p_{up} c_p / c_v\right) \quad \text{(C.17)}$$

where $c_p/c_v = 1.4$ for air and p_{up} is the upstream nozzle pressure.

For a compressible fluid, it can be shown that the approach velocity factor is approximately

$$Y = 1 + 0.5\left(A_n / A_{tus}\right)^2 + 2\left(A_n / A_{tus}\right)_2 \Delta p_n / \left(p_{up} c_p / c_v\right) \quad \text{(C.18)}$$

C.4 Sample calculation

This sample calculation shows how the air mass flow rate through the test facility is determined and illustrates the calculations required for the presentation of the heat transfer- and pressure drop performance characteristics.

The data used in the following sample calculation was recorded for a heat exchanger bundle consisting of finned tubes with a fin pitch of 2.5 mm and is presented in Table C.7. A sample calculation showing the calculation of the relevant tube geometries and a detailed cross-section drawing of the finned tubes under investigation are presented in Appendix B. All the required thermophysical properties are calculated by means of the correlations presented in Appendix F.

Heat exchanger bundle geometry:

Hydraulic tube diameter	d_e	=	0.025922 m
Inside cross-sectional tube flow area	A_{tc}	=	0.00133 m^2
Inside area of tube per unit length	A_{ti}	=	0.205242 m^2/m
Effective finned length of tubes	L_{te}	=	4.7 m
Number of tubes	n_t	=	10
Tube length	L_t	=	0.47 m
Fin width	W_f	=	0.05 m
Heat exchanger bundle frontal area	A_{fr}	=	0.235 m^2

Windtunnel specifications:

Windtunnel cross-sectional flow area	A_{tus}	=	1.44 m^2
Open nozzle 1 diameter	d_1	=	0.2509 m
Open nozzle 2 diameter	d_2	=	0.2008 m

Test data:

Inlet air temperature	T_{ai}	=	26.3323 °C
Outlet air temperature	T_{ao}	=	37.2817 °C
Mean air temperature	T_{am}	=	31.8070 °C
Inlet water temperature	T_{wi}	=	62.1798 °C
Outlet water temperature	T_{wo}	=	60.4000 °C
Mean water temperature	T_{wm}	=	61.2899 °C
Wet bulb temperature	T_{wb}	=	19 °C
Atmospheric pressure	p_{atm}	=	100131.028 N/m^2
Water mass flow rate	m_w	=	2.8962 kg/s
Pressure drop across nozzles	Δp_n	=	750 N/m^2

Nozzle upstream pressure differential	Δp_u	=	836 N/m^2
Pressure drop across the bundle	Δp_b	=	274 N/m^2

Water properties at T_{wm} = 61.2899 °C*:*

Specific heat	c_{pw}	=	4184.945295 J/kg K
Thermal conductivity	k_w	=	0.654421 W/m K
Dynamic viscosity	μ_w	=	4.541163 x 10^{-4} kg/ms
Prandtl number	Pr_w	=	2.90402

Air vapour mixture properties at T_{am} = 31.8070 °C*:*

Partial vapour pressure at T_{wb} = 19 °C	p_{vwb}	=	2196.10 N/m^2
Humidity ratio	w	=	0.0109617
Specific heat	c_{pav}	=	1016.72195 J/kg K
Thermal conductivity	k_{av}	=	0.026492 W/m K
Dynamic viscosity	μ_{av}	=	1.85796 x 10^{-5} kg/ms
Prandtl number	Pr_{av}	=	0.71305
Density	ρ_{av}	=	1.13625 kg/m^3

Air vapour mixture properties at nozzle upstream conditions:

Outlet air temperature	T_{ao}	=	37.2817 °C
Humidity ratio	w	=	0.0109617
Nozzle upstream pressure	p_{up}	=	99295.028 N/m^2
Dynamic viscosity	μ_{avn}	=	1.88284 x 10^{-5} kg/ms
Density	ρ_{avn}	=	1.106894 kg/m^3

C.4.1 Air mass flow rate through the test apparatus

A single nozzle was open during the test run and the nozzle cross-sectional flow area is calculated as follows:

$$A_{n1} = \tfrac{\pi}{4} d_{n1}^2 = \tfrac{\pi}{4}(0.2509)^2 = 0.049441 \text{ m}^2$$

- *Air mass flow rate through open nozzle 1:*

The gas expansion factor is given by equation (C.17)

$$\phi_{g1} = 1 - \frac{3x750}{4x99295.028x1.4} = 0.995954$$

and the approach velocity factor is calculated by means of equation (C.18) as

$$Y_1 = 1 + 0.5(0.049441/1.44)^2 + 2(0.049441/1.44)^2 x750/(1.4x99295.028)$$
$$= 1.00060213$$

The nozzle discharge coefficient is determined iteratively by means of equations (C.15) and (C.16), and found to be C_n = 0.994 since the nozzle Reynolds number, Re_{n1} > 350000. The air mass flow rate through nozzle 1 is now given by equation (C.14) as follows:

$$m_{a1} = 0.994x0.995954x1.00060213x0.049441x(2x1.106894x750)^{0.5}$$
$$= 1.995598 \text{ kg/s}$$

The nozzle Reynolds number is calculated by means of equation (C.16)

$$Re_{n1} = \frac{1.995598x0.2509}{0.049441x1.88284x10^{-5}} = 537864.720$$

Re_{n1} > 350000 and therefore C_n = 0.994 according to equation (C.15).

C.4.2 Heat transfer and pressure loss calculations

In order to present the heat transfer characteristics, the effective heat transfer coefficient, h_{ae} is determined by means of the right hand side of equation (C.3). The

required water-side heat transfer coefficient, h_w, logarithmic mean temperature difference, ΔT_{lm}, and the air-side heat transfer, Q_a, is determined as follows:

The water-side Reynolds number is given by the following

$$Re_w = \frac{m_w d_e}{A_{tc}\mu_w} = \frac{2.8962x0.025922}{0.00133x4.541163x10^{-4}} = 124302.059$$

and the subsequent friction factor for turbulent flow is according to equation (C.12)

$$f_D = (1.82log(124302.059) - 1.64)^{-2} = 0.0171684$$

Substituting the water-side Reynolds number and friction factor into equation (C.11) gives the water-side Nusselt number

$$Nu_w = \frac{(0.0171684/8)(124302.059-1000)x2.90402\left[1+(0.025922/4.7)^{0.67}\right]}{1+12.7(0.0171684/8)^{0.5}\left(2.90402^{0.67}-1\right)}$$

$$= 490.87704$$

The water-side heat transfer coefficient now follows from equation (C.10)

$$h_w = 490.87704x0.654421/0.025922 = 12392.5717 \text{ W/m}^2\text{K}$$

The corresponding wetted, water-side tube area is calculated as follows:

$$A_w = n_t A_{ti} L_t = 10x0.205242x0.47 = 0.964637$$

The air-side heat transfer of the test bundle is calculated by means of equation (C.5)

$$Q_a = 1.995598x1016.72195(37.2817 - 26.3323) = 22215.985 \text{ W}$$

The water-side heat transfer is calculated in similar fashion to the air-side heat transfer, in order to evaluate the energy balance of the system.

$$Q_w = 2.8962x4184.945295(62.1798 - 60.40) = 21571.957 \text{ W}$$

The subsequent energy balance is now calculated as follows:

$$EB = Q_w / Q_a = 21571.957 / 22215.985 = 0.971$$

The logarithmic mean temperature difference is given by equation (C.4)

$$\Delta T_{lm} = \frac{(60.40 - 26.3323) - (62.1798 - 37.2817)}{ln[(60.40 - 26.3323)/(62.1798 - 37.2817)]} = 29.243691 \ ^{\circ}\text{C}$$

The respective dimensionless temperatures required for the calculation of the temperature correction factor, F_T, is calculated by means of equations (C.7) to (C.9)

$$\phi_h = \frac{62.1798 - 60.40}{62.1798 - 26.3323} = 0.049649209$$

$$\phi_c = \frac{37.2817 - 26.3323}{62.1798 - 26.3323} = 0.305443894$$

$$\phi_{cf} = \frac{0.049649209 - 0.305443894}{ln[(1 - 0.305443894)/(1 - 0.049649209)]} = 0.815780498$$

Table C.1 gives the sixteen values of the empirical constant $a_{i,k}$ required for the calculation of the temperature correction factor, F_T. Substituting the required values into equation (C.6) gives the temperature correction factor $F_t = 0.97551363$.

From the right hand side of equation (C.3) it follows that the effective heat transfer coefficient,

$$h_{ae}A_a = \left(\frac{0.97551363x29.243691}{22215.985} - \frac{1}{0.964637x12392.5717}\right)^{-1} = 833.01984$$

By means of equation (C.1) the characteristic heat transfer parameter for the particular data point can now be calculated as follows:

$$Ny = \frac{833.01984}{0.235x0.71305^{0.333}0.026492} = 149755.845 \text{ m}^{-1}$$

The corresponding characteristic flow parameter is given by equation (C.2)

$$Ry = \frac{1.995598}{0.235x1.85796x10^{-5}} = 457055.393 \text{ m}^{-1}$$

The inlet air velocity is calculated as follows

$$v_{ai} = m_a / (\rho_{av} A_{fr}) = 1.995598 / (1.13625x0.235) = 7.47362498 \text{ m/s}$$

Equation (C.13) gives the non-isothermal pressure loss coefficient to be

$$K_{he} = \frac{274}{\frac{1}{2}1.13625x7.47362498^2} = 8.634637$$

The heat transfer and pressure drop results may by correlated by means of the least squares method [94GE1] and presented in exponential form as given by equations (C.1) and (C.13) respectively.

$$Ny = 1707.3978 Ry^{0.344111}$$

$$K_{heiso} = 1168.125 Ry^{-0.378090}$$

C.5 *Experimental data*

In co-operation with Makhema [99MA1], the following experimental test data was obtained.

Table C.2: Air- and waterside temperatures, mass flow rates and energy balance for a test conducted on the 2.2 mm fin pitch tube bundle.

No.	p_{atm} °C	T_{ai} °C	T_{ao} °C	T_{wi} °C	T_{wo} °C	m_a kg/s	m_w kg/s	Energy balance, %
1	100273	24.9695	36.5022	64.4204	62.1421	2.4791	2.9440	4.0253
2	100265	25.4213	38.3388	64.3172	62.2621	1.9704	2.9244	3.3919
3	100266	25.4095	40.2657	64.2602	62.4009	1.5576	2.9167	4.1324
4	100265	25.4322	43.0686	64.3021	62.6867	1.1342	2.9078	3.9390
5	100265	25.4544	45.2657	64.4102	62.9669	0.8840	2.8725	3.1658
6	100259	25.7829	48.9238	64.8531	63.6397	0.6466	2.8640	4.9833

Table C.3: Air- and waterside temperatures, mass flow rates and energy balance for a test conducted on the 2.3 mm fin pitch tube bundle.

No.	p_{atm} °C	T_{ai} °C	T_{ao} °C	T_{wi} °C	T_{wo} °C	m_a kg/s	m_w kg/s	Energy balance, %
1	99844	28.6901	38.3076	61.9731	59.9847	2.4656	2.8423	2.9955
2	99841	28.8805	39.5237	61.6023	59.7481	1.9671	2.7858	-0.4081
3	99842	28.7949	41.0572	61.8017	60.1763	1.5365	2.7870	2.1478
4	99845	28.6381	43.0477	61.9922	60.5707	1.1483	2.7790	2.8465
5	99844	28.6500	44.9530	61.9628	60.6975	0.8958	2.7608	2.6642
6	99847	28.5132	47.2141	61.7606	60.6762	0.6637	2.7633	1.7663

Table C.4: Air- and waterside temperatures, mass flow rates and energy balance for a test conducted on the 2.4 mm fin pitch tube bundle.

No.	p_{atm} °C	T_{ai} °C	T_{ao} °C	T_{wi} °C	T_{wo} °C	m_a kg/s	m_w kg/s	Energy balance, %
1	99657	30.9757	39.2506	61.4688	59.5709	2.4583	2.7189	-3.0513
2	99657	31.0151	40.5375	61.6476	59.9534	1.9650	2.7168	0.0683
3	99656	31.0331	42.0278	61.7585	60.2781	1.5352	2.6604	5.2050
4	99662	30.6762	43.9341	61.9265	60.6132	1.1336	2.6762	5.0113
5	99660	30.8281	45.9278	61.9828	60.8458	0.8666	2.6662	5.9052
6	99662	30.7082	48.2942	62.2364	61.2450	0.6419	2.6331	6.0717

Table C.5: Air- and waterside temperatures, mass flow rates and energy balance for a test conducted on the 2.5 mm fin pitch tube bundle.

No.	p_{atm} °C	T_{ai} °C	T_{ao} °C	T_{wi} °C	T_{wo} °C	m_a kg/s	m_w kg/s	Energy balance, %
1	100141	25.7392	35.5305	62.0382	60.0484	2.5269	2.8979	4.0892
2	100131	26.3323	37.2817	62.1798	60.4000	1.9956	2.8962	2.8995
3	100130	26.3878	39.0992	62.2043	60.6221	1.5463	2.8816	4.5262
4	100129	26.4842	41.3760	62.0889	60.7237	1.1461	2.8724	5.4333
5	100118	27.1069	44.0803	62.2516	61.0730	0.8722	2.8773	5.6985
6	100120	27.0320	46.3389	62.2193	61.1917	0.6563	2.8773	3.9549

C.6 *Performance characteristics of the evaluated finned tube bundles*

Tables C.2 to C.5 give the experimental data acquired during respective bundle tests. Figures C.3 and C.4 show the heat transfer results, in terms of the characteristic heat transfer and flow parameters, obtained from the various evaluated tube bundles. The relation between the fin pitch and the heat transfer of the evaluated finned tube bundles is evident. As is expected, the tube bundle with P_f = 2.2 mm has the highest heat transfer performance characteristics and the tube bundle with P_f = 2.5 mm the lowest. It should however be stated that the fin pitch is not the only determining factor in the heat transfer of the finned tubes. Other factors such as fin thickness, the galvanising thickness on the steel fins and a difference in contact resistance also has an influence on the heat transfer performance characteristics. The investigation of the various influences on the heat transfer of the evaluated finned tubes however does not form part of this dissertation.

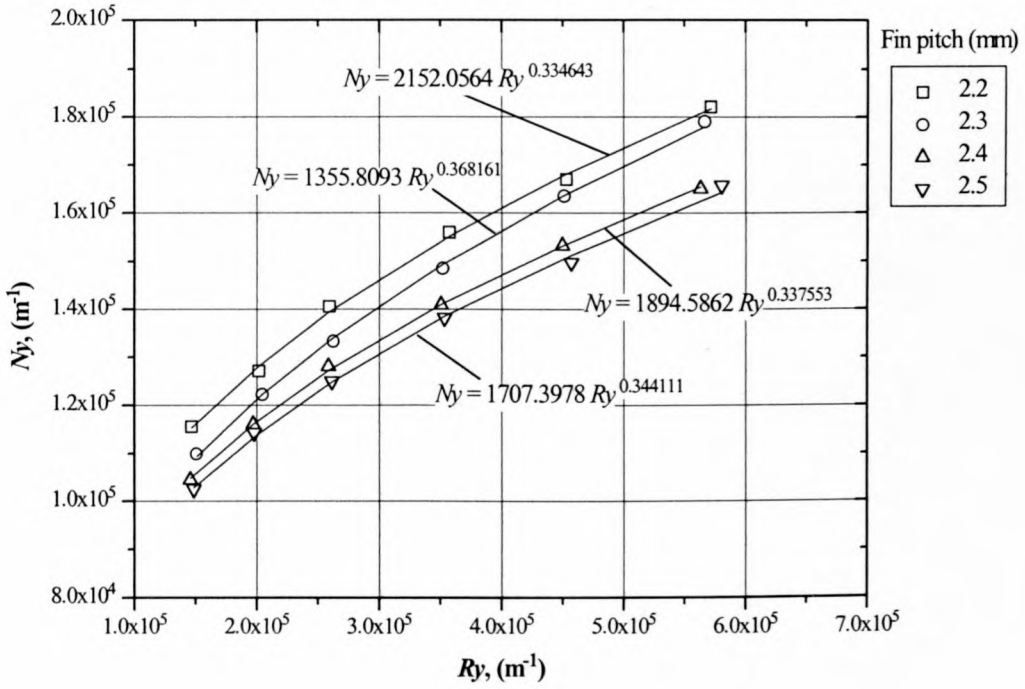

Figure C.3: Heat transfer results of the various tubes evaluated in terms of the characteristic heat and flow parameters.

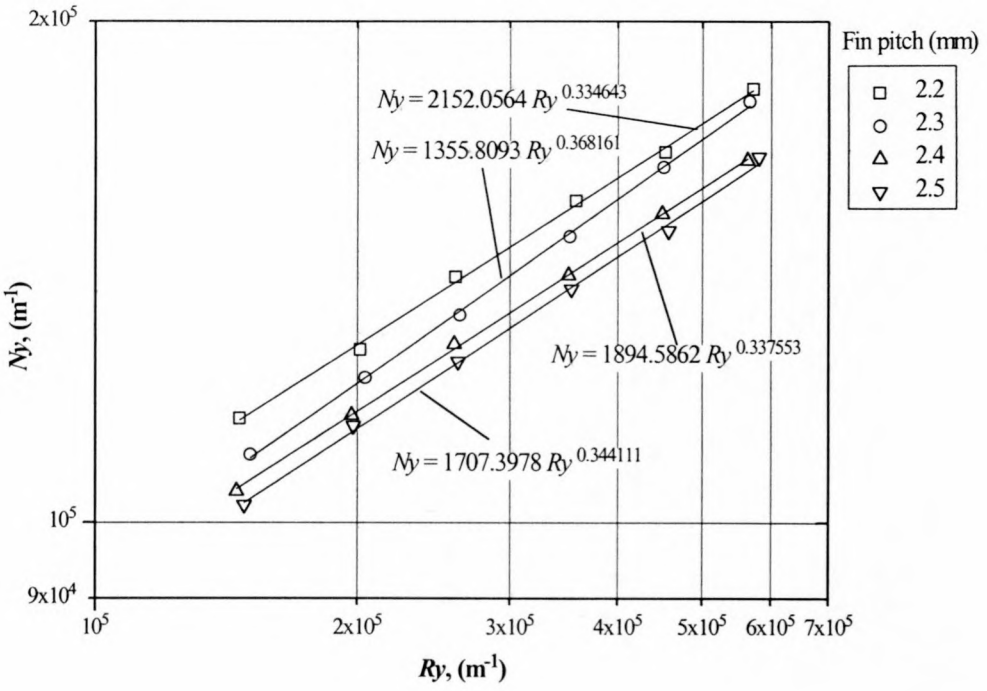

Figure C.4: Correlated heat transfer results in terms of the characteristic heat transfer and flow parameters.

Table C.6 gives a summary of the correlated heat transfer performance characteristics, in terms of the characteristic heat transfer and flow parameters as defined by equation (C.1). The correlated coefficients a_{Ny}, and exponents, b_{Ny}, for each heat exchanger bundle are given.

Table C.6: Summary of the correlated characteristic heat transfer parameter for each evaluated tube bundle, as given by equation (C.1)

P_f, (mm)	a_{Ny}	b_{Ny}
2.2	2152.0564	0.334643
2.3	1355.8093	0.368161
2.4	1894.5862	0.337553
2.5	1707.3978	0.344111

Figure C.5 shows the isothermal, pressure loss results in terms of the isothermal, pressure loss coefficient and characteristic flow parameter. The heat exchanger bundle consisting of tubes with P_f = 2.2 mm has the highest pressure loss coefficient, while the bundle with P_f = 2.5 mm has the lowest.

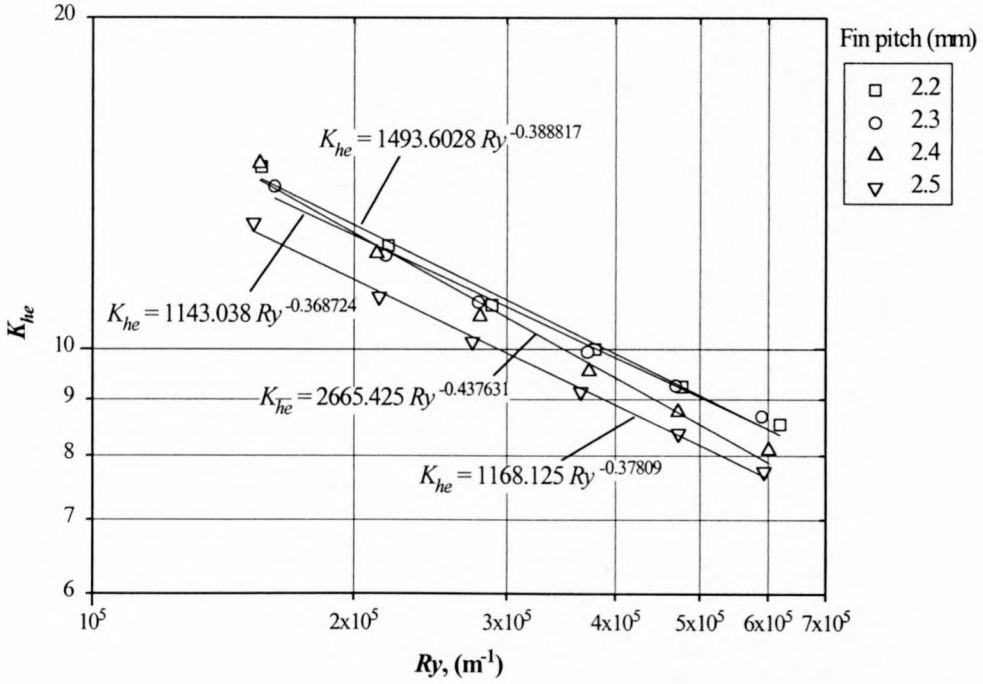

Figure C.5: Isothermal pressure loss results presented in terms of the pressure loss coefficient and the characteristic flow parameter.

Table C.7 Summary of the correlated isothermal pressure loss coefficient for each of the evaluated finned tube bundles, as given by equation (C.13)

P_f, (mm)	a_k	B_k
2.2	1493.6028	-0.388817
2.3	1143.038	-0.368724
2.4	2665.425	-0.437631
2.5	1168.125	-0.378090

Table C.7 gives a summary of the correlated isothermal pressure loss coefficients in terms of the characteristic flow parameters as defined by equation (C.13). The

correlated coefficients a_k, and exponents, b_k, for each of the evaluated finned tube bundles are given.

C.7 Tube row heat transfer matching

Conradie [91CO1] developed a computer simulation program with which the performance characteristics of forced draught air-cooled heat exchangers can be critically evaluated. With the aid of this program, the operation of a particular double row, forced draught ACC system with second tube row heat transfer characteristics similar to the evaluated finned tubes, is simulated. The aim of this investigation is to illustrate the matching heat transfer capabilities of the 1st and 2nd tube row for the particular ACC system operating at an atmospheric design temperature of 25 °C.

The input specifications of the particular condenser system, utilising the finned tubes with 2.2 mm fin pitch as its second tube row bundle is as follows:

Fan installation specifications:

Height of fan platform above ground level	= 40 m
Number of fan units	= 1
Fan diameter	= 9.145 m
Fan casing diameter	= 9.216 m
Fan hub diameter	= 1.4 m
Fan speed	= 125 r.p.m
Loss coefficient for flow obstacles (fan suction side)	= 0.2969
Loss coefficient for flow obstacles (fan discharge side)	= 0.3908
Fan blade angle	= 16 °
Efficiency of fan drive system	= 90 %
Half-width of walkway between A-frames	= 0.2 m
Condenser support loss coefficient	= 1.5
Height of wind wall	= 8.27 m

Heat exchanger bundle specifications:

Number of heat exchanger bundles above one fan	= 8
Frontal area of one bundle	= 27.434 m^2
Effective finned tube length	= 9.46 m
Heat exchanger bundle semi-apex angle	= 30 ^{o}
Heat exchanger inlet contraction area ratio	= 0.875
Minimum heat exchanger free flow area	= 0.48
Number of tube rows	= 2
Number of tubes in 1st row	= 57
Number of tubes in 2nd row	= 58
Isothermal pressure loss coefficient across two tube rows	$K_{he} = 4464.4\ Ry^{-0.4393}$
Characteristic heat transfer parameter (1st row)	$Ny = 475.8214\ Ry^{0.4031}$
(2nd row)	$Ny = 2152.056\ Ry^{0.3346}$

Finned tube design specifications:

Tube hydraulic diameter (1st row)	= 0.02593 m
(2nd row)	= 0.02593 m
Tube cross-sectional flow area (1st row)	= 0.00133 m^2
(2nd row)	= 0.00133 m^2
Tube inside area per meter length (1st row)	= 0.20524 m^2/m
(2nd row)	= 0.20524 m^2/m

Atmospheric and steam design specifications:

Air temperature at ground level	= 25 ^{o}C
Barometric pressure at ground level	= 84600 N/m^2
Saturated steam supply temperature	= 60 ^{o}C
Effective steam header diameter	= 1.25 m
Mean steam ducting loss coefficient	= 2.5

By entering the heat transfer characteristics of the different evaluated finned tubes as input values for the second tube row to the computer program, a set of performance data is generated. Figure C.6 shows the respective tube row heat transfer results versus the

fin pitch of the second tube row, P_{f2}, for a single fan unit. The matching heat transfer of the first and second tube rows is evident in the case where the second tube row heat transfer characteristics compares to that of the evaluated finned tube with $P_f = 2.2$ mm.

An increase P_{f2}, results in a decrease in the heat transfer of the second tube row, as shown in figure C.6. The higher heat transfer of the first tube row may result in steam back flow, which in turn may cause the accumulation of non-condensable gases in the first tube row.

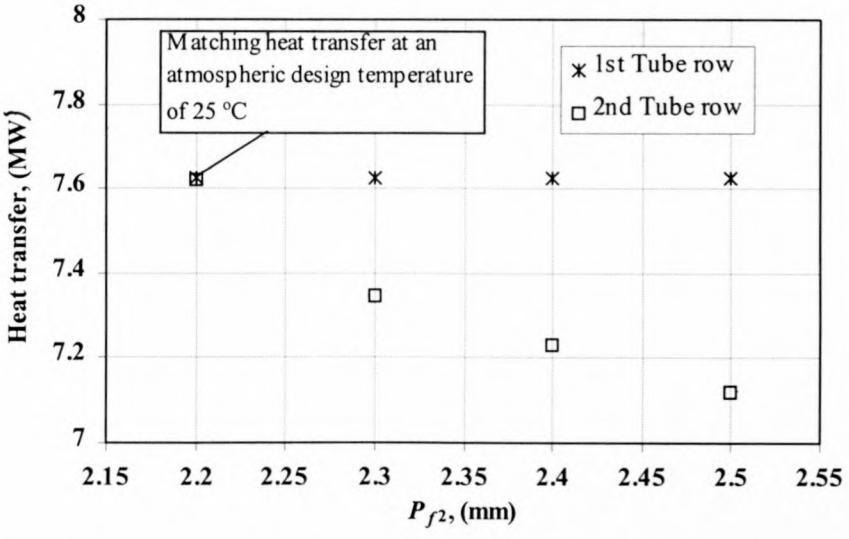

Figure C.6: Heat transfer results of a single fan unit operating at an atmospheric temperature of 25 °C and a saturated steam supply temperature of 60 °C.

Matching heat transfer of the two tube rows is only valid for the specified design operating condition. To illustrate the influence of different atmospheric operating temperatures on the performance of the ACC system, temperatures of 15 °C and 35 °C are simulated. These results are presented in figures C.7 and C.8 respectively.

Figure C.7 shows that atmospheric temperatures below the design operating point of the system, (T_{atm} = 15 °C), result in higher heat transfer for both tube rows. This is expected as the temperature difference between the colder atmospheric temperature and saturated steam supply is now greater. For the case where P_{f2} = 2.2 mm, the second tube row has the higher heat transfer. This operating condition may result in steam

backflow that causes the accumulation of non-condensable gases in the second tube row.

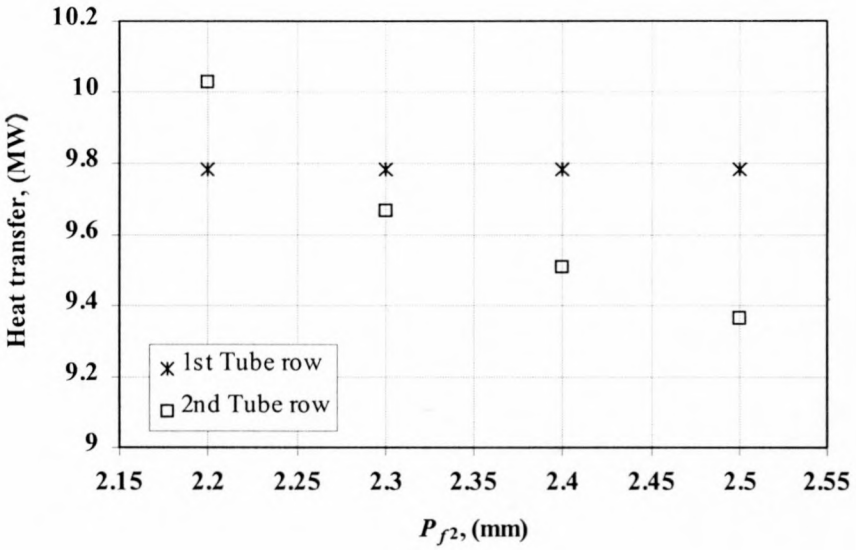

Figure C.7: Tube row heat transfer results vs P_{f2} for a single fan unit operating at an atmospheric temperature of 15 °C and a saturated steam supply temperature of 60 °C.

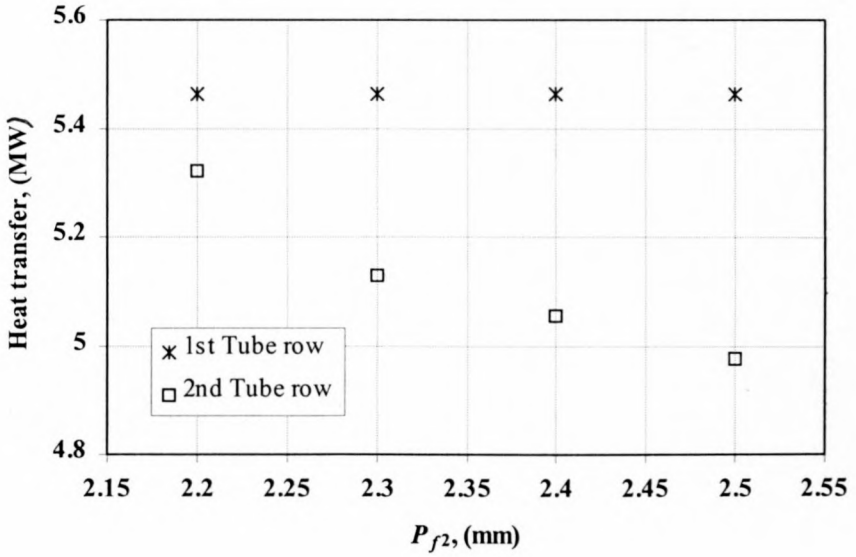

Figure C.8: Tube row heat transfer results vs P_{f2} for a single fan unit operating at an atmospheric temperature of 35 °C and a saturated steam supply temperature of 60 °C.

On the other hand, figure C.8 shows that atmospheric temperatures higher than the design operating point, (T_{atm} = 35 °C) result in a decrease in the heat transfer of both tube rows. For this operating condition, and P_{f2} = 2.2 mm, the first tube row has the

higher heat transfer. Steam backflow may occur resulting in the accumulation of non-condensable gases in the first tube row.

Figures C.6 to C.8 show the importance of matching heat transfer capabilities in double row ACC systems and care should be taken in the design of such systems to ensure tube row matching at the design operation point.

APPENDIX D

PERFORMANCE CHARACTERISTICS OF AN AIR-COOLED FINNED TUBE OPERATING AT SMALL ANGLES TO THE HORIZONTAL

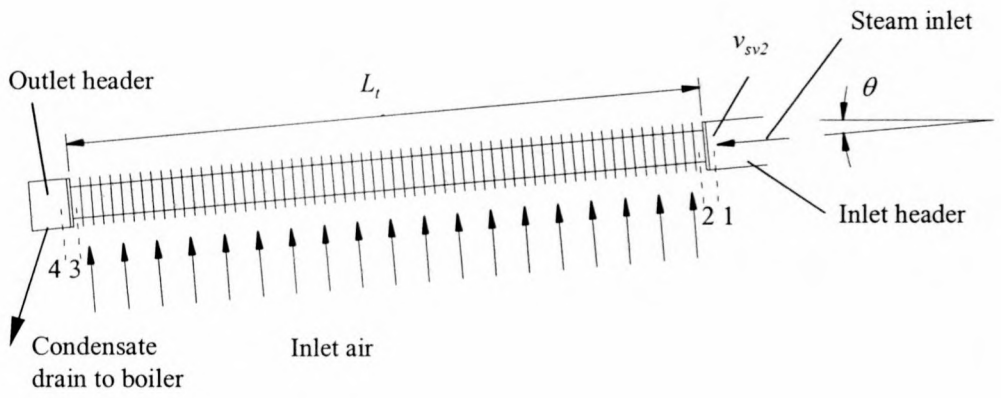

Figure D.1: A schematic of the test tube.

D.1 Sample calculations

Figures D.1 and 5.2 are schematics of the test tube and the experimental apparatus respectively, used to determine the heat transfer characteristics of a typical finned tube operating at small inclination angles. Tables D.1 to D.10 give the experimental data for all the evaluated operating conditions.

The test data used in the following sample calculation was recorded for a steam saturation temperature of approximately 60 °C and a tube inclination angle of –5 °. All thermopysical properties are determined by means of the relevant correlations presented in Appendix F

Test tube geometry:

Hydraulic tube diameter	d_e	=	0.02592 m
Inside tube height	H_{ti}	=	0.097 m
Frontal tube area	A_{fr}	=	0.3491 m^2

Inside tube cross-sectional flow area	A_{tc}	=	0.00133 m^2
Inlet header cross-sectional flow area	A_{ihc}	=	0.012469 m^2
Inside wetted tube area per unit length	A_{ti}	=	0.20524 m^2/m
Effective finned length of tube	L_t	=	6.982 m
Tube inclination angle	θ_t	=	-5 °
Fin width	W_f	=	0.05 m

Steamside and condensate data:

Inlet steam temperature	T_{vi}	=	60.08 °C
Outlet steam temperature	T_{vo}	=	59.1 °C
Arithmetic mean steam temperature	T_{vm}	=	59.59 °C
Condensate mass flow rate	m_c	=	0.0094 kg/s

Steam and condensate properties evaluated at T_{vi}:

Vapour density	ρ_v	=	0.13068 kg/m^3
Vapour viscosity	μ_v	=	$11.08509x10^{-6}$ kg/ms
Condensate density	ρ_c	=	983.17474 kg/m^3
Condensate viscosity	μ_c	=	$4.62537x10^{-4}$ kg/ms
Condensate thermal conductivity	k_c	=	0.65327 W/mK
Latent heat of vaporisation	i_{lg}	=	$2.35842x10^6$ J/kg

Airside data at air-box 1:

Inlet air temperature	T_{ai1}	=	25.45 °C
Outlet air temperature	T_{ao1}	=	43.49 °C
Arithmetic mean air temperature	T_{am1}	=	34.47 °C
Air mass flow rate	m_{a1}	=	0.317 kg/s

Air properties at T_{am}:

Specific heat	c_{pam1}	=	1007.2639 J/kgK

Schoenfeld [97SC1] experimentally determined the air-side heat transfer characteristics of the finned tube in a wind tunnel, prior to the installation of the test tube in the experimental apparatus. Appendix C shows the schematics of the wind tunnel and gives

a discussion on the experimental procedure by which the heat transfer characteristics were determined. Equation (D.1) gives the airside heat transfer characteristics of the test tube in terms of the characteristic flow parameter.

$$Ny = 2594.951 Ry^{0.3184} \tag{D.1}$$

D.1.1 Experimental heat transfer

The heat transfer to the air in air-box 1 (refer to the schematic of the experimental apparatus presented in figure 5.2) is given by the following equation.

$$Q_{a1} = m_{a1} c_{pam1} (T_{ao1} - T_{ai1}) = 0.317 x 1007.2639 x (43.49 - 25.45) = 5760.2199 \text{ W}$$

Similarly, the experimental heat transfer to the air is calculated for the remaining three air-boxes. Summation of the heat transfer in the four air-boxes gives a total airside heat transfer of Q_{at} = 22664.24 W. In order to evaluate an energy balance, the heat transfer on the steam side is obtained from the measured condensate mass flow rate as follows:

$$Q_c = m_c i_{lg} = 0.0094 x 2.35842 x 10^6 = 22169.148 \text{ W}$$

The energy balance is defined as

$$EB = (Q_c - Q_{at}) / Q_c x 100 = (22169.148 - 22664.24) / 22169.148 x 100 = -2.233 \text{ \%}$$

D.1.2 Predicted heat transfer

The evaluation of the air properties at the mean air temperature requires the air outlet temperature, which is an unknown in the set of heat transfer equations presented in equation (5.14). The heat transfer equations, and subsequent air outlet temperature are therefore solved by an iterative procedure. This sample calculation shows the final set of calculations used in the iterative procedure to determine the airside heat transfer in

air-box 1. The outlet air temperature is found to be $T_{ao1} = 44.0208\ ^{o}C = 317.1708$ K and the arithmetic mean air temperature is thus

$$T_{am1} = (T_{ai1} + T_{ao1})/2 = (25.45 + 44.0208)/2 = 34.7354\ ^{o}C$$

Air properties at T_{am1} are as follows:

Specific heat	c_{pam1} =	1007.2639 J/kgK
Viscosity	μ_{am1} =	$1.88299x10^{-5}$ kg/ms
Density	ρ_{am1} =	1.13519 kg/m^3
Thermal conductivity	k_{am1} =	0.02683 W/mK
Prandtl number	Pr_{am1} =	0.7069

The finned tube length in air-box1 is

$$L_{t1} = L_t / 4 = 6.982 / 4 = 1.7455 \text{ m}$$

and the corresponding finned tube frontal area

$$A_{fr1} = L_{t1} x W_f = 1.7455x0.05 = 0.087275 \text{ m}^2$$

According equation (A.19) the characteristic flow parameter, *Ry*, is

$$Ry_1 = 0.317 / (1.88299x10^{-5} x0.087275) = 192895.187 \text{ m}^{-1}$$

Substituting Ry_1 into equation (D.1) gives

$$Ny_1 = 2594.951 Ry_1^{0.3184} = 2594.951x192895.187^{0.3184} = 125018.848 \text{ m}^{-1}$$

The air-side thermal conductance calculated by means of equation (A.18) is as follows:

$$(h_{ae}A_a)_1 = Ny_1 k_{am1} Pr_{am1}^{0.333} A_{fr1} = 125018.848x0.02683x0.7069^{0.333} x0.087275$$
$$= 260.8088 \text{ W/K}$$

The overall heat transfer coefficient, based on the condensation surface area, which is required to determine the condensation heat transfer coefficient is calculated by means of equation (A.22)

$$(U_c H_t L_t) = 260.8088/2 = 130.4044 \text{ W/K}$$

The air mass flow rate across one half of the finned tube is required in order to determine the condensation heat transfer coefficient, h_c, and is calculated as follows:

$$m_{ah1} = m_{a1}/2 = 0.317/2 = 0.01585 \text{ kg/s}$$

The condensation heat transfer coefficient is now determined by means of equation (A.20).

$$h_{c1} = 0.9245\left[\frac{1.7455x0.65327^3 x983.17474^2 x9.792x\cos(-5)x2.35842x10^6}{4.62537x10^{-4} x0.1585x1007.2639x(59.59-25.45)}\right.$$
$$\left.\frac{1}{x[1-exp\{-130.4044/(0.1585x1007.2639)\}]}\right]^{0.333}$$
$$= 18068.8251 \text{ W/m}^2\text{K}$$

The steamside area of section 1 of the finned tube is

$$A_{c1} = A_{ti} L_{t1} = 0.20524x1.7455 = 0.35825 \text{ m}^2$$

The overall thermal conduction is obtained from equation (A.16).

$$(UA)_1 = \left[\frac{1}{260.8088} + \frac{1}{18068.8251x0.35825}\right]^{-1}$$
$$= 250.7076 \text{ W/K}$$

and the corresponding condenser effectiveness is calculated by means of equation (A.15).

$$e_1 = 1 - exp[-250.7076/(0.317x1007.2639)] = 0.54396$$

The predicted airside heat transfer of air-box 1 can now be obtained by means of equation (5.14) as follows:

$$Q_{a1} = m_{a1}c_{pam1}(T_{vm1} - T_{ai1})e = 0.317x1007.2639x(59.59 - 25.45)x0.54396$$
$$= 5929.704 \text{ W}$$

From equation (5.14) it is now possible to determine the predicted air outlet temperature, T_{ao1}, for air box 1.

$$T_{ao1} = Q_{a1}/(m_{a1}c_{pam1}) + T_{ai1} = 5929.704/(0.317x1007.2639) + 25.45 = 44.0208\ ^{\circ}\text{C}$$

The comparison between the experimental and predicted heat transfer is shown in figure D.2

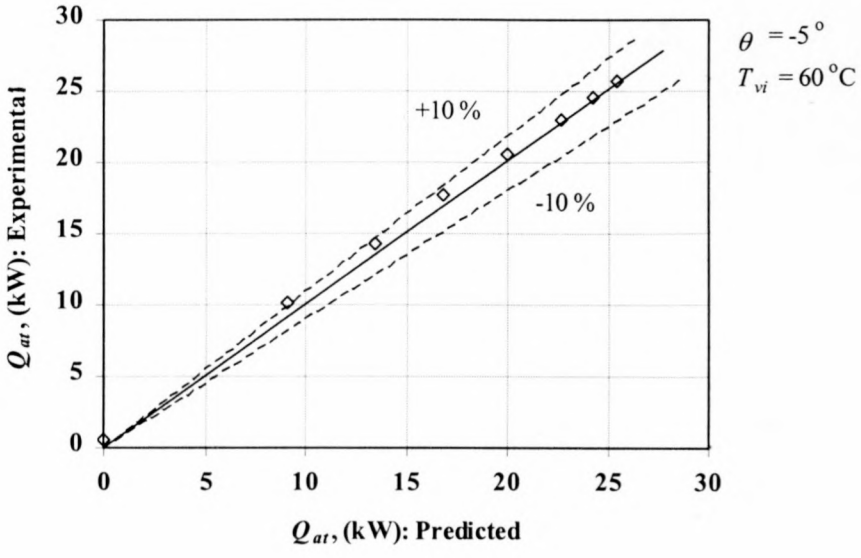

Figure D.2: Comparison between the experimental and predicted heat transfer rate.

D.1.3 Predicted pressure drop in the absence of draining condensate at the inlet to the test tube

For negative tube inclination angles, there is no condensate drainage at the steam inlet to the finned tube and the inlet pressure drop is evaluated in terms of a single phase contraction loss coefficient as shown in the following sample calculation. The experimental airside heat transfer is used in order to determine the respective vapour and condensate flow rates. The superficial vapour velocity at the tube inlet is given by the following relation

$$v_{sv2} = Q_{at} / \left(\rho_v A_{tc} i_{lg}\right) = 22664.24 / \left(0.13068x0.00133x2.35842x10^6\right)$$
$$= 55.2916\,\text{m/s}$$

and the corresponding densimetric Froude number according to equation (A.50) is

$$Fr_{Hsg2} = 0.13068x55.2916^2 / \left[9.792x0.097x\left(983.17474 - 0.13068\right)\right]$$
$$= 0.42787$$

The condensate mass flow rate based on the airside heat transfer is calculated as follows

$$m_{ca} = Q_{at} / i_{lg} = 22664.24 / 2.35842x10^6 = 0.00961\,\text{kg/s}$$

The inlet to the finned tube is approximated as a sharp inlet to parallel plates and the required single phase contraction loss coefficient, K_{csp}, is determined by means of equation (5.3) as follows:

$$\sigma_{21} = A_{tc} / A_{ihc} = 0.00133 / 0.012469 = 0.1066645$$

which gives σ_c from equation (5.4) as

$$\sigma_c = 0.6144517 + 0.04566493x0.1066645 - 0.336651x0.1066645^2 + 0.4082743 x0.1066645^3 + 2.672041x0.1066645^4 - 5.963169x0.1066645^5 + 3.558944 x0.1066645^6 = 0.6162566$$

Substituting σ_c into equation (5.3) gives

$$K_{csp} = (1 - 1/0.6162566)^2 = 0.3877561$$

It is now possible to determine the inlet pressure drop, in the absence of draining condensate, to the finned tube by means of equation (5.2)

$$\Delta p_{12} = 0.5x0.13068x55.2916^2\left[1 - 0.1066645^2 + 0.3877562\right] = 274.9384 \text{ N/m}^2$$

The vapour Reynolds number at the inlet to the finned tube is calculated as follows

$$Re_{sv2} = \rho_v v_{sv2} d_e / \mu_v = 0.13068x55.2916x0.02592 / 11.08509x10^{-6} = 16895.2280$$

Using the condensate mass flow based on the airside heat transfer, the suction Reynolds number is determined according to equation (A.38)

$$Re_{vn} = m_{ca} d_e / (\mu_v L_t A_{ti}) = 0.00961x0.02592 / (11.08509x10^{-6} x6.982x0.20524) = 15.68113$$

The coefficients a_1 and a_2 are given by equations (A.37a) and (A.37b) respectively.

$$a_1 = 1.0649 + 1.041x10^{-3} x15.68113 - 2.011x10^{-7} x15.68113^3 = 1.080449$$

$$a_2 = 290.1479 + 59.3153x15.68113 + 1.5995x10^{-2} x15.68113^3 = 1281.95485$$

It is assumed that all the steam is condensed inside the test tube section, rendering the outlet vapour velocity, $v_{sv3} = 0$. Equation (5.8) gives the pressure drop across the finned tube due to the respective frictional, gravitational and momentum components assuming no vapour outflow at the outlet of the test tube. The finned tube pressure loss due to frictional losses is determined by means of the first term on the right-hand side of equation (5.8).

$$\Delta p_{23f} = \tfrac{1}{2}\rho_v v_{sv2}^2 \left[\frac{L_t}{d_e} K\, Re_{sv2}^n \left(\frac{a_1}{n+3} + \frac{a_2}{(n+2)Re_{sv2}}\right)\right]$$

$$= 0.5x0.13068x55.2916^2\left[\frac{6.982}{0.02592} x0.2259x1685.228^{-0.2088}\right.$$

$$\left. x\left(\frac{1.080449}{3-0.2088} + \frac{1281.95485}{(2-0.2088)16895.228}\right)\right] = 683.7795\ \text{N/m}^2$$

The second term on the right-hand side of equation (5.8) gives the gravitational pressure drop through the test tube as follows:

$$\Delta p_{23g} = \rho_v g L_t \sin\theta_t = 0.13068x9.792x6.982x\sin(-5) = -0.7787\ \text{N/m}^2$$

and the gain in pressure due to the decrease in vapour momentum according to the last term on the right hand side of equation (5.8) is

$$\Delta p_{23m} = -\rho_v v_{sv2}^2 = -0.13068x55.2916^2 = -399.5098\ \text{N/m}^2.$$

The sum of the frictional, gravitational and momentum components, as shown in equation (5.6), gives the total pressure drop between sections 2 and 3 of the finned tube.

$$\Delta p_{23} = 683.7795 - 0.7787 - 399.5098 = 283.4910\ \text{N/m}^2$$

Due to the assumption of no vapour outflow at the end of the finned tube $\Delta p_{34} = 0$. The total predicted pressure drop can now be calculated by summation of the respective pressure drop components as given by equation (5.1).

$$\Delta p_{14} = 274.9384 + 283.4910 + 0 = 558.4294 \text{ N/m}^2$$

Figure D.3 shows the comparison between the experimental results and the predicted pressure drop.

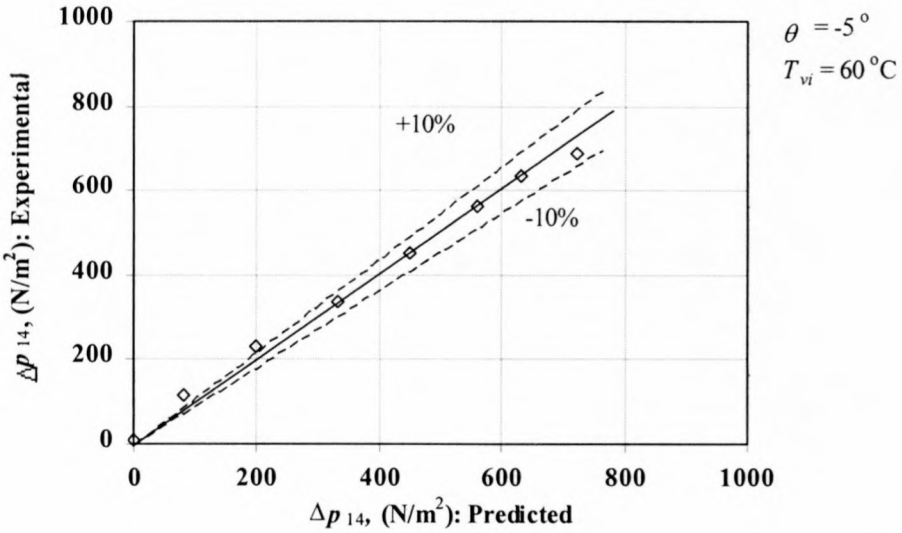

Figure D.3: Comparison between the experimental and predicted pressure drop results.

D.1.4 Predicted pressure drop and tube flooding in the presence of draining condensate at the inlet to the test tube

For positive tube inclination angles, condensate drainage is present at the inlet to the finned tube and the inlet pressure drop, Δp_{12}, is evaluated in terms of a two-phase contraction loss coefficient as presented in equation (5.5). The following data set was recorded for a tube inclination angle of 2 ° and a steam inlet temperature to the test tube of approximately 60 °C. All thermopysical properties are determined by means of the correlations presented in Appendix F.

Experimental data:

Total airside heat transfer	Q_{at}	=	6730.7884 W
Inlet steam temperature	T_{vi}	=	60.16 °C

Fluid properties evaluated at T_{vi}:

Vapour density	ρ_v	=	0.131139 kg/m^3
Vapour viscosity	μ_v	=	$1.108764x10^{-5}$ kg/ms
Condensate density	ρ_c	=	983.132585 kg/m^3
Condensate viscosity	μ_c	=	$4.619725x10^{-4}$ kg/ms
Latent heat of vaporisation	i_{lg}	=	$2.358228x10^6$ J/kg

In similar fashion to the previous sample calculation, the pressure loss across the test tube is calculated with exception of the inlet pressure drop. The experimental airside heat transfer is used in order to determine the respective vapour and condensate flow rates.

The superficial vapour velocity at the duct inlet is as follows:

$$v_{sv2} = Q_{at} / (\rho_v A_{tc} i_{lg}) = 6730.7884 / (0.131139x0.00133x2.358228x10^6$$
$$= 16.36427 \text{ m/s}$$

and the corresponding densimetric Froude number according to equation (A.50) is

$$Fr_{Hsg2} = 0.131139x16.36427^2 / [9.792x0.097x(983.132585 - 0.131139)]$$
$$= 0.037612$$

The condensate mass flow based on the airside heat transfer is calculated as follows:

$$m_{ca} = Q_a / i_{lg} = 6730.7884 / 2.358228x10^6 = 2.854172x10^{-3} \text{kg/s}$$

The inlet to the finned tube is approximated as a square-edged inlet to parallel plates. Zapke [97ZA1] determined the two-phase inlet loss coefficient in the presence of draining liquid at the inlet to a flattened tube with tube height, H_t = 100mm, operating at a tube inclination angle of 2°, as K_{tp} = 1.9. Substituting the values for K_{tp} and σ_{21} into equation (5.5) gives the inlet pressure loss to the test tube as

$$\Delta p_{12} = 0.5x0.131139x16.36427^2\left(1.9 - 0.1066645^2\right) = 33.16197 \text{ N/m}^2$$

The pressure loss across the test tube due to frictional and gravitational losses are respectively found to be

$$\Delta p_{23f} = 80.47658 \text{ N/m}^2$$

and

$$\Delta p_{23g} = 0.3129 \text{ N/m}^2$$

by means of equation (5.8) and assuming $v_{sv3} = 0$. The gain in pressure through the tube due to the decrease in vapour momentum is given by the last term on the right-hand side of equation (5.8) as follows

$$\Delta p_{23m} = -35.11763 \text{ N/m}^2$$

The sum of the frictional, gravitational and momentum components, as shown in equation (5.6), gives the total pressure drop between sections 2 and 3 of the finned tube.

$$\Delta p_{23} = 80.47658 + 0.3129 - 35.11763 = 45.67185 \text{ N/m}^2$$

The total predicted pressure drop can now be calculated by summation of the respective pressure drop components as given by equation (5.1).

$$\Delta p_{14} = 33.16197 + 45.67185 = 78.83382 \text{ N/m}^2$$

The following calculations, illustrates the prediction of the densimetric gas Froude number at which flooding in the inclined test tube occurs. Equation (A.52) gives the water surface tension as presented by Carey [92CA1] as follows

$$\sigma = 75.83 - 0.1477x60.16 = 0.0669444 \text{ N/m}$$

For a tube inclination angle, $\theta = 2\ ^{\circ}$, the empirical constants K_o and n, as correlated by Zapke [97ZA1], are respectively given by equations (A.54) and (A.55)

$$K_o = 7.9143x10^{-2} + 4.9705x10^{-3}x2 + 1.5183x10^{-4}x2^2 - 1.9852x10^{-6}x2^3$$
$$= 0.08967544$$

$$n = 1.8149x10 - 1.9471x2 + 6.7058x10^{-2}x2 + 1.5183x10^{-4}x2^3$$
$$= 14.51877$$

In order to calculate the densimetric liquid Froude number, Fr_{dsl}, the superficial liquid velocity at the inlet to the tube is determined as follows

$$v_{sl2} = m_{ca}/(\rho_l A_{tc}) = 2.854172x10^{-3}/(983.132585x0.00133) = 2.18281x10^{-3}\ \text{m/s}$$

Substituting the superficial liquid velocity into equation (A.56) gives

$$Fr_{dsl} = 983.132585\left(2.18281x10^{-3}\right)^2/[9.792x0.02592(983.132585 - 0.131139)]$$
$$= 1.877515x10^{-5}$$

The *Zk*-number which accounts for the relevant fluid properties and duct dimension that govern the flooding of inclined tubes, is according to equation (A.51)

$$Zk_d = (983.132585x0.02592x0.0669444)^{0.5}/4.619725x10^{-4} = 2827.25217$$

The densimetric gas Froude number at which the onset of flooding is prediction is now calculated by means of equation (A.53) as follows

$$Fr_{Hsg} = 0.08967544\,exp\left[-14.51877\left(1.877515x10^{-5}\right)^{0.6}/2827.25217^{0.2}\right]$$
$$= 0.089289$$

Figure D.4 shows the results of the evaluated test, conducted at a tube inclination angle of 2 ° to the horizontal and a steam inlet temperature to the test tube of approximately 60 °C.

The presented figure clearly illustrates the predicted densimetric gas Froude number at which the onset of flooding is predicted, as proposed by Zapke [97ZA1] in equation (A.53.) The sudden increase in the measured tube pressure drop, associated with tube flooding, compares well to the predicted flooding point. At operating conditions with a densimetric gas Froude number larger than the flooding point, the steam velocity inside the test tube is sufficient to force condensate to drain through the top of the test tube via the outlet header. This phenomenon explains the trend in the measured pressure drop results.

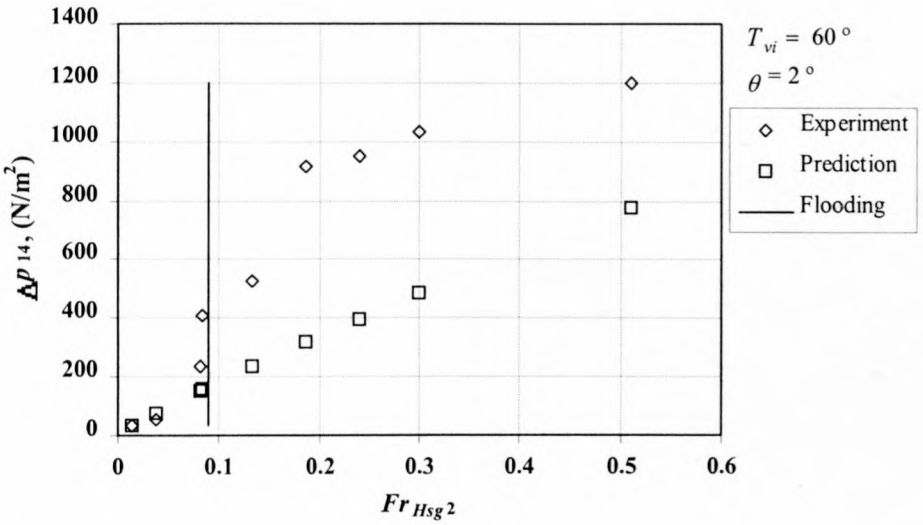

Figure D.4: Comparison between experimental results and the predicted pressure drop.

D.2 Experimental data for all evaluated tube inclination angles

Table D.1a: Experimental results obtained with an inclination angle, θ = -5, and steam inlet temperature T_{si} = 50 °C.

No.	p_{atm}	T_{si}	T_{so}	T_{ai1}	T_{ai2}	T_{ai3}	T_{ai4}	T_{ao1}	T_{ao2}	T_{ao3}	T_{ao4}
-	N/m^2	°C	°C	°C	°C	°C	°C	°C	°C	°C	°C
1	100212	50.34	46.3	22.46	22.52	22.67	22.9	40.18	41.59	41.17	42.48
2	100212	50.31	49.07	22.41	22.31	22.71	22.75	41.39	42.21	41.95	43.08
3	100212	49.33	46.3	22.53	22.41	22.59	22.96	38.9	40.31	41.05	41.32
4	100212	49.59	40.24	22.37	22.65	22.8	22.77	34.44	40.93	41.66	41.87
5	100212	49.24	38.78	22.74	22.36	22.5	22.89	37.52	40.88	41.51	41.81
6	100212	48.87	34.23	23.17	23.12	23.4	23.42	35.84	38.34	38.99	39.27
7	100212	48.95	34.13	23.2	23.08	23.35	23.68	35.82	38.35	39	39.39
8	100212	50.21	50.14	22.81	22.97	23.22	23.46	42.28	43.76	43.48	44.36

Table D.1 b: Experimental results obtained with an inclination angle, θ = -5, and steam inlet temperature T_{si} = 50 °C.

No.	m_{a1}	m_{a2}	m_{a3}	m_{a4}	Q_{a1}	Q_{a2}	Q_{a3}	Q_{a4}	Q_{atot}	Fr_{Hsg2}	Δp_{14}
-	kg/s	kg/s	kg/s	kg/s	kW	kW	kW	kW	kW		N/m^2
1	0.033	0.050	0.041	0.034	0.609	0.919	0.772	0.576	2.875	0.011	29.36
2	0.019	0.051	0.042	0.034	0.372	1.007	0.827	0.631	2.836	0.011	33.86
3	0.137	0.151	0.146	0.130	2.358	2.746	2.652	2.273	10.029	0.134	235.27
4	0.140	0.152	0.145	0.130	1.842	2.820	2.681	2.402	9.745	0.124	189.99
5	0.137	0.155	0.144	0.128	2.143	2.892	2.673	2.325	10.034	0.136	215.62
6	0.236	0.258	0.243	0.220	3.074	3.897	3.631	3.339	13.942	0.275	391.58
7	0.237	0.253	0.244	0.218	3.071	3.837	3.674	3.263	13.844	0.270	390.05
8	0.019	0.051	0.043	0.032	0.372	1.037	0.861	0.622	2.892	0.011	39.97

Table D.2 a: Experimental results obtained with an inclination angle, $\theta = 0$, and steam inlet temperature $T_{si} = 50\ ^{o}C$.

No.	p_{atm}	T_{si}	T_{so}	T_{ai1}	T_{ai2}	T_{ai3}	T_{ai4}	T_{ao1}	T_{ao2}	T_{ao3}	T_{ao4}
-	N/m^2	°C	°C	°C	°C	°C	°C	°C	°C	°C	°C
1	99774	49.79	47.66	20.25	20.16	20.17	20.31	39.68	40.39	40.46	41.98
2	99774	49.89	46.41	20.46	20.25	20.22	20.35	40.25	41.38	41.75	42.75
3	99774	49.83	48.66	20.38	20.31	20.28	20.4	39.94	40.23	41.2	41.78
4	99774	49.85	48.49	20.28	20.39	20.34	20.43	39.16	39.58	40.57	41.11
5	99774	49.66	48.02	20.5	20.56	20.61	20.64	38.27	38.84	39.82	40.38
6	99774	49.23	48.37	20.38	20.4	20.42	20.51	37.65	37.68	38.78	39.3
7	99774	49.78	48.78	20.61	20.71	20.59	20.62	37.73	37.91	39.06	39.56
8	99774	49.82	48.57	20.44	20.27	20.41	20.54	36.78	36.99	38.21	38.69

Table D.2 b: Experimental results obtained with an inclination angle, $\theta = 0$, and steam inlet temperature $T_{si} = 50\ ^{o}C$.

No.	m_{a1}	m_{a2}	m_{a3}	m_{a4}	Q_{a1}	Q_{a2}	Q_{a3}	Q_{a4}	Q_{atot}	Fr_{Hsg2}	Δp_{14}
-	kg/s	kg/s	kg/s	kg/s	kW	kW	kW	kW	kW		N/m^2
1	0.030	0.052	0.042	0.035	0.606	1.078	0.866	0.689	3.238	0.014	20.058
2	0.057	0.078	0.068	0.058	1.170	1.669	1.481	1.210	5.530	0.040	28.361
3	0.110	0.128	0.119	0.105	2.218	2.608	2.460	2.138	9.425	0.116	168.18
4	0.136	0.153	0.145	0.128	2.666	2.986	2.882	2.543	11.076	0.160	251.99
5	0.163	0.173	0.170	0.152	3.026	3.213	3.194	2.885	12.318	0.200	314.56
6	0.191	0.209	0.190	0.177	3.417	3.659	3.398	3.207	13.680	0.253	400.96
7	0.192	0.210	0.189	0.177	3.386	3.631	3.377	3.212	13.606	0.247	394.22
8	0.228	0.248	0.231	0.210	3.838	4.172	3.969	3.651	15.629	0.326	486.18

Table D.3a: Experimental results obtained with an inclination angle, $\theta = 1$, and steam inlet temperature $T_{si} = 50$ °C.

No.	p_{atm}	T_{si}	T_{so}	T_{ai1}	T_{ai2}	T_{ai3}	T_{ai4}	T_{ao1}	T_{ao2}	T_{ao3}	T_{ao4}
-	N/m^2	°C	°C	°C	°C	°C	°C	°C	°C	°C	°C
1	100494	50.02	48.92	23.5	23.4	23.25	23.5	41.25	42.36	42.49	43.79
2	100494	49.81	47.72	23.48	23.36	23.24	23.48	42.16	43.17	43.49	44.3
3	100494	50.15	47.32	23.53	23.63	23.33	23.34	42.19	42.83	43.25	43.77
4	100494	49.99	46.04	23.25	23.53	23.31	23.28	41.24	41.67	42.17	42.65
5	100494	49.88	45.54	23.43	23.79	23.42	23.21	40.12	40.24	41.16	41.8
6	100494	50.13	46.43	23.35	23.77	23.37	23.14	39.62	39.7	40.63	41.36
7	100494	50.21	46.35	23.35	23.8	23.42	23.15	39.61	39.79	40.67	41.44
8	100494	49.89	46.1	23.24	23.74	23.39	23.13	38.77	38.86	39.92	40.65
9	100494	49.87	44.96	23.19	23.58	23.49	23.2	38.01	38	39.19	40.06
10	100494	49.96	44.26	23.21	23.35	23.31	23	37.37	37.46	38.68	39.57
11	100494	49.97	43.39	22.94	23.34	23.49	23.01	36.19	36.33	37.77	38.46
12	100494	50.02	43.08	22.95	23.22	23.35	22.81	35.5	35.65	37.09	37.72

Table D.3b: Experimental results obtained with an inclination angle, $\theta = 1$, and steam inlet temperature $T_{si} = 50$ °C.

No.	m_{a1}	m_{a2}	m_{a3}	m_{a4}	Q_{a1}	Q_{a2}	Q_{a3}	Q_{a4}	Q_{atot}	Fr_{Hsg2}	Δp_{14}
-	kg/s	kg/s	kg/s	kg/s	kW	kW	kW	kW	kW		N/m^2
1	0.019	0.051	0.042	0.034	0.352	1.011	0.851	0.647	2.861	0.0102	25.70
2	0.048	0.078	0.068	0.058	0.941	1.59	1.399	1.144	5.075	0.0330	86.56
3	0.077	0.104	0.094	0.081	1.498	2.057	1.865	1.584	7.003	0.0624	189.00
4	0.106	0.131	0.122	0.106	1.988	2.423	2.259	1.984	8.654	0.0968	406.51
5	0.136	0.156	0.147	0.129	2.315	2.596	2.531	2.325	9.767	0.1262	592.63
6	0.163	0.174	0.172	0.153	2.713	2.791	2.884	2.698	11.086	0.1611	633.67
7	0.163	0.174	0.172	0.153	2.715	2.786	2.878	2.699	11.079	0.1611	606.30
8	0.189	0.209	0.19	0.178	3.011	3.19	3.027	3.012	12.241	0.1988	638.12
9	0.216	0.237	0.221	0.2	3.249	3.436	3.336	3.226	13.247	0.2362	655.21
10	0.244	0.263	0.248	0.224	3.505	3.684	3.661	3.53	14.379	0.2802	698.74
11	0.294	0.314	0.303	0.274	3.94	4.033	4.132	3.999	16.104	0.3548	788.04
12	0.345	0.359	0.349	0.319	4.372	4.417	4.585	4.491	17.866	0.4357	849.92

Table D.4a: Experimental results obtained with an inclination angle, $\theta = 2$, and steam inlet temperature $T_{si} = 50\ ^{o}C$.

No.	p_{atm}	T_{si}	T_{so}	T_{ai1}	T_{ai2}	T_{ai3}	T_{ai4}	T_{ao1}	T_{ao2}	T_{ao3}	T_{ao4}
-	N/m^2	°C	°C	°C	°C	°C	°C	°C	°C	°C	°C
1	100462	50.06	47.4	24.07	24.08	23.95	23.99	42.03	41.99	42.27	43.71
2	100462	49.84	46.66	24.1	24.12	24.02	24.08	42.6	43.38	43.6	44.42
3	100462	49.93	45.16	24.18	24.21	23.98	24.14	42.46	43.14	43.57	43.99
4	100462	49.82	42.73	24.35	24.26	24.07	24.01	41.6	42.53	42.91	43.12
5	100462	49.58	41.51	24.66	24.19	24.16	24.39	40.09	41.5	41.6	41.81
6	100462	50.04	40.83	24.45	24.27	24.1	24.18	40.78	41.23	41.51	42.03
7	100462	50.1	46.69	24.59	24.43	24.3	24.23	40.06	40.07	40.76	41.4
8	100462	49.99	45.91	24.45	24.5	24.17	24.25	39.87	39.98	40.65	41.3

Table D.4b: Experimental results obtained with an inclination angle, $\theta = 2$, and steam inlet temperature $T_{si} = 50\ ^{o}C$.

No.	m_{a1}	m_{a2}	m_{a3}	m_{a4}	Q_{a1}	Q_{a2}	Q_{a3}	Q_{a4}	Q_{atot}	Fr_{Hsg2}	Δp_{14}
-	kg/s	kg/s	kg/s	kg/s	kW	kW	kW	kW	kW		N/m^2
1	0.019	0.051	0.041	0.034	0.353	0.957	0.793	0.615	2.717	0.009	23.952
2	0.046	0.078	0.068	0.058	0.892	1.544	1.35	1.124	4.91	0.031	66.002
3	0.078	0.104	0.095	0.083	1.453	2.008	1.849	1.569	6.879	0.062	136.69
4	0.107	0.131	0.12	0.106	1.876	2.421	2.231	1.934	8.462	0.095	233.98
5	0.135	0.155	0.148	0.13	2.126	2.701	2.515	2.189	9.531	0.122	461.55
6	0.137	0.157	0.147	0.129	2.216	2.651	2.484	2.217	9.569	0.123	680.50
7	0.165	0.177	0.173	0.154	2.561	2.738	2.748	2.539	10.586	0.151	918.79
8	0.164	0.177	0.173	0.153	2.551	2.715	2.754	2.511	10.531	0.149	938.32

Table D.5a: Experimental results obtained with an inclination angle, $\theta = 4$, and steam inlet temperature $T_{si} = 50\ ^{o}C$.

No.	p_{atm}	T_{si}	T_{so}	T_{ai1}	T_{ai2}	T_{ai3}	T_{ai4}	T_{ao1}	T_{ao2}	T_{ao3}	T_{ao4}
-	N/m^2	°C	°C	°C	°C	°C	°C	°C	°C	°C	°C
1	99673	50.18	44.93	26.29	26.32	26.08	25.87	43.88	43.53	44.08	44.95
2	99673	50.23	48.96	26.36	26.15	25.76	25.81	44.28	44.45	44.72	45.39
3	99673	50.22	47.69	26.41	26.07	25.73	25.58	43.78	44.23	44.62	44.97
4	99673	49.92	49.04	25.79	25.68	25.84	25.76	43.18	43.31	43.83	44.09
5	99673	50.21	48.18	25.82	25.89	25.8	25.72	42.32	42.76	43.29	43.44
6	99673	49.98	46.33	25.97	25.85	25.9	25.81	41.03	41.8	42.23	42.18
7	99673	49.8	44.46	26.12	26.01	25.68	25.59	40.72	41.54	41.83	41.67
8	99673	50.5	46.53	25.89	25.96	25.57	25.62	40.05	39.93	40.6	41.19

Table D.5b: Experimental results obtained with an inclination angle, $\theta = 4$, and steam inlet temperature $T_{si} = 50\ ^{o}C$.

No.	m_{a1}	m_{a2}	m_{a3}	m_{a4}	Q_{a1}	Q_{a2}	Q_{a3}	Q_{a4}	Q_{atot}	Fr_{Hsg2}	Δp_{14}
-	kg/s	kg/s	kg/s	kg/s	kW	kW	kW	kW	kW		N/m^2
1	0.018	0.05	0.042	0.033	0.337	0.913	0.764	0.588	2.601	0.008	60.56
2	0.035	0.076	0.067	0.056	0.644	1.429	1.276	1.039	4.388	0.025	107.08
3	0.072	0.103	0.092	0.08	1.282	1.908	1.736	1.484	6.41	0.053	160.44
4	0.102	0.128	0.118	0.104	1.813	2.287	2.085	1.802	7.987	0.085	231.46
5	0.13	0.154	0.142	0.126	2.201	2.621	2.413	2.115	9.35	0.115	332.05
6	0.158	0.172	0.17	0.149	2.446	2.754	2.695	2.316	10.211	0.139	580.16
7	0.159	0.171	0.169	0.15	2.354	2.651	2.63	2.307	9.942	0.134	703.80
8	0.186	0.206	0.187	0.172	2.667	2.854	2.691	2.559	10.771	0.153	1534.8

Table D.6a: Experimental results obtained with an inclination angle, θ = -5 °, and steam inlet temperature T_{si} = 60 °C.

No.	p_{atm}	T_{si}	T_{so}	T_{ai1}	T_{ai2}	T_{ai3}	T_{ai4}	T_{ao1}	T_{ao2}	T_{ao3}	T_{ao4}
-	N/m^2	°C	°C	°C	°C	°C	°C	°C	°C	°C	°C
1	99515	59.84	59.63	20.58	20.55	20.67	21.14	46.62	47.90	47.46	49.18
2	99515	59.70	59.29	20.81	20.61	20.69	21.00	48.23	48.92	49.30	50.41
3	99515	59.26	58.78	21.16	20.85	20.88	21.14	47.61	47.58	48.56	49.19
4	99515	59.47	59.00	21.27	21.13	20.97	21.20	47.98	48.07	49.05	49.63
5	99515	59.24	58.43	20.97	20.78	20.87	21.15	46.58	46.68	47.72	48.13
6	99515	59.86	59.34	21.49	21.17	21.07	21.22	45.94	46.06	46.90	47.46
7	99515	59.77	58.70	21.18	20.86	21.03	21.56	43.74	44.04	44.95	45.52

Table D.6b: Experimental results obtained with an inclination angle, θ = -5 °, and steam inlet temperature T_{si} = 60 °C.

No.	m_{a1}	m_{a2}	m_{a3}	m_{a4}	Q_{a1}	Q_{a2}	Q_{a3}	Q_{a4}	Q_{atot}	Fr_{Hsg2}	Δp_{14}
-	kg/s	kg/s	kg/s	kg/s	kW	kW	kW	kW	kW		N/m^2
1	0.018	0.046	0.036	0.030	0.492	1.219	0.972	0.754	3.437	0.011	20.035
2	0.054	0.077	0.067	0.058	1.517	2.139	1.875	1.542	7.073	0.046	58.636
3	0.100	0.123	0.113	0.101	2.729	3.307	3.072	2.647	11.756	0.124	185.06
4	0.096	0.121	0.111	0.099	2.645	3.303	3.060	2.665	11.673	0.120	173.24
5	0.136	0.155	0.150	0.135	3.614	4.077	3.938	3.485	15.113	0.201	300.25
6	0.169	0.193	0.178	0.164	4.227	4.785	4.433	4.094	17.539	0.271	416.24
7	0.225	0.246	0.236	0.212	5.209	5.653	5.422	4.830	21.113	0.396	562.45

Table D.7a: Experimental results obtained with an inclination angle, $\theta = 0$ °, and steam inlet temperature $T_{si} = 60$ °C.

No.	p_{atm}	T_{si}	T_{so}	T_{ai1}	T_{ai2}	T_{ai3}	T_{ai4}	T_{ao1}	T_{ao2}	T_{ao3}	T_{ao4}
-	N/m^2	°C	°C	°C	°C	°C	°C	°C	°C	°C	°C
1	99784	59.88	53.78	28.13	28.15	28.06	28.03	49.76	51.44	52.06	52.86
2	99784	60.06	59.34	28.16	28.21	28.32	28.21	49.21	49.59	50.64	51.29
3	99784	60.16	58.35	28.14	28.12	28.32	28.41	47.04	47.73	48.96	49.48
4	99784	59.90	57.48	28.21	27.92	28.18	28.38	45.30	45.92	47.28	47.78
5	99784	60.18	58.77	28.33	28.10	28.13	28.36	44.46	44.89	46.14	46.62
6	99784	60.07	57.92	28.14	27.82	28.18	28.48	43.02	43.62	45.03	45.54
7	99784	59.86	58.31	28.52	28.27	28.10	28.16	42.63	43.10	44.32	44.76

Table D.7b: Experimental results obtained with an inclination angle, $\theta = 0$ °, and steam inlet temperature $T_{si} = 60$ °C.

No.	m_{a1}	m_{a2}	m_{a3}	m_{a4}	Q_{a1}	Q_{a2}	Q_{a3}	Q_{a4}	Q_{atot}	Fr_{Hsg2}	Δp_{14}
-	Kg/s	kg/s	kg/s	kg/s	kW	kW	kW	kW	kW		N/m^2
1	0.062	0.102	0.094	0.081	1.381	2.421	2.230	1.915	7.947	0.054	125.88
2	0.125	0.154	0.145	0.129	2.682	3.313	3.150	2.820	11.965	0.125	258.97
3	0.182	0.208	0.189	0.179	3.539	4.051	3.755	3.560	14.904	0.194	334.16
4	0.236	0.262	0.250	0.225	4.138	4.677	4.567	4.126	17.507	0.273	435.88
5	0.288	0.311	0.300	0.274	4.755	5.151	5.167	4.723	19.796	0.346	520.21
6	0.340	0.362	0.350	0.322	5.169	5.611	5.597	5.165	21.541	0.416	609.85
7	0.368	0.397	0.381	0.350	5.294	5.778	5.843	5.450	22.365	0.454	660.88

Table D.8a: Experimental results obtained with an inclination angle, $\theta = 1\ ^{\circ}$, and steam inlet temperature $T_{si} = 60\ ^{\circ}C$.

No.	p_{atm}	T_{si}	T_{so}	T_{ai1}	T_{ai2}	T_{ai3}	T_{ai4}	T_{ao1}	T_{ao2}	T_{ao3}	T_{ao4}
-	N/m^2	°C	°C	°C	°C	°C	°C	°C	°C	°C	°C
1	100494	60.06	59.82	23.74	23.47	23.16	23.49	49.01	49.26	49.77	51.62
2	100494	59.8	59.44	23.76	23.66	23.29	23.33	50.28	50.71	51.07	52.24
3	100494	59.87	58.87	23.65	23.77	23.31	23.31	49.92	49.77	50.37	51.23
4	100494	59.92	57.66	23.58	23.74	23.26	23.21	48.63	48.62	49.58	50.38
5	100494	59.81	55.69	23.42	23.48	23.2	23.09	46.97	47.3	48.39	49.35
6	100494	59.97	55.03	23.26	23.72	23.13	22.96	46.1	46.44	47.63	48.65
7	100494	59.91	55.23	23.19	23.58	23.01	22.91	45.06	45.28	46.7	47.76
8	100494	59.82	55.37	23.07	23.14	23.32	23	43.23	43.43	45.16	46
9	100494	59.75	54.62	22.85	23.12	23.34	23.04	42	42.18	44.05	44.79
10	100494	59.59	55.23	22.7	23.17	23.24	23.03	40.7	40.95	42.92	43.45

Table D.8b: Experimental results obtained with an inclination angle, $\theta = 1\ ^{\circ}$, and steam inlet temperature $T_{si} = 60\ ^{\circ}C$.

No.	m_{a1}	m_{a2}	m_{a3}	m_{a4}	Q_{a1}	Q_{a2}	Q_{a3}	Q_{a4}	Q_{atot}	Fr_{Hsg2}	Δp_{14}
-	Kg/s	kg/s	kg/s	kg/s	kW	kW	kW	kW	kW		N/m^2
1	0.018	0.050	0.041	0.033	0.488	1.332	1.114	0.837	3.771	0.012	24.453
2	0.018	0.076	0.066	0.057	0.504	2.110	1.866	1.538	6.018	0.031	101.51
3	0.061	0.102	0.092	0.080	1.662	2.709	2.480	2.132	8.982	0.069	415.96
4	0.093	0.127	0.118	0.103	2.418	3.247	3.063	2.697	11.426	0.110	547.03
5	0.126	0.152	0.143	0.127	3.048	3.617	3.485	3.188	13.338	0.156	530.51
6	0.154	0.173	0.168	0.150	3.601	3.928	3.977	3.698	15.204	0.202	625.74
7	0.182	0.205	0.185	0.172	4.076	4.451	4.234	4.086	16.847	0.248	693.89
8	0.233	0.258	0.243	0.218	4.829	5.218	5.111	4.789	19.947	0.350	747.27
9	0.286	0.307	0.295	0.267	5.591	5.820	5.863	5.514	22.788	0.463	860.64
10	0.337	0.355	0.342	0.314	6.203	6.260	6.439	6.086	24.988	0.561	965.15

Table D.9a: Experimental results obtained with an inclination angle, $\theta = 2\ ^{\circ}$, and steam inlet temperature $T_{si} = 60\ ^{\circ}C$.

No.	p_{atm}	T_{si}	T_{so}	T_{ai1}	T_{ai2}	T_{ai3}	T_{ai4}	T_{ao1}	T_{ao2}	T_{ao3}	T_{ao4}
-	N/m^2	°C	°C	°C	°C	°C	°C	°C	°C	°C	°C
1	100573	60.34	60.2	20.42	20.28	20.17	20.29	48.5	48.3	49.57	51.26
2	100573	60.16	59.63	20.22	20.07	19.92	20.15	49.85	50.02	50.38	51.76
3	100573	59.89	57.02	20.84	20.73	20.3	20.45	48.93	49.01	49.72	50.69
4	100573	60.11	56.88	21.02	20.81	20.41	20.51	49.04	49.08	49.86	50.84
5	100573	59.72	53.82	20.87	20.7	20.45	20.53	47.49	47.9	48.87	49.65
6	100573	59.75	57.8	20.8	20.76	20.32	20.53	46.71	46.49	47.58	48.51
7	100573	59.81	57.67	21.07	20.97	20.51	20.69	45.67	45.52	46.52	47.73
8	100573	59.47	57.07	20.5	20.47	20.49	20.54	44.25	44.01	45.24	46.52
9	100573	58.72	55.79	21.86	21.63	20.67	20.57	41.09	40.96	42.12	43.04

Table D.9b: Experimental results obtained with an inclination angle, $\theta = 2\ ^{\circ}$, and steam inlet temperature $T_{si} = 60\ ^{\circ}C$.

No.	m_{a1}	m_{a2}	m_{a3}	m_{a4}	Q_{a1}	Q_{a2}	Q_{a3}	Q_{a4}	Q_{atot}	Fr_{Hsg2}	Δp_{14}
-	Kg/s	kg/s	kg/s	kg/s	kW	kW	kW	kW	kW		N/m^2
1	0.018	0.05	0.041	0.034	0.545	1.503	1.239	0.967	4.254	0.015	35.253
2	0.018	0.077	0.067	0.057	0.561	2.377	2.063	1.692	6.693	0.038	55.613
3	0.064	0.104	0.093	0.081	1.856	2.972	2.718	2.327	9.873	0.084	406.15
4	0.064	0.103	0.093	0.08	1.837	2.952	2.707	2.31	9.805	0.082	232.43
5	0.097	0.129	0.117	0.105	2.642	3.533	3.261	2.914	12.35	0.133	528.88
6	0.129	0.154	0.144	0.127	3.411	3.932	3.79	3.408	14.54	0.187	912.05
7	0.158	0.179	0.17	0.151	3.947	4.348	4.263	3.912	16.469	0.241	946.22
8	0.188	0.211	0.187	0.175	4.544	4.925	4.441	4.332	18.241	0.300	1031.6
9	0.288	0.309	0.294	0.271	5.614	5.883	6.03	5.806	23.333	0.511	1196.9

Table D.10a: Experimental results obtained with an inclination angle, $\theta = 4\ ^{o}$, and steam inlet temperature $T_{si} = 60\ ^{o}C$.

No.	p_{atm}	T_{si}	T_{so}	T_{ai1}	T_{ai2}	T_{ai3}	T_{ai4}	T_{ao1}	T_{ao2}	T_{ao3}	T_{ao4}
-	N/m^2	°C	°C	°C	°C	°C	°C	°C	°C	°C	°C
1	99681	60.14	56.87	27.35	27.21	26.77	26.80	50.06	49.79	50.73	52.07
2	99681	59.95	55.86	27.18	27.05	26.90	26.88	50.74	51.67	51.93	53.03
3	99681	60.15	55.12	27.42	27.07	26.87	26.84	50.93	51.70	52.22	52.91
4	99681	59.93	58.71	27.16	27.17	27.09	27.18	50.68	50.97	51.55	52.01
5	99681	60.21	58.07	27.15	27.61	27.23	27.13	49.75	50.30	50.90	51.17
6	99681	60.27	57.53	27.31	27.46	27.23	27.18	49.52	50.28	50.81	50.90
7	99681	60.14	56.15	27.23	27.72	27.36	27.36	48.23	49.31	49.64	49.80
8	99681	59.95	54.80	27.30	27.84	27.44	27.51	47.86	48.88	49.14	49.65

Table D.10b: Experimental results obtained with an inclination angle, $\theta = 4\ ^{o}$, and steam inlet temperature $T_{si} = 60\ ^{o}C$.

No.	m_{a1}	m_{a2}	m_{a3}	m_{a4}	Q_{a1}	Q_{a2}	Q_{a3}	Q_{a4}	Q_{atot}	Fr_{Hsg2}	Δp_{14}
-	kg/s	kg/s	kg/s	kg/s	kW	kW	kW	kW	kW		N/m^2
1	0.018	0.050	0.041	0.033	0.426	1.186	0.991	0.750	3.353	0.009	44.08
2	0.018	0.075	0.065	0.055	0.441	1.897	1.642	1.339	5.319	0.024	64.05
3	0.057	0.100	0.089	0.078	1.382	2.518	2.265	1.916	8.081	0.055	67.79
4	0.089	0.126	0.114	0.102	2.128	3.041	2.736	2.389	10.294	0.092	101.43
5	0.117	0.150	0.139	0.124	2.719	3.436	3.212	2.822	12.190	0.128	261.47
6	0.118	0.148	0.140	0.125	2.697	3.403	3.214	2.819	12.133	0.126	391.46
7	0.147	0.168	0.163	0.146	3.196	3.643	3.517	3.129	13.485	0.156	629.99
8	0.147	0.169	0.164	0.146	3.110	3.552	3.444	3.071	13.177	0.152	880.09

APPENDIX E

BOX-TYPE INLET MANIFOLD INVESTIGATION

E.1 Sample calculation illustrating the calculation of the header pipe loss coefficient

The static pressure loss between the header pipe and the bundle tubes (sections 1 and 2 as shown in the schematic of the experimental apparatus presented in figure 4.10), is presented in terms of a dimensionless inlet header loss coefficient, K_{h_2}. This sample calculation illustrates the calculation of K_{h_2} for two experimental data points that were obtained during a test run representing the operating conditions of tube bundle 4 as per the schematic shown in figure 2.6. Table E.4 presents the experimental data used in the following sample calculation.

The selected data points represent an up- and downstream position within the box-manifold. Within the upstream side of the box-manifold high flow distortions are encountered, while essentially no flow distortions are encountered in the downstream side.

The experimental data is as follows:

Dephlegmator bundle tube geometry as given in Appendix B:

Tube height	H_t	=	0.097 m
Tube cross-section flow area	A_{tc}	=	$1.330x10^{-3}$ m^2
Total number of tubes	n_t	=	115
Tube pitch	P_f	=	0.05 m
Fin height	H_f	=	0.12 m
Hydraulic tube diameter	d_e	=	0.02593 m

Geometry of the experimental apparatus:

Tube length	L_t	=	2 m
Flow area ratio at the inlet to the bundle tubes	σ_{21}	=	0.2217
Tube inclination angle	θ_t	=	60 °

Operating conditions:

Header pipe inlet air temperature	T_{aip}	=	23 °C
Water temperature	T_w	=	19 °C
Air mass flow rate through dephlegmator	m_a	=	2.2717 kg/s

Upstream data point: (L_{dm} = 0.4 m) (See figure 4.11):

Manifold downstream tube pressure differential	$(p_2 - p_3)_u$	=	81 N/m^2
Manifold pressure differential	p_1-p_3	=	236 N/m^2
Air velocity inside bundle tubes	v_{2u}	=	5.25 m/s

Downstream data point: (L_{dm} = 0.7 m) (See figure 4.11):

Manifold upstream tube pressure differential	$(p_2 - p_3)_d$	=	191 N/m^2
Manifold pressure differential	p_1-p_3	=	236 N/m^2
Air velocity inside bundle tubes	v_{2d}	=	12.603 m/s

[1]*The required fluid properties within the header pipe are as follows:*

Air density	ρ_a	=	1.1785 kg/m^3
Air viscosity	μ_a	=	1.82912x10^{-5} kg/ms
Water density	ρ_l	=	998.859 kg/m^3

The average superficial gas velocity at the inlet to the dephlegmator header pipe is calculated as follows:

$$v_{sga} = m_a/(\rho_a A_{tc} n_t) = 2.2717/(1.1785x1.330x10^{-3} x115) = 12.603 \text{ m/s} \qquad \text{(E.1)}$$

[1] All fluid properties are determined by means of the relevant correlations given in Appendix F.

and the superficial densimetric gas Froude number is calculated by means of equation (2.1).

$$Fr_{Hsga} = \frac{1.1785x12.603^2}{9.81x0.097x(998.859-1.1785)} = 0.19717 \qquad \text{(E.2)}$$

The average superficial gas velocity at the inlet to the header pipe is calculated as follows:

$$v_{sgh} = \frac{m_a}{\rho_a x A_{hc}} = \frac{2.2717}{1.1785x0.098} = 19.635 \text{ m/s}$$

The inlet header loss coefficient K_{h2} can now be calculated for the respective data points by means of equation (4.4):

$$K_{h2} = \frac{p_{13} - p_{23u} - 0.5\rho_a v_{2u}^2}{0.5\rho_a v_{sgh}^2} + 1 = \frac{236-81-0.5x1.1785x5.25^2}{0.5x1.1785x19.635^2} = 1.16108$$

$$K_{h2} = \frac{p_{13} - p_{23u} - 0.5\rho_a v_{2u}^2}{0.5\rho_a v_{sgh}^2} + 1 = \frac{236-191-0.5x1.1785x12.603^2}{0.5x1.1785x19.635^2} = 0.78610$$

E.2 Experimental data

The experimental data and header pipe loss coefficient, K_{h2}, results obtained during the investigation are presented in the following tables. Tube pressure differentials, Δp_{23}, were measured for a selection of bundle tubes as indicated in the tables. The measured tube pressure differentials and tube velocities are correlated for the purpose of the investigation and the correlated values are also presented in the tables and accompanying figures.

Table E.1: Experimental results obtained for flow conditions representative of dephlegmator tube bundle 1 as per figure 2.6.

m_a	ρ_a	μ_a	ρ_l	Δp_{13}
(kg/s)	**(kg/m³)**	**(kg/ms)**	**(kg/m³)**	**(N/m²)**
2.3674	1.2206	$1.784x10^{-5}$	998.859	230

	Measured Results		**Correlated Results**		
L_{dm}	Δp_{23}	v_2	Δp_{23}	v_2	K_{h2}
(m)	**(N/m²)**	**(m/s)**	**(N/m²)**	**(m/s)**	
0	124	9.00	123.00	8.97	1.2427
0.05		7.00	112.92	8.17	1.3200
0.1	106	7.50	104.19	7.48	1.3843
0.15		6.50	96.80	6.90	1.4368
0.2		7.00	90.75	6.42	1.4784
0.25	95	6.00	86.05	6.05	1.5100
0.3	88	5.75	82.69	5.78	1.5322
0.35		5.00	80.67	5.62	1.5453
0.4	80	5.50	80.00	5.57	1.5496
0.45		6.00	83.50	5.77	1.5292
0.5	94	5.80	94.00	6.36	1.4667
0.55		7.20	111.50	7.35	1.3587
0.6		9.00	136.00	8.73	1.1990
0.65		8.25	167.50	10.51	0.9792
0.7		13.00	206.00	12.69	0.6886
0.9	204	12.25	206.00	12.69	0.6886
2	201	12.50	206.00	12.69	0.6886
2.65	207	13.00	206.00	12.69	0.6886

Table E.2: Experimental results obtained for flow conditions representative of dephlegmator tube bundle 2 as per figure 2.6.

m_a	ρ_a	μ_a	ρ_l	Δp_{13}
(kg/s)	**(kg/m^3)**	**(kg/ms)**	**(kg/m^3)**	**(N/m^2)**
2.2735	1.2056	$1.808x10^{-5}$	998.859	309

	Measured Results		**Correlated Results**		
L_{dm}	Δp_{23}	v_2	Δp_{23}	v_2	K_{h2}
(m)	**(N/m^2)**	**(m/s)**	**(N/m^2)**	**(m/s)**	
0	159.00	10.50	167.50	10.95	2.2456
0.05		11.00	163.36	10.62	2.3958
0.1	166.00	10.25	160.14	10.37	2.5111
0.15		10.00	157.84	10.19	2.5926
0.2		10.80	156.46	10.08	2.6411
0.25	156.00	10.00	156.00	10.05	2.6573
0.3	154.00	10.50	157.96	10.15	2.6001
0.35		11.00	163.84	10.45	2.4274
0.4	184.00	12.00	173.64	10.95	2.1352
0.45		11.00	187.36	11.65	1.7169
0.5	204.00	12.75	205.00	12.55	1.1636
0.9	209.00	11.70	205.00	12.55	1.1636
2	200.00	12.50	205.00	12.55	1.1636
2.65	210.00	13.25	205.00	12.55	1.1636

Table E.3: Experimental results obtained for flow conditions representative of dephlegmator tube bundle 3 as per figure 2.6.

m_a	ρ_a	μ_a	ρ_l	Δp_{13}
(kg/s)	(kg/m^3)	(kg/ms)	(kg/m^3)	(N/m^2)
2.3962	1.160	$1.8219x10^{-5}$	998.859	295

	Measured Results		Correlated Results		
L_{dm}	Δp_{23}	v_2	Δp_{23}	v_2	K_{h2}
(m)	(N/m^2)	(m/s)	(N/m^2)	(m/s)	
0	150.00	11.20	148.00	11.17	2.1634
0.05		10.00	130.75	10.38	2.5853
0.1	124.00	10.00	125.00	10.12	2.7235
0.15		11.00	129.06	10.33	2.6211
0.175		10.20	134.14	10.59	2.4919
0.2		10.50	141.25	10.96	2.3090
0.25	170.00	13.00	161.56	12.02	1.7726
0.3	177.00	12.50	190.00	13.51	0.9875
0.4	187.00	13.50	190.00	13.51	0.9875
0. 5	191.00	14.00	190.00	13.51	0.9875
0.9	192.00	12.75	190.00	13.51	0.9875
2	186.00	15.00	190.00	13.51	0.9875
2.65	187.00	12.80	190.00	13.51	0.9875

Table E.4: Experimental results obtained for flow conditions representative of dephlegmator tube bundle 4 as per figure 2.6.

m_a	ρ_a	μ_a	ρ_l	Δp_{13}
(kg/s)	**(kg/m³)**	**(kg/ms)**	**(kg/m³)**	**(N/m²)**
2.2717	1.1785	$1.8163x10^{-5}$	998.859	236

	Measured Results		**Correlated Results**		
L_{dm}	Δp_{23}	v_2	Δp_{23}	v_2	K_{h2}
(m)	**(N/m²)**	**(m/s)**	**(N/m²)**	**(m/s)**	
0	102.00	8.50	102.00	8.09	1.4200
0.05		6.80	91.71	6.70	1.5187
0.1	81.00	5.20	84.86	5.77	1.5789
0.15		5.50	81.43	5.31	1.6073
0.175		4.90	81.00	5.25	1.6108
0.2		5.00	81.49	5.29	1.6077
0.25	88.00	6.00	85.40	5.55	1.5831
0.3	104.00	6.20	93.22	6.07	1.5330
0.35		6.50	104.96	6.85	1.4550
0. 4	135.00	7.00	120.60	7.90	1.3462
0.45		11.00	140.16	9.21	1.2021
0.5	170.00	10.50	163.62	10.77	1.0175
0.55		13.80	191.00	12.60	0.7861
0.9	181.00	13.20	191.00	12.60	0.7861
2	196.00	11.40	191.00	12.60	0.7861
2.65	182.00	12.00	191.00	12.60	0.7861

Figures E.1 to E.4 shows the experimental pressure differential, Δp_{23}, results presented in tables E1 to E.4 respectively.

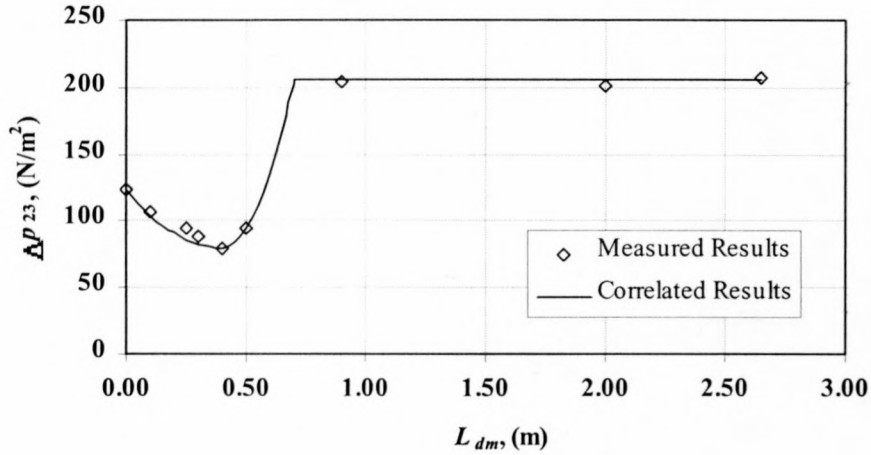

Figure E.1: Tube pressure differential (Δp_{23}) results representative of dephlegmator tube bundle 1 as per figure 2.6.

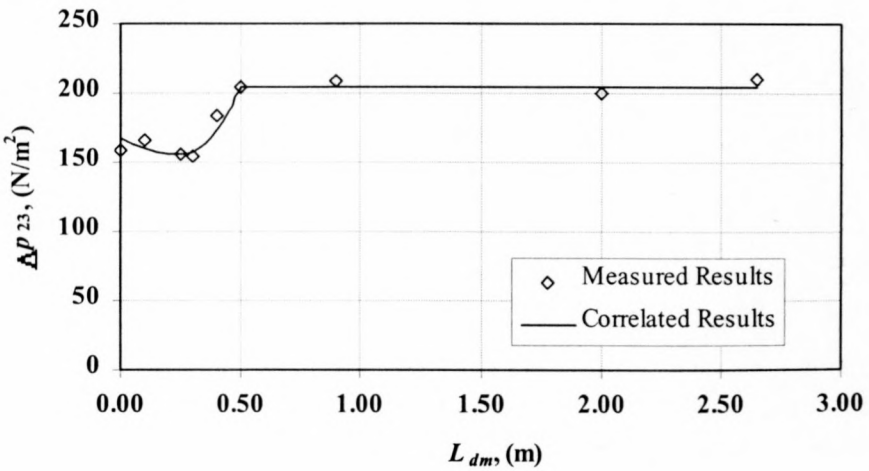

Figure E.2: Tube pressure differential (Δp_{23}) results representative of dephlegmator tube bundle 2 as per figure 2.6.

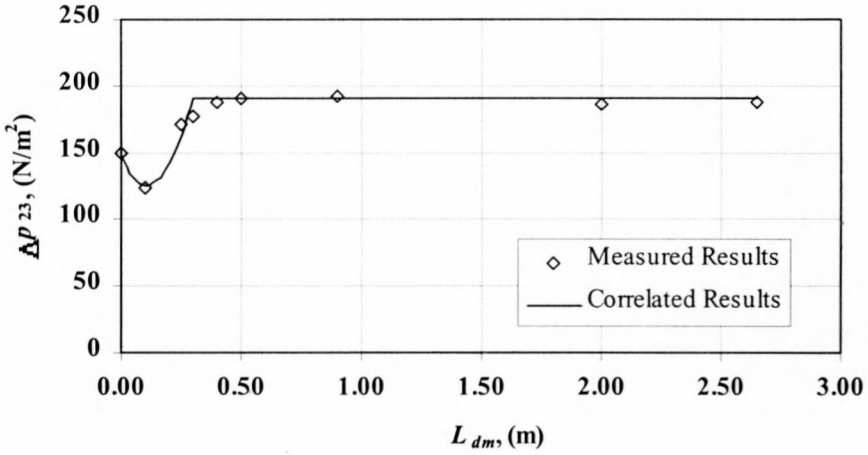

Figure E.3: Tube pressure differential (Δp_{23}) results representative of dephlegmator tube bundle 3 as per figure 2.6.

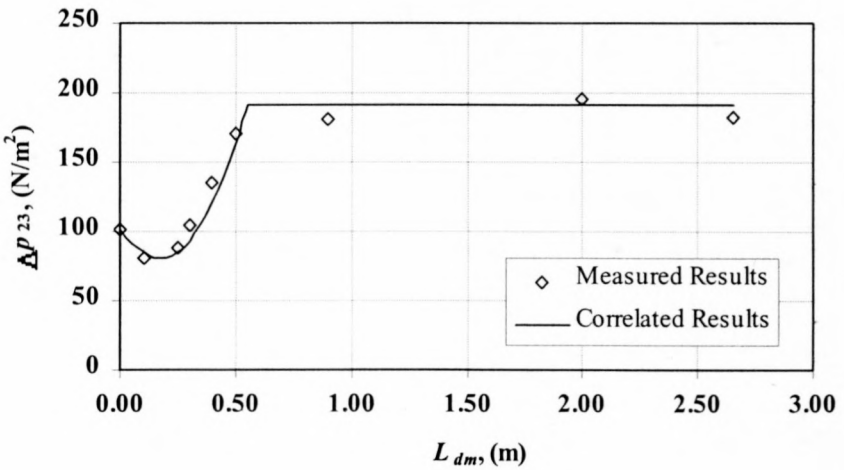

Figure E.4: Tube pressure differential (Δp_{23}) results representative of dephlegmator tube bundle 4 as per figure 2.6.

APPENDIX F

PROPERTIES OF FLUIDS

Kröger [98KR1] gives all the correlations presented in this appendix.

F.1 The thermophysical properties of dry air from 220K to 380K at standard atmospheric pressure (101325 N/m^2)

Density:

$$\rho_a = p_a/(287.08T), \text{ kg/m}^3 \tag{F.1}$$

Specific heat:

$$c_{pa} = 1.045356x10^3 - 3.161783x10^{-1}T + 7.083814x10^{-4}T^2 - 2.705209x10^{-7}T^3, \text{ J/kgK} \tag{F.2}$$

Dynamic viscosity:

$$\mu_a = 2.287973x10^{-6} + 6.259793x10^{-8}T - 3.131956x10^{-11}T^2 + 8.15038x10^{-15}T^3, \text{ kg/ms} \tag{F.3}$$

Thermal conductivity:

$$k_a = -4.937787x10^{-4} + 1.018087x10^{-4}T - 4.627937x10^{-8}T^2 + 1.250603x10^{-11}T^3, \text{ W/mK} \tag{F.4}$$

F.2 The thermophysical properties of saturated water vapour from 273.15K to 380K

Vapour pressure:

$$p_v = 10^z, \text{ N/m}^2$$

$$z = 10.79586(1 - 273.16/T) + 5.02808\,log_{10}(273.16/T)$$
$$+ 1.50474x10^{-4}\left[1 - 10^{-8.29692\{(T/273.16)-1\}}\right]$$
$$+ 4.2873x10^{-4}\left[10^{4.76955(1-273.16/T)} - 1\right] + 2.786118312 \quad \text{(F.5)}$$

Specific heat:

$$c_{pv} = 1.3605x10^3 - 2.31334T - 2.46784x10^{-10}T^5$$
$$+ 5.91332x10^{-13}T^6, \text{ J/kgK} \quad \text{(F.6)}$$

Dynamic viscosity:

$$\mu_v = 2.562435x10^{-6} + 1.816683x10^{-8}T - 2.579066x10^{-11}T^2$$
$$- 1.067299x10^{-14}T^3, \text{ kg/ms} \quad \text{(F.7)}$$

Thermal conductivity:

$$k_v = 1.3046x10^{-2} - 3.756191x10^{-5}T + 2.217964x10^{-7}T^2$$
$$- 1.111562x10^{-10}T^3, \text{ W/mK} \quad \text{(F.8)}$$

Density:

$$\rho_v = -4.062329056 + 0.10277044T - 9.76300388x10^{-4}T^2 + 4.475240795x10^{-6}T^3$$
$$- 1.004596894x10^{-8}T^4 + 8.9154895x10^{-12}T^5, \text{ kg/m}^3 \quad \text{(F.9)}$$

F.3 The thermophysical properties of mixtures of air and water vapour

Humidity ratio:

$$w = \left(\frac{2501.6 - 2.3263(T_{wb} - 273.15)}{2501.6 + 1.8577(T - 273.15) - 4.184(T_{wb} - 273.15)} \right) \left(\frac{0.62509 p_{vwb}}{p_{abs} - 1.005 p_{vwb}} \right)$$

$$- \left(\frac{1.00416(T - T_{wb})}{2501.6 + 1.8577(T - 273.15) - 4.184(T_{wb} - 273.15)} \right), \text{ kg/kg dry air} \qquad \text{(F.10)}$$

Density:

$$\rho_{av} = (1 + w)[1 - w/(w + 0.62198)]\, p_{abs} / (287.08T), \text{ kg air-vapour/m}^3 \qquad \text{(F.11)}$$

Specific heat:

$$c_{pav} = (c_{pa} + w c_{pv}) / (1 + w), \text{ J/Kkg air-vapour} \qquad \text{(F.12)}$$

Dynamic viscosity:

$$\mu_{av} = \left(X_a \mu_a M_a^{0.5} + X_v \mu_v M_v^{0.5} \right) / \left(X_a M_a^{0.5} + X_v M_v^{0.5} \right), \text{ kg/ms} \qquad \text{(F.13)}$$

where M_a = 28.97 kg/mole, M_v = 18.016 kg/mole, X_a = 1/(1+1.608w) and X_v = w/(w+0.622)

Thermal conductivity:

$$k_{av} = \left(X_a k_a M_a^{0.33} + X_v k_v M_v^{0.33} \right) / \left(X_a M_a^{0.33} + X_v M_v^{0.33} \right), \text{ W/mK} \qquad \text{(F.14)}$$

F.4 The thermophysical properties of saturated water liquid from 273.15K to 380K

Density:

$$\rho_w = \left(1.49343x10^{-3} - 3.7164x10^{-6}T + 7.09782x10^{-9}T^2 - 1.90321x10^{-20}T^6\right)^{-1}, \text{kg/m}^3 \quad \text{(F.15)}$$

Specific heat:

$$c_{pw} = 8.15599x10^{3} - 2.80627x10T + 5.11283x10^{-2}T^2 - 2.17582x10^{-13}T^6, \text{J/kgK} \quad \text{(F.16)}$$

Dynamic viscosity:

$$\mu_w = 2.414x10^{-5}x10^{247.8/(T-140)}, \text{kg/ms} \quad \text{(F.17)}$$

Thermal conductivity:

$$k_w = -6.14255x10^{-1} + 6.9962x10^{-3}T - 1.01075x10^{-5}T^2 + 4.74737x10^{-12}T^4, \text{W/mK} \quad \text{(F.18)}$$

Latent heat of vaporisation:

$$i_{fgw} = 3.4831814x10^{6} - 5.8627703x10^{3}T + 12.139568T^2 - 1.40290431x10^{-2}T^3, \text{J/kg} \quad \text{(F. 19)}$$


smit_inlet_2000